Hybrid Monte Carlo/Deterministic Neutron Transport for Shutdown Dose Rate Analysis

by

Elliott D. Biondo

A dissertation submitted in partial fulfillment of

the requirements for the degree of

Doctor of Philosophy

(Nuclear Engineering and Engineering Physics)

at the

UNIVERSITY OF WISCONSIN–MADISON

2016

Date of final oral examination: 7/21/2016

The dissertation is approved by the following members of the Final Oral Committee:

Paul Wilson, Professor, Nuclear Engineering and Engineering Physics
Douglass Henderson, Professor, Nuclear Engineering and Engineering Physics
James Blanchard, Professor, Nuclear Engineering and Engineering Physics
Bryan Bednarz, Professor, Medical Physics and Human Oncology
Scott Mosher, R&D Staff Member, Oak Ridge National Laboratory
Ahmad Ibrahim, R&D Staff Member, Oak Ridge National Laboratory

Dedicated to my parents, Sam and Joy.

Acknowledgments

My thesis work has been funded in part by the Nuclear Regulatory Commission Graduate Fellowship, which I am very grateful to have received. I would like to thank my thesis committee for the helpful advice they offered during my preliminary examination. I would also like to thank Dr. Andrew Davis for many years of advice and wisdom, and his amazing ability to fix anything broken. I thank Prof. Anthony Scopatz for his inspiring degree of software development expertise and shaping me into a better programmer one pull request at a time. I thank Dr. Ahmad Ibrahim for teaching me the ropes on the theory side and helping me improve my technical writing. Finally, I would like to extend my deepest gratitude to my advisor, Prof. Paul Wilson. Paul has been more than an academic advisor to me, but a figure whose patience, wisdom, and leadership have set a standard which I aspire to achieve.

Contents

List of Tables

List of Figures

Abstract

The operation of fusion energy systems (FES) results in neutron activation of system components. Radionuclides produced in this process persist after the device is shutdown and emit photons as they decay. It is necessary to quantify the potential dose rate from these photons as a function of position and time after shutdown for maintenance planning and licensing purposes. This shutdown dose rate (SDR) is calculated by coupling neutron transport, activation analysis, and photon transport. The size, complexity, and attenuating configuration of FES motivates the use of hybrid Monte Carlo (MC)/deterministic neutron transport. The Multi-Step Consistent Adjoint Driven Importance Sampling (MS-CADIS) method is a method for optimizing MC neutron transport for coupled multiphysics problems, including SDR analysis, using deterministic estimates of adjoint flux distributions. MS-CADIS requires the formulation of an adjoint neutron source that approximates the transmutation process.

In this work, transmutation approximations and assumptions are described that allow for the derivation of an approximate solution for the MS-CADIS adjoint neutron source for SDR analysis. These assumptions are collectively referred to as the Single Neutron Interaction and Low Burnup (SNILB) criteria, and result in the SNILB solution for the adjoint neutron source. A heuristic method is proposed for determining the extent to which the SNILB criteria are met. It is shown that the SNILB criteria are reasonably met for typical FES neutron spectra and materials over a range of irradiation scenarios. The Groupwise Transmutation (GT)-CADIS method is proposed: an implementation of the MS-CADIS method for SDR analysis that uses single-energy-group irradiations to generate an adjoint neutron source that is equivalent to the SNILB solution when the SNILB criteria are met. The GT-CADIS method is demonstrated with a simple SDR problem. Speedups of 200 ± 100 are obtained relative to the Forward Weighted (FW)-CADIS global variance reduction technique and $9 \pm 5 \cdot 10^4$ relative to analog.

For special cases when the SNILB criteria are not met, a suite of methods referred to as

SNILB-violation methods are proposed for resolving the MS-CADIS adjoint neutron source for SDR analysis. An SDR problem was constructed where the SNILB criteria are egregiously violated and a subset of SNILB-violation methods are shown to provide improvements over the GT-CADIS method in this case. Finally, the GT-CADIS method is applied to a problem involving a Princeton Plasma Physics Laboratory (PPPL) Spherical Tokamak (ST) Fusion Nuclear Science Facility (FNSF) device. This work shows that the MS-CADIS method for SDR analysis and specifically the GT-CADIS implementation are broadly applicable to FES problems, provide a significant speedup that will drastically reduce the computational resources necessary for SDR analysis, and are ready for production-level use.

Chapter 1

Introduction

Fusion energy systems (FES) describe a class of experimental and conceptual devices that use the fusion of atomic nuclei to generate heat with the ultimate goal of producing electricity for commercial consumption. The fusion of two nuclei requires overcoming the tremendous electrostatic force that exists between them. With thermonuclear fusion this force is overcome by heating fuel in the plasma state to temperatures that exceed 10^8 K. Leading concepts for thermonuclear fusion systems include tokamaks and stellerators, which use magnetic fields to confine these plasmas within toroidal vacuum vessels. The design and operation of experimental devices — such as the Joint European Torus (JET) [1], Wendelstein 7-X [2], and ITER [3] — requires surmounting a variety of engineering challenges.

One such challenge is the production of radionuclides within the components of these reactors. Though the future may hold several viable options for fusion fuel, the fusion of deuterium and tritium (D-T) is the easiest to achieve. Each D-T reaction produces a high-energy neutron (14.1 MeV). These neutrons penetrate deep into system components. Nuclear reactions between neutrons and system components produce radionuclides which persist after neutron-producing operations cease. These radionuclides emit high-energy (0.01 – 10 MeV) photons as they decay. Maintenance operations may require personnel to be in the vicinity of these activated components. It is therefore necessary to quantify the potential dose rate from photons emitted from these radionuclides as a function of position and time after shutdown. Precise quantification of this shutdown dose rate (SDR) is necessary to ensure occupational safety, minimize the downtime of the device from cooldown before maintenance, and carry out licensing activities.

The quantification of the SDR is made possible by high-fidelity computational simulations. The foremost method for obtaining these estimates is the Rigorous 2-Step (R2S) method [4].

With this method a neutron transport simulation is first performed in order to acquire a multigroup neutron flux distribution throughout the reactor geometry within discrete spatial regions (either geometry cells or a mesh). A dedicated nuclear inventory analysis code is then used to simulate the irradiation of the material within each spatial region when subjected to the neutron flux for some irradiation and decay scenario of interest. This yields an energywise photon emission density within each spatial region, which is then used to define a source for a photon transport simulation. Flux-to-dose-rate conversion factors can be used to convert the resulting photon flux distributions to SDR distributions.

Monte Carlo radiation transport is typically used for both R2S transport steps [5, 6, 4, 7, 8, 9] due to the degree of accuracy required for SDR estimation. MC transport is a stochastic method that involves simulating random walks of particles through space/energy phase space. This allows for continuous (i.e., not discrete) treatment of particle position, direction, and energy. However, MC results must be obtained within discrete phase space regions, known as tallies, and these results have associated statistical uncertainties. Simulation of transport through the highly-attenuating geometries encountered in FES requires the use of MC variance reduction (VR) techniques in order to obtain results with satisfactory statistical uncertainty in reasonable computer processor time. VR techniques modify particle behavior in order to preferentially sample behavior that results in MC tally scores, accelerating the convergence of results.

Deterministic radiation transport methods involve spatial, angular, and energy discretization, yielding particle flux distribution equations that can be solved numerically. In contrast to MC methods, deterministic methods are ideally suited for resolving particle flux distributions that span many orders of magnitude, as encountered within FES problems. However, the discretization process introduces significant systematic error into results. Reducing this systematic error requires increasing the resolution of the discretization (i.e., a finer mesh, more angular groups, more energy groups), which increases computer memory requirements. FES are large, geometrically complex, and contain regions were particle streaming is important.

As a result, computer memory limitations do not permit full-scale analysis of FES to be done with the resolution necessary to obtain results with sufficiently low systematic error.

Though full-scale FES analysis with deterministic transport is not feasible, deterministic methods can be used to quickly (i.e., with less computer processor time than MC transport) obtain approximate particle flux distributions which can be used for MC VR. The Consistent Adjoint Driven Importance Sampling (CADIS) method [10] is one such hybrid MC/deterministic method that allows for high-resolution results to be obtained using MC transport with a speedup from a deterministic transport preprocessing step. With this method, MC transport is optimized with respect to a detector response function. This detector is used as an adjoint source for deterministic adjoint transport. The resulting adjoint flux distribution — which provides an estimate of the importance of phase space regions to the detector response—is used to define MC weight windows and biased source distributions that optimize MC transport with respect to the detector. The Forward-Weighted (FW)-CADIS method [11] uses an additional deterministic estimate of the forward flux to generate an adjoint source to be used with the CADIS method to optimize MC transport with respect to multiple detectors simultaneously. The FW-CADIS method can also be used to optimize MC transport with respect to all of space (or phase space) for the purpose of global VR. These methods have been shown to drastically improve the efficiency of MC simulations for large-scale fusion applications [12] which motivates the application of these methods to SDR analysis problems.

For R2S photon transport the standard CADIS or FW-CADIS method can be applied in order to optimize photon transport for local or global SDR calculations [5]. For R2S neutron transport, global VR techniques have previously been used to evenly distribute MC neutrons throughout all of space or phase space [5, 13]. FW-CADIS could be used in order to optimize radiation transport using this approach. However, this global approach is computationally wasteful because not all regions of neutron phase space are of equal importance to the photon SDR. Instead, neutrons should be preferentially directed to regions of phase space where material becomes activated and produces photons at decay times of interest that are

important to photon dose rate detector(s). The Multi-Step (MS)-CADIS method [14, 15] defines an adjoint neutron source (i.e., a detector response function) that, when used with the CADIS method, achieves this optimal neutron biasing. However, a solution for this adjoint neutron source requires a quantity, defined as T, that relates neutron flux to decay photon emission density. An expression for T is not attainable for arbitrary transmutation networks and irradiation scenarios, so transmutation approximations must be made.

The principle goal of this work is to develop approximate solutions for T for the MS-CADIS adjoint neutron source and characterize the applicability and performance of these techniques. Chapter 2 first provides background on radiation transport, nuclear inventory analysis, SDR analysis, and the MS-CADIS method. Chapter 3 discusses the Single Neutron Interaction and Low Burnup (SNILB) solution for T. This approximate solution is valid when a set of criteria referred to as the SNILB criteria are met. Chapter 4 first describes the Groupwise Transmutation (GT)-CADIS method, an implementation of the MS-CADIS method for SDR analysis that involves calculating T via a series of irradiations with neutrons in a single energy group, performed as a preprocessing step. This procedure produces T that are equivalent to the SNILB solution when the SNILB criteria are met. A suite of methods are also proposed in cases where the SNILB criteria are not met, referred to as SNILB-violation methods. These methods involves calculating T by carrying out irradiations with multiple neutron energy groups simultaneously and/or with *a priori* knowledge of the neutron spectra within a problem.

Chapter 5 describes the software used to conduct the numerical experiments in this work. Chapters 6–9 describe these numerical experiments. In Chapter 6 the SNILB criteria are evaluated for typical FES materials and neutron spectra over a range of irradiation and decay scenarios. In Chapter 7 the efficacy of the GT-CADIS method is demonstrated relative to FW-CADIS and analog transport for a simple problem where the SNILB criteria are met. In Chapter 8, a problem is constructed where the SNILB criteria are egregiously violated and SNILB-violation methods are shown to provide improved performance compared to

GT-CADIS. Finally, in Chapter 9 the GT-CADIS method is applied to a production-level problem involving a Princeton Plasma Physics Laboratory (PPPL) Spherical Tokamak (ST) Fusion Nuclear Science Facility (FNSF) device [16] in order to show that the method is ready for production-level use.

Chapter 2

Background

This work focuses on the application of hybrid Monte Carlo (MC)/deterministic radiation transport techniques to SDR analysis. This chapter provides the theoretical and practical background for these two topics. Radiation transport for fusion shielding applications is first discussed including deterministic and MC solution methods, MC VR, and hybrid MC/deterministic methods. Nuclear inventory analysis is then discussed, followed by SDR analysis methods that couple nuclear inventory analysis with radiation transport. Finally, the MS-CADIS method is introduced.

2.1 Radiation Transport for Fusion Shielding Applications

The design and operation of FES requires detailed knowledge of particle flux distributions throughout the device. In the case of SDR analysis, neutron flux distributions are necessary to quantify the nuclear activation of system components. Photon flux distributions are required to assess the dose rate resulting from these activated components within regions of interest. This section describes the theory and methods for ascertaining these distributions.

2.1.1 The Linear Boltzmann Equation

The steady state distribution of neutrons and photons within FES can be described by a form of the linear Boltzmann Equation [17] as given by

$$\Big(\hat{\Omega}\cdot\vec{\nabla}+\Sigma(\hat{r},E)\Big)\psi(\hat{r},\hat{\Omega},E)= \tag{2.1}$$
$$q(\vec{r},\hat{\Omega},E)+\int_{E'}\mathrm{d}\,E'\int_{4\pi}\mathrm{d}\,\Omega'\Sigma_s(\hat{r},E'\rightarrow E,\hat{\Omega}'\cdot\hat{\Omega})\psi(\hat{r},\hat{\Omega},E).$$

In Equation 2.1, $\psi(\vec{r},\hat{\Omega},E,t)$ represents the particle flux as a function of a three-dimensional position vector ($\vec{r}$), a two-dimensional direction vector ($\hat{\Omega}$), and energy (E). The total macroscopic cross section is denoted by $\Sigma(\hat{r},E)$. The $q(\vec{r},\hat{\Omega},E)$ is a fixed external source (e.g., neutrons from a burning/ignited plasma, decay photons from activation products). The $\Sigma_s(\hat{r},E'\rightarrow E,\hat{\Omega}'\cdot\hat{\Omega})$ is the double-differential scattering cross section: the cross section of a particle of energy E' and direction $\hat{\Omega}'$ scattering into energy E at some angle θ where $\cos(\theta)=\hat{\Omega}'\cdot\hat{\Omega}$. It is often convenient to write the transport equation in terms of the transport operator $\mathcal{H}$ as seen in Equation 2.2. The $\mathcal{H}$ captures the behavior of all particle interactions in a single term:

$$\mathcal{H}=\hat{\Omega}\cdot\vec{\nabla}+\Sigma(\hat{r},E)-\int_{E'}\mathrm{d}\,E'\int_{4\pi}\mathrm{d}\,\Omega'\Sigma_s(\hat{r},E'\rightarrow E,\hat{\Omega}'\cdot\hat{\Omega}). \tag{2.2}$$

The transport equation can then be written in operator notation as:

$$\mathcal{H}\psi(\hat{r},\hat{\Omega},E)=q(\vec{r},\hat{\Omega},E). \tag{2.3}$$

2.1.2 The Adjoint Transport Equation

The adjoint flux (ψ^+), is a quantity of interest to FES analysis because under certain circumstances (explained below) ψ^+ defines the importance of regions of phase space to the response of a detector. This is useful for MC VR methods that aim to optimize the convergence of the solution of the transport equation relative to a detector response function. Mathematically, ψ^+ is defined as the quantity that satisfies the following adjoint identity:

$$\langle \psi^{+} \mathcal{H} \psi \rangle = \langle \psi \mathcal{H}^{+} \psi^{+} \rangle, \tag{2.4}$$

where $\mathcal{H}^{+}$ is the adjoint of the transport operator and $\langle \cdot \rangle$ denotes integration over all phase space. The $\mathcal{H}^{+}$ and ψ^{+} can be related by the adjoint transport equation:

$$\mathcal{H}^{+} \psi^{+} = q^{+}, \tag{2.5}$$

where q^{+} is the adjoint source. Just as the forward (i.e., not adjoint) flux is dependent on the forward external source q, the adjoint flux is dependent on q^{+}. In the case when q^{+} is chosen to be equivalent to a forward detector response function σ_d, the resulting adjoint flux denotes the importance of a region of phase space to σ_d [18].

For a given detector response function, the response (R) is:

$$R = \langle \psi \sigma_d \rangle. \tag{2.6}$$

The adjoint identity given in Equation 2.4 can be simplified using Equations 2.3 and 2.5 yielding:

$$\langle q^{+} \psi \rangle = \langle q \psi^{+} \rangle, \tag{2.7}$$

which allows for an alternative formulation of the response:

$$R = \langle \psi^{+} q \rangle. \tag{2.8}$$

This means that the response can be known for any source once the adjoint flux for a given detector is resolved. The adjoint flux for a given detector and the forward flux can be combined to give the contributon flux (ψ^{c}) as shown in Equation 2.9 [19].

$$\psi^{c} = \psi \cdot \psi^{+} \tag{2.9}$$

The contributon flux can be thought of as a forward flux where only particles that ultimately contribute to a detector are counted. Contributon flux distributions are useful for determining the pathways particles take to reach a given detector.

2.1.3 Deterministic Radiation Transport

Though analytic solutions to the forward and adjoint transport equations are possible for simple configurations, the complexity of nuclear systems has necessitated the development of numerical techniques for most practical applications. Deterministic radiation transport methods involve discretizing space, energy, and direction in order to obtain an approximate solution to Equation 2.3. The term "deterministic" is used in contrast to the stochastic MC method discussed in Section 2.1.4. A multitude of deterministic methods exist and are used in different applications [17]. One of the most prominent methods is the discrete ordinates (S_N) method, which solves the transport equation along discrete angles.

The S_N method relies on the multigroup approximation, which divides energy into G groups. For each energy group (g), the group fluxes are given by

$$\psi_g(\hat{r},\hat{\Omega}) = \int_{E_{g+1}}^{E_g} \psi(\hat{r},\hat{\Omega},E)\,dE. \tag{2.10}$$

The group quantities for total absorption cross section, scattering cross section from $g' \rightarrow g$, and source density, denoted by $\Sigma_g(\hat{r})$, $\Sigma_{s,gg'}(r,\hat{\Omega}\cdot\hat{\Omega}')$, and $q_g(\hat{r},\hat{\Omega})$, respectively are similarly obtained by integrating continuous quantities over the energy group. This yields the multigroup representation of the transport equation [20]:

$$[\hat{\Omega}\cdot\hat{\nabla}+\Sigma_g(\hat{r})]\psi_g(\hat{r},\hat{\Omega}) = \sum_{g'}\int_{4\pi}\Sigma_{s,gg'}(\hat{r},\hat{\Omega}\cdot\hat{\Omega}')\psi_{g'}(\hat{r},\hat{\Omega}')d\,\hat{\Omega}' + q_g(\hat{r},\hat{\Omega}). \tag{2.11}$$

The $\Sigma_{s,gg'}(\hat{r},\hat{\Omega}\cdot\hat{\Omega}')$ is a nontrivial function of $\hat{\Omega}$ which can be approximated using a truncated

Legendre expansion. This provides a starting point for the S_N method, which proceeds by solving along N discrete angles, which form a quadrature set. A spatial differencing scheme is used to relate flux in neighboring discrete spatial regions. The S_N method then obtains a flux distribution using an iterative method. In each iteration, fluxes are obtained for each phase space region using an estimate of the scattering source. The flux distribution is then used to improve the estimate of the scattering source for the next iteration. This process is repeated until some convergence criteria are met. The notation "$P_L S_N$" is often used to describe the parameters used for S_N methods, where L represents the number of terms in the truncated Legendre polynomial expansion.

S_N methods (and deterministic methods in general) can be used to quickly obtain global flux distributions and other quantities with the sacrifice in accuracy from the aforementioned discretizations. The resolution of S_N methods is often bound by computer memory, as the solution method requires the storage of cross sections and angular multigroup fluxes for each ordinate within each mesh volume element. S_N methods are poorly suited for transport problems where streaming plays a large role. The limited number of discrete angles can yield artifacts known as "ray effects": artificially high flux along quadrature ordinates, especially in (near-)void regions. In addition, particle streaming down ducts may be poorly represented if the duct does not happen to be aligned with an angle in the quadrature set. These effects limit the use of S_N methods for shielding calculations for FES, which involve particles born in near-vacuum and extensive streaming through narrow channels.

This work utilizes the PARallel TIme-dependent SN (PARTISN) [21] 3D Cartesian S_N code developed at Los Alamos National Laboratory (LANL). PARTISN can solve both forward and adjoint transport problems and is parallelized via Message Passing Interface (MPI). Computational tools have been created to handle PARTISN input and output as discussed in Section 5.2.

2.1.4 Monte Carlo Radiation Transport

MC radiation transport is a stochastic method that involves simulating particles using a random walk method. Particle birth and interactions are described using probability density functions (PDFs). Pseudo-random numbers are generated to sample these PDFs to move the particle through phase space until it is absorbed or otherwise terminated. Quantities such as flux and current can be ascertained using tallies, which record the behavior of particles as they travel through a region of phase space. Each such event (a tally score) constitutes a random sample of the underlying (unknown) response PDF, and a sufficiently large collection of these events can be averaged together to obtain a converged result.

MC radiation transport is generally more accurate than deterministic methods because it does not require discretization in space, energy, or direction. Though lack of phase space discretization reduces systematic errors from modeling that are intrinsic to deterministic calculations, results from MC simulations have an associated statistical error. The statistical error is typically quantified using the relative error R. The relative error is given by

$$R = \frac{1}{\bar{x}} \frac{S_x}{\sqrt{N_{\text{scores}}}}, \tag{2.12}$$

where $\bar{x}$ is the mean of the tally scores, S_x is the standard deviation of the tally scores, and N_{scores} is the number of tally scores. In MC, the R is used not only to quantify stochastic uncertainty, but also as a convergence test. Relative errors must be less than 0.1 to be considered "generally reliable" [22]. The efficiency of an MC simulation is measured by how quickly a simulation can achieve a sufficiently low R. The MC Figure of Merit (FOM) of a tally is defined by:

$$\text{FOM} = \frac{1}{R^2 t_{\text{proc}}}, \tag{2.13}$$

where t_{proc} is the processor time necessary to achieve a relative error R. The FOM is highly problem-dependent, and is also processor-dependent.

The high degree of accuracy required for the analysis of FES necessitates the use of MC radiation transport. This accuracy comes at the price of long convergence times compared to deterministic methods. This is mitigated through the use of MC VR (as discussed in the following section) as well as parallelization. MC methods are "embarrassingly parallelizable" — particles can be simulated independently from one another on many processors in parallel with minimal interprocess communication or overhead. Results from particles simulated on many processors simultaneously can then be combined using appropriate statistical methods.

This work utilizes the MCNP5 transport code, developed at Los Alamos National Laboratory [22]. MCNP5 is a continuous-energy MC code for neutron, photon, and electron transport. In MCNP5, a text-based Constructive Solid Geometry (CSG) language is used to define geometry cells and surfaces. However, due to the tremendous complexity of FES, geometries are typically created using Computer Aided Design (CAD) software. In many cases, CAD models already exist for device assembly purposes so it is desirable to use these same models for neutronics analysis as well.

Radiation transport can be performed directly on CAD geometry using DAG-MCNP5, a modified version of MCNP5 that uses the Direct Accelerated Geometry Monte Carlo (DAGMC) toolkit [23] (a component of the Mesh Oriented dataABase (MOAB) library [24]) for particle tracking. CUBIT CAD software [25] can be used to create CAD geometry for use with DAG-MCNP5. DAG-MCNP5 has been used for 3D analysis of FES including ITER, ARIES, and FNSF [26].

2.2 Monte Carlo Variance Reduction

The deep-penetration shielding problems encountered in FES are problematic for analog MC transport (i.e., MC transport without VR). In analog MC simulations, particle birth positions, energies, directions, and all subsequent interactions are simulated by sampling the unbiased PDFs that represent these phenomena. This means that regions of phase space

with high particle flux are sampled more frequently then regions of low particle flux. This results in prohibitively-low convergence rates for tallies in regions where the flux is highly attenuated, commonly found in FES scenarios.

MC VR refers to a class of methods that improve the efficiency of MC calculations by modifying particle behavior (e.g., by biasing PDFs that govern particle behavior) in order to preferentially sample events that result in tally scores. The statistical weight of particles must then be adjusted in order to play a "fair game" — that is, to ensure that a systematic bias is not being introduced into the result. The following relationship between biased and unbiased PDFs (denoted by $\mathfrak{p}$) and statistical weight (w) guarantees a fair game:

$$w_{\text{biased}}\,\mathfrak{p}_{\text{biased}} = w_{\text{unbiased}}\,\mathfrak{p}_{\text{unbiased}}\,. \tag{2.14}$$

The sampling of the biased PDFs can increase the FOM by either increasing the rate of tally scores (thereby increasing N_{scores} in Equation 2.12) or decreasing the standard deviation in tally scores S_x, which is a function of statistical weight. Most MC VR methods affect both quantities.

Techniques to choose $\mathfrak{p}_{\text{biased}}$ can be thought of in terms of two classes of MC problems. In target-based problems, low-variance results are desired for one or more tallies, which typically occupy a small region of phase space (contiguous or disparate) relative to the phase space of the problem. For example, the nuclear heating in a single component or the prompt dose rate to an operator may need to be estimated. In global MC simulations, low-variance results are desired uniformly throughout space or phase space. This may be useful for estimating dose rates throughout an entire facility. Global problems can be thought of as a special case of target-based problems, where the target is a response function chosen to yield uniform sampling of space or phase space. Nonetheless, the distinction between global and target-based problems is useful in the discussion of different MC VR techniques.

2.2.1 Source Biasing and Particle Splitting

Industry-standard MC codes typically contain a suite of VR methods [10]. Historically, using these methods has required an experienced analyst. Automated VR refers to methods that can increase the FOM of a tally with minimal judgment from the analyst. Two such VR methods often used as components of these schemes are source biasing and splitting/rouletting.

All MC sources are defined by PDFs. Source biasing is the process in which a biased source PDF is sampled instead of the source PDF, and statistical weight of particles born is adjusted using Equation 2.14. This method is particularly useful when phase space regions with the highest source intensity are not major contributors to the tally or tallies of interest.

Particle splitting is a population control method where a single particle is split into multiple particles — each of reduced statistical weight — upon entering a region of phase space. When a single particle is split into N particles each of weight w_{biased}, the follow relation must be satisfied:

$$\mathsf{N} \times w_{\text{biased}}\, \mathfrak{p}_{\text{biased}} = w_{\text{unbiased}}\, \mathfrak{p}_{\text{unbiased}}\,. \tag{2.15}$$

If used correctly, particles split when moving from one region of phase space to a more important one. Splitting is used in combination with Russian roulette: when a particle moves in the opposite direction, from an important region to a less important one, it is terminated with a probability that is reciprocal to N. In MCNP5 the "weight window game" is a splitting/rouletting implementation. A weight window is a range of weights with an upper and lower bound, that can be assigned spatially to geometry cells or a superimposed mesh, and to energy bins. When a particle enters such a phase space region, its weight is unmodified if it is within the window. If it is above or below the window it is split or rouletted appropriately. Automatic VR parameter generation schemes can be used to generate weight window lower bounds (often referred to as simply "weight windows" for short) and/or source biasing parameters, typically using some problem-specific information obtained via a

preprocessing step. Two of these methods are discussed in Section 2.2.2.

2.2.2 CADIS and FW-CADIS

CADIS and FW-CADIS are hybrid MC/deterministic methods that generate MC weight windows and biased sources using a deterministic estimate of the adjoint flux in order to maximize the FOM of a tally. The tally of interest defines the adjoint source and adjoint transport is carried out. The response can be formulated as a function of the resulting estimate of the adjoint flux:

$$R = \int_{4\pi}\int_{E}\int_{V} \psi^{+}(\vec{r}, E, \hat{\Omega})\, q(\vec{r}, E, \hat{\Omega})\, d\vec{r}\, dE\, d\hat{\Omega}. \tag{2.16}$$

Weight window lower bounds are then given by:

$$w_l(\vec{r}, E) = \frac{R}{\left(\frac{1+\beta}{2}\right)\psi^{+}(\vec{r}, E)}, \tag{2.17}$$

where β is the ratio of weight window upper bound to lower bound (default of 5 for MCNP5). The corresponding biased source distribution is

$$\hat{q}(\vec{r}, E) = \frac{\psi^{+}(\vec{r}, E)\, q(\vec{r}, E)}{R}. \tag{2.18}$$

This biased source is defined "consistently," such that particles are born within the weight window for the birth location and energy. The CADIS method is useful when optimizing the results of a single detector response function. In many cases, it may be necessary to simultaneously optimize several detector response functions. The FW-CADIS method defines an adjoint source that, when used with the CADIS method, will optimize multiple detector response functions. This adjoint source is given as:

$$q^{+}(\vec{r}, E) = \sum_{i} \frac{\sigma_{d,i}(\vec{r}, E)}{R_i}, \tag{2.19}$$

where $\sigma_{d,i}$ is the detector response function for the i^{th} detector and each response R_i is calculated from a deterministic estimate of the forward flux. The FW-CADIS method can be used for global VR by defining a mesh tally covering the entire geometry as a detector. If uniform relative error is also desired across all energy groups, the response is set equal to the energy-wise flux, and $\sigma_{d,i}$ is 1 for all i. In this case, the adjoint source is simply

$$q^{+}(\vec{r}, E) = \frac{1}{\phi(\vec{r}, E)}. \tag{2.20}$$

2.3 Nuclear Inventory Analysis

When a material is irradiated with neutrons, a complex network of reaction pathways is populated, producing radionuclides. These pathways may involve reactions with neutrons directly, which occur only during operation when neutrons are being produced, or decay processes that occur both during the operation of the device and after shutdown. For SDR analysis, the nuclear inventory must be known precisely in order to quantify the photon emission density as a function of time after shutdown. The production and destruction of nuclides can be modeled mathematically, allowing for the nuclear inventory to be discerned for arbitrary irradiation and decay scenarios [27].

2.3.1 Mathematical Model

The rate in which a nuclide i undergoes reactions or decay to some other nuclide j is proportional to its concentration. For nuclear reactions, the production rate constant (P) is

$$P_{i \to j,\,\text{reaction}} = \int_{E_n} \sigma_{i \to j}(E_n)\phi_n(E_n)\mathrm{d}\,E_n, \tag{2.21}$$

where $\phi_n(E_n)$ is the neutron flux for neutron energy E_n and $\sigma_{i \to j}(E_n)$ is the microscopic cross section for the reaction that transforms nuclide i into j. For decay processes, the

proportionality constant is

$$P_{i\to j,\,\mathrm{decay}} = \lambda_i b_{i\to j}, \tag{2.22}$$

where λ_i is the decay constant for i and $b_{i\to j}$ is the branching ratio for the pathway that produces j. It is convenient to represent both of these $i \to j$ rates within the single term:

$$P_{i\to j,\,\mathrm{total}} = P_{i\to j,\,\mathrm{reaction}} + P_{i\to j,\,\mathrm{decay}}. \tag{2.23}$$

The rate of change in the concentration of any nuclide (N_i) with respect to time is the difference in the rate of production and destruction of that nuclide:

$$\frac{d\,N_i(t)}{d\,t} = \sum_j N_j(t) P_{j\to i,\,\mathrm{total}} - \sum_j N_i(t) P_{i\to j,\,\mathrm{total}}. \tag{2.24}$$

For an entire network of nuclides and pathways, this can be expressed as a system of first-order linear differential equations, given by:

$$\frac{d\,\vec{N}(t)}{d\,t} = \mathbf{A}\vec{N}(t), \tag{2.25}$$

where $\vec{N}(t)$ is a vector of all nuclide concentrations as a function of time and $\mathbf{A}$ is the transfer matrix of production/destruction rates. The solution to this equation is the matrix exponential:

$$\vec{N}(t) = e^{\mathbf{A}t}\vec{N}_0. \tag{2.26}$$

Analysis of the nuclear inventory of FES requires the modeling of complex irradiation scenarios which involve sequential periods of device on-time and off-time which have unique $\mathbf{A}$ matrices. For an arbitrary irradiation scenario $\vec{N(t)}$ can be obtained by solving Equation 2.26 for each period within the scenario, with $\vec{N}_0$ being the inventory from the end of the previous period.

Since **A** is large (perhaps as large as 2000 × 2000 [27]) and sparsely filled, simplifying assumptions are often made to solve Equation 2.26. For example, a truncated series expansion can be used to approximate the matrix exponential. Transmutation chains that contain loops or cross-links can be straightened to form smaller or simpler systems. The straightening of transmutation chains also allows for the application of the analytic solution of nuclide concentrations within linear chains (as discussed in the next section). Other methods involve approximating the derivative (the RHS of Equation 2.25) by iteratively solving for many small time steps. Each method has trade-offs in accuracy, processor time, and computer memory.

This work uses the Analytic and Laplacian Adaptive Radioactivity Analysis (ALARA) activation code developed at the University of Wisconsin - Madison [28]. ALARA adaptively chooses a solution method based on the characteristics of the problem and allows for activation problems to be performed in a large number of material/flux regions within a single code execution. The computational efficiency of ALARA facilitates mesh-based activation analysis, characterized by 10^5 – 10^7 activation problems.

2.3.2 Linear Transmutation Chains

One method of solving Equation 2.26 is to decompose the transmutation network into a collection of linear chains in the form:

$$\mathsf{N}_1 \rightarrow \cdots \rightarrow \mathsf{N}_\mathrm{i} \rightarrow \cdots \rightarrow \mathsf{N}_\mathrm{I}. \tag{2.27}$$

This can be done for arbitrary transmutation networks, as will be shown in Section 3.1. Modeling transmutation networks as a collection of linear chains greatly simplifies Equation 2.26. For these chains the **A** matrix is bidiagonal which allows for a solution to Equation 2.26 in the form of the Bateman equation [29]:

$$N_i(t) = N_i(0)e^{-d_i t} + \sum_{j=1}^{i-1} N_j(0) \left[\sum_{k=j}^{i-1} \left[\frac{P_{k+1}(e^{-d_k t} - e^{-d_i t})}{d_i - d_k} \prod_{\substack{l=j, \\ l \neq k}}^{i-1} \frac{P_{l+1}}{d_l - d_k} \right] \right], \tag{2.28}$$

where P_k is the production rate of nuclide k (i.e., $P_{k-1 \rightarrow k}$), d_k is the destruction rate of k (i.e., $P_{k \rightarrow k+1} + \lambda_k$), and $N_i(0)$ and $N_j(0)$ are the initial concentrations of nuclides i and j, respectively.

2.4 Shutdown Dose Rate Analysis

In FES, neutrons activate system components and the dose rate from photons emitted from these components must be estimated as a function of position and time after shutdown. This dose rate may be one of several radiological quantities of interest. For this work, the SDR will be quantified using a set of ICRP-74 [30] flux-to-dose rate conversion factors recommended by the ITER organization [31]. This particular set provides the effective dose rate ("the sum of the weighted equivalent dose [rates] in all the tissues and organs of the body" [30]), resulting from antero-posterior (AP) irradiation. In this section two methods that couple particle transport and nuclear inventory analysis in order to estimate the SDR are discussed: the Direct 1-Step (D1S) method [32, 33] and the Rigorous 2-Step (R2S) method [4].

2.4.1 Direct 1-Step Method

Industry standard MC codes such as MCNP5 allow for simultaneous transport of neutrons and prompt photons resulting from (n, γ) reactions. The prompt photon emission density $q_p(E_p)$ that results from neutron flux $\phi_n(E_n)$ is given by:

$$q_p(E_p) = \int_{E_n} \sigma_{(n,\gamma)}(E_n, E_p)\phi_n(E_n) \mathrm{d}\, E_n, \tag{2.29}$$

where ($\sigma_{(n,\gamma)}$) is the prompt photon production cross section.

Conceptually, with the D1S method $\sigma_{(n,\gamma)}$ is replaced with a function that converts neutron flux to decay photon emission density. Then a single transport simulation is performed for both neutrons and photons. Photon fluxes can be tallied in the region of interest and flux-to-dose-rate conversion factors can be used to obtain the SDR. D1S allows for photon source density to be continuous in space without any cell- or mesh-based discretization. D1S is not well-suited to applications where the geometry changes between activation and decay.

The principle challenge with the D1S method is producing modified cross sections. To date, the methods proposed (in published work) have only considered single-step reactions for a small subset of nuclides within a problem [33]. No method has been proposed for generating modified cross sections for arbitrary transmutation networks with multistep reactions which may include loops and branches. These cross sections can be related to the MS-CADIS method, as further discussed in Section 2.5.

2.4.2 Rigorous 2-Step Method

The R2S method involves two separate transport steps. Neutron transport is first performed and the neutron flux is tallied using some spatial discretization, either geometry cells or a superimposed mesh [7], as well as energy discretization (i.e., energy bins). Using these neutron fluxes and the irradiation scenario of interest, an activation calculation is carried out in each region using a dedicated nuclear inventory analysis code to give the photon source density in the region as a function of the decay time. This is then used as a source for photon transport, where the SDR is tallied using a detector modified with flux-to-dose-rate conversion factors. The R2S method will be used exclusively in this work.

2.5 MS-CADIS

SDR analysis often involves estimating the dose rate through thick shielding, in places where personnel are likely to spend significant time, which necessitates the use of MC VR. With the R2S method, MC VR is typically required for both neutron and photon transport. For photon transport either target-based or global VR techniques can be used depending on where SDR estimates are needed. The CADIS and FW-CADIS methods can be used in these two cases respectively to produce optimal weight windows and biased sources.

For R2S neutron transport analysts have previously used target-based VR techniques such as the MCNP weight window generator [4, 9], and manually generated cell-based importances [8] for MC neutron transport. These methods requires analysts to guess what regions of neutron phase space are important to the photon SDR and are unlikely to result in optimal importance sampling VR parameters. The Method of Automatic Generation of Importances by Calculation (MAGIC) [34] global VR technique has also been used for R2S neutron transport [5, 13]. Global VR techniques are computationally wasteful for SDR calculations, because not all phase space regions become activated and produce important decay photons.

The CADIS method can be used to optimize neutron transport for SDR calculations if an adjoint neutron source can be formulated that captures both the potential of regions of phase space to become activated and the importance of the resulting decay photons to the SDR detector. The MS-CADIS method, when applied to SDR analysis, provides an adjoint neutron source with these properties. The derivation of this adjoint neutron source is given below, adapted from Ibrahim et al. [14].

When applied to SDR analysis[1], the MS-CADIS method constrains the adjoint neutron source such that the neutron response is equivalent to the photon SDR for a fixed irradiation scenario. The formulation of the response in Equation 2.8 becomes (time notation suppressed):

[1]From this point forward, all references to MS-CADIS imply the application of the MS-CADIS method to SDR analysis, specifically.

$$SDR = \langle \phi_n(\vec{r},\, E_n)\,,\; q_n^+(\vec{r},\, E_n)\,\rangle. \tag{2.30}$$

The photon SDR can also be expressed in terms of the adjoint photon flux:

$$SDR = \langle \phi_p^+(\vec{r},\, E_p)\,,\; q_p(\vec{r},\, E_p)\,\rangle. \tag{2.31}$$

From Equations 2.30 and 2.31 it follows that:

$$\langle \phi_n(\vec{r},\, E_n)\,,\; q_n^+(\vec{r},\, E_n)\,\rangle = \langle \phi_p^+(\vec{r},\, E_p)\,,\; q_p(\vec{r},\, E_p)\,\rangle. \tag{2.32}$$

In order to solve Equation 2.32 for $q_n^+(\vec{r},\, E_n)$, the following relationship can be used, relating $\phi_n(\vec{r},\, E_n)$ to $q_p(\vec{r},\, E_p)$:

$$q_p(\vec{r},\, E_p) \;= \int_{E_n} T(\vec{r},\, E_n,\, E_p)\; \phi_n(\vec{r},\, E_n)\; dE_n\,. \tag{2.33}$$

The quantity $T(\vec{r},\, E_n,\, E_p)$ is defined by this relationship. Substituting Equation 2.33 into Equation 2.32 yields:

$$\int_{\vec{r}} \int_{E_n} \phi_n(\vec{r},\, E_n)\; q_n^+(\vec{r},\, E_n)\; dE_n\; d\vec{r} \;=$$

$$\int_{\vec{r}} \int_{E_p} \left(\int_{E_n} T(\vec{r},\, E_n,\, E_p)\; \phi_n(\vec{r},\, E_n)\; dE_n \right) \phi_p^+(\vec{r},\, E_p)\; dE_p\; d\vec{r}. \tag{2.34}$$

Switching the order of integration yields:

$$\int_{\vec{r}} \int_{E_n} \phi_n(\vec{r},\, E_n)\; q_n^+(\vec{r},\, E_n)\; dE_n\; d\vec{r} \;=$$

$$\int_{\vec{r}} \int_{E_n} \left(\int_{E_p} T(\vec{r},\, E_n,\, E_p)\; \phi_p^+(\vec{r},\, E_p)\; dE_p \right) \phi_n(\vec{r},\, E_n)\; dE_n\; d\vec{r}\,. \quad (2.35)$$

From this, the solution for the MS-CADIS adjoint neutron source is obtained:

$$q_n^+(\vec{r},\, E_n) = \int_{E_p} T(\vec{r},\, E_n,\, E_p)\; \phi_p^+(\vec{r},\, E_p)\; dE_p\,. \quad (2.36)$$

The $\phi_p^+(\vec{r},\, E_p)$ can be estimated deterministically given a final photon dose rate detector to use for $q_p^+(\vec{r},\, E_p)$. If a $T(\vec{r},\, E_n,\, E_p)$ can be found that satisfies Equation 2.33, then the $q_n^+(\vec{r},\, E_n)$ in Equation 2.36 can be used with the CADIS method to optimize neutron transport for SDR problems. A nascent implementation of the MS-CADIS method has previously been used to obtain modest speedups over the FW-CADIS method [14].

In the cases where the SDR is desired globally, an adjoint photon source that results in global VR can be used with the MS-CADIS method. This adjoint photon source can be obtained using a method similar to the FW-CADIS method. A forward neutron transport calculation must first be done. The resulting forward neutron fluxes are then used to obtain a forward photon source using activation calculations or more simply Equation 2.33. Using this forward photon source, forward photon transport is then done to obtain forward photon fluxes. Forward photon fluxes are then used to generate an adjoint photon source as is done with the FW-CADIS method. This adjoint photon source is used as a starting point for the MS-CADIS method.

The MS-CADIS adjoint neutron source has also been shown to be applicable to the process of propagating statistical error through an R2S calculation [14]. In addition, the MS-CADIS method can be related to the D1S method described in Section 2.4.1. Equation 2.33 is in the form of Equation 2.29, which means that if a suitable $T(\vec{r},\, E_n,\, E_p)$ can be found for use with the MS-CADIS method, this same function could potentially be used to replace prompt photon production cross sections for the D1S method. As will be discussed in Chapter 3, a solution for $T(\vec{r},\, E_n,\, E_p)$ cannot be obtained for general transmutation networks,

necessitating the approximation of the transmutation process.

Chapter 3

Solution for the MS-CADIS Adjoint Neutron Source

The MS-CADIS method can be used to optimize MC radiation transport for the neutron transport step of an R2S calculation provided that a suitable $T(\vec{r}, E_n, E_p)$ can be obtained, as defined in Equation 2.33. In order to understand when such an expression is attainable, $T(\vec{r}, E_n, E_p)$ at a single point is first considered, allowing for the removal of the dependence on $\vec{r}$. This gives the expression:

$$q_p(E_p) = \int_{E_n} T(E_n, E_p)\phi_n(E_n)\mathrm{d}\,E_n. \tag{3.1}$$

This equation can be expressed in terms of a function $f(\phi_n)$, which is nonlinear with respect to ϕ_n (notation abbreviated):

$$q_p = \int_{E_n} f(\phi_n)\mathrm{d}\,E_n, \tag{3.2}$$

The function $f(\phi_n)$ can be expressed as a Taylor series expansion around some flux, a:

$$f(\phi_n) = f(a) + \frac{f'(a)}{1!}(\phi_n - a) + \frac{f''(a)}{2!}(\phi_n - a)^2 \dots \tag{3.3}$$

where derivatives are with respect to ϕ_n. By setting a to 0, this expansion becomes:

$$f(\phi_n) = f(0) + \frac{f'(0))}{1!}(\phi_n) + \frac{f''(0)}{2!}(\phi_n)^2 \dots \tag{3.4}$$

The $f(0)$ term must be 0 because decay photons are the result of neutron interactions. If ϕ_n is sufficiently small (near $a = 0$) the $f''(0)$ term can be truncated yielding

$$f(\phi_n) \approx f'(0)\phi_n, \tag{3.5}$$

where $f'(0)$ can now be used for $T(E_n, E_p)$ in Equation 3.1.

In this chapter the function $f(\phi_n)$ is linearized with respect to ϕ_n in order to obtain an expression for $T(E_n, E_p)$, starting from first principles. In Section 3.1 the mathematical relationship between $q_p(E_p)$ and $\phi_n(E_n)$ is first put forth. In Section 3.2.1 it is shown that in the general case (i.e., arbitrary transmutation networks and irradiation scenarios) a relationship in the form of Equation 3.1 cannot be obtained. Section 3.2.2 shows that this expression can be satisfied when a set of assumptions and criteria, referred to as the Single Neutron Interaction and Low Burnup (SNILB) criteria, are valid. The SNILB criteria can be used to obtain solutions for $T(E_n, E_p)$, $T(\vec{r}, E_n, E_p)$, and the MS-CADIS adjoint neutron source. Section 3.3 describes a heuristic method for evaluating the extent to which the SNILB criteria are met.

3.1 Relating Neutron Flux and Photon Emission Density

In order to find a relationship between neutron flux and photon emission density in the form of Equation 3.1 (to obtain T for the MS-CADIS adjoint neutron source) the transmutation problem is formulated in terms of independent transmutation chains. This decomposition is shown in Figure 3.1. These chains, indexed by c take the form:

$$N_1 \rightarrow \cdots \rightarrow N_{i_c}. \tag{3.6}$$

Each chain has length i_c and therefore the final nuclide in each chain is N_{i_c}. For a simple irradiation and decay scenario consisting of an irradiation of time t_{irr} followed by a decay of time t_{dec} the photon emission density at time $t_{tot} = t_{irr} + t_{dec}$ can be expressed in terms of

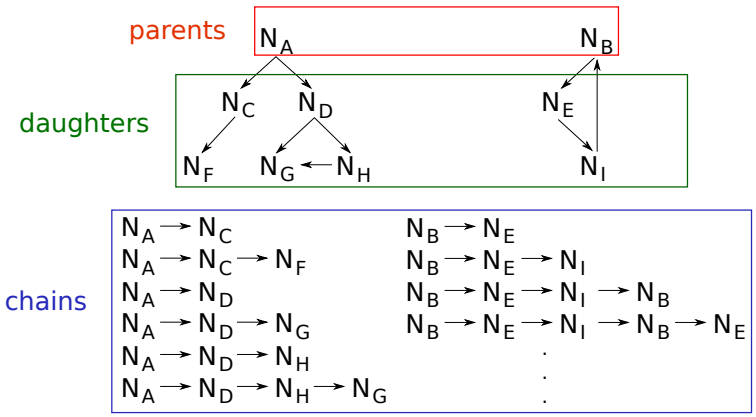

Figure 3.1: Decomposition of a transmutation network into chains.

contributions from the last nuclide within every chain in the network:

$$q_p(E_p, t_{tot}) = \sum_c \lambda_{c,i_c} b_{c,i_c}(E_p) N_{c,i_c}(t_{tot}). \tag{3.7}$$

Here, λ_{c,i_c} and $b_{c,i_c}(E_p)$ are the decay constant and branching functions for the nuclide i_c within chain c. This formulation has several important features. Consider the chain $N_A \to N_D \to N_G$ in Figure 3.1. The contribution of N_D and N_G to the photon emission density are formulated in terms of contributions from two separate chains. The contribution from N_D comes from the chain $N_A \to N_D$ with $i_c = 2$, and the contribution from N_G comes from $N_A \to N_D \to N_G$ with $i_c = 3$. The full contribution from N_G is obtained by including the other N_G production pathway: $N_A \to N_D \to N_H \to N_G$ with $i_c = 4$.

The only flux-dependent term in Equation 3.7 is $N_{c,i_c}(t_{tot})$. In order to obtain an expression in the form of Equation 3.1 this flux dependence must be expressed explicitly. The quantity $N_{c,i_c}(t_{tot})$ can be expressed in terms of $N_{c,i_c}(t_{irr})$ and $N_{c,j}(t_{irr})$ for $j \in [1, i_c - 1]$ — the compositions of the nuclides in chain c at the end of irradiation — with the Bateman equation (Equation 2.28), adapted here:

$$N_{c,i_c}(t_{tot}) = N_{c,i_c}(t_{irr}) e^{-d_{c,i_c} t_{dec}} \tag{3.8}$$

$$+\sum_{j=1}^{i_c-1} N_{c,j}(t_{irr})\left[\sum_{k=j}^{i_c-1}\left[\frac{P_{c,k+1}(e^{-d_{c,k}t_{dec}}-e^{-d_{c,i_c}t_{dec}})}{d_{c,i_c}-d_{c,k}}\prod_{\substack{l=j,\\ l\neq k}}^{i_c-1}\frac{P_{c,l+1}}{d_{c,l}-d_{c,k}}\right]\right].$$

It should be emphasized that the P and d terms here represent production and destruction during the decay interval (i.e., not production/destruction during irradiation) and are not flux-dependent. For convenience, the quantity within the larger set of square brackets in Equation 3.8 is renamed $B_{c,i_c,j}(t_{dec})$. This quantity represents the rate of production of nuclide i_c from nuclide j via chain c after a decay of time t_{dec}. This simplifies Equation 3.8 to:

$$N_{c,i_c}(t_{tot}) = N_{c,i_c}(t_{irr})e^{-d_{c,i_c}t_{dec}} + \sum_{j=1}^{i_c-1} N_{c,j}(t_{irr})B_{c,i_c,j}(t_{dec}). \tag{3.9}$$

The only quantities in Equation 3.9 that are flux-dependent are the nuclide concentrations. In order to obtain an expression in the form of Equation 3.1 the flux-dependence of the nuclide concentrations must take the form

$$N_{c,i}(t_{irr}) = \int_{E_n} U_{c,i}(E_n, t_{irr})\phi_n(E_n)\,dE_n, \tag{3.10}$$

where $U_{c,i}(E_n, t_{irr})$ is a function that is defined by this equation. Combining Equations 3.9 and 3.10 gives the following expression for $N_{c,i_c}(t_{tot})$:

$$N_{c,i_c}(t_{tot}) = \int_{E_n} \phi_n(E_n)\left[U_{c,i_c}(E_n, t_{irr})e^{-d_{c,i_c}t_{dec}} + \sum_{j=1}^{i_c-1} U_{c,j}(E_n, t_{irr})B_{c,i_c,j}(t_{dec})\right]dE_n. \tag{3.11}$$

This equation can be combined with Equation 3.7 to obtain an expression relating $q_p(E_p, t_{tot})$ and $\phi_n(E_n)$:

$$q_p(E_p, t_{tot}) = \sum_c \lambda_{c,i_c} b_{c,i_c}(E_p) \int_{E_n} \phi_n(E_n) \Bigg[U_{c,i_c}(E_n, t_{irr}) e^{-d_{c,i_c} t_{dec}} + \sum_{j=1}^{i_c-1} U_{c,j}(E_n, t_{irr}) B_{c,i_c,j}(t_{dec}) \Bigg] dE_n. \tag{3.12}$$

This equation is in the form of Equation 3.1, as desired. This gives the following solution for $T(E_n, E_p)$:

$$T(E_n, E_p) = \sum_c \lambda_{c,i_c} b_{c,i_c}(E_p) \left[U_{c,i_c}(E_n, t_{irr}) e^{-d_{c,i_c} t_{dec}} + \sum_{j=1}^{i_c-1} U_{c,j}(E_n, t_{irr}) B_{c,i_c,j}(t_{dec}) \right]. \tag{3.13}$$

In other words if $U_{c,i}(E_n, t_{irr})$ for $i \in [1, i_c]$ can be found that satisfy Equation 3.10, an expression for $T(E_n, E_p)$ can be found in the form of Equation 3.13, for use with the MS-CADIS adjoint neutron source. The next section explores when suitable $U_{c,i}(E_n, t_{irr})$ can be found.

3.2 Relating Neutron Flux and Nuclide Concentration

In Section 3.1 it was shown that a solution for $T(E_n, E_p)$ can be found provided that Equation 3.10 can be used to describe the concentration of nuclides after irradiation. In this section, it is first shown that a $U_{c,i}(E_n, t_{irr})$ that satisfies Equation 3.10 cannot be found in the case of arbitrary transmutation chains and irradiation scenarios. Transmutation approximations are then described in order to find a suitable $U_{c,i}(E_n, t_{irr})$, which ultimately can be used to obtain a solution for $T(E_n, E_p)$ in Equation 3.1 for use with the MS-CADIS method.

3.2.1 General Case

The quantity $U_{c,i}(E_n, t_{irr})$ relates neutron flux to $N_{c,i}(t_{irr})$. The Bateman equation can be used to obtain such a relationship by using P and d terms that represent production and destruction during the irradiation interval from time 0 to time t_{irr}. Due to the modeling of each chain individually, a simplification can be made. For a given transmutation chain only the first nuclide, $N_{c,1}$ is present at the beginning of irradiation. In other words, the initial concentrations of all subsequent nuclides in the chain are zero. If any $N_{c,i}$ for $i > 1$ is present at the beginning of irradiation it is modeled as a separate chain. This assumption allows for the Bateman equation to be simplified to the following expression,[1] with the chain notation (c) suppressed:

$$N_i(t_{irr}) = \begin{cases} N_i(0)e^{-d_i t_{irr}}, \quad i = 1, & \text{(3.14a)} \\ N_1(0) \sum_{k=1}^{i-1} \left[\frac{P_{k+1}\left(e^{-d_k t_{irr}} - e^{-d_i t_{irr}}\right)}{d_i - d_k} \prod_{\substack{l=1, \\ l \neq k}}^{i-1} \frac{P_{l+1}}{d_l - d_k} \right], \quad i > 1. & \text{(3.14b)} \end{cases}$$

In this equation, destruction terms (d), which may be flux dependent, appear in exponentials. Because this equation gives an exponential relationship between nuclide concentration and neutron flux, it is clear that this relationship cannot be cast into the form of Equation 3.10. This means that transmutation approximations are required in order to proceed.

3.2.2 Transmutation Approximations

In order to obtain an expression in the form of Equation 3.10 (ultimately to find an expression for T for the MS-CADIS adjoint neutron source) it is first assumed that the parent nuclide $(N_{c,1})$ is stable. If $N_{c,1}$ is stable then no $N_{c,1}$ is transmuted during the decay period. In this case, $N_{c,1}$ does not contribute to the production of N_{c,i_c} during the decay period, which

[1] This formulation does not account for unrolled transmutation loops. Treatment for this special case is found elsewhere [27].

indicates that $B_{c,i_c,1} = 0$. As a result, the expression for $T(E_n, E_p)$ in Equation 3.13 no longer requires $U_{c,i}(E_n, t_{irr})$ for $i = 1$, only for $i \in [2, i_c]$. Therefore, finding an expression for $U_{c,i}(E_n, t_{irr})$ can proceed using Equation 3.14b.

The exponential terms in Equation 3.14b can be simplified using the following Taylor expansion:

$$e^{-d \cdot t_{irr}} = \sum_{z=0}^{\infty} \frac{(-d \cdot t_{irr})^z}{z!} \approx \sum_{z=0}^{Z} \frac{(-d \cdot t_{irr})^z}{z!}, \tag{3.15}$$

where Z is a parameter that defines truncation. For values of $d \cdot t_{irr} < 1$ the magnitude of the terms in the Taylor expansion decrease monotonically:

$$|1| > |-d \cdot t_{irr}| > \left|\frac{(d \cdot t_{irr})^2}{2}\right| > \left|-O((d \cdot t_{irr})^3)\right|. \tag{3.16}$$

The smaller the value of $d \cdot t_{irr}$, the faster the terms decrease in magnitude. A small $d \cdot t_{irr}$ occurs when the irradiation time is short and the destruction rate is small, which has the physical interpretation of low burnup. This means that the lower the burnup, the fewer terms are required to accurately represent $e^{-d \cdot t_{irr}}$, and therefore a smaller Z can be use for truncation. Applying the Taylor expansion in Equation 3.15 to Equation 3.14b yields:

$$N_i(t_{irr}) = N_1(0) \sum_{k=1}^{i-1} \left[\frac{P_{k+1} \left(\sum_{z=0}^{Z} \frac{(-t_{irr})^z}{z!} (d_k^z - d_i^z) \right)}{d_i - d_k} \prod_{\substack{l=1, \\ l \neq k}}^{i-1} \frac{P_{l+1}}{d_l - d_k} \right], \quad i > 1. \tag{3.17}$$

The criteria for truncating the Taylor expansion in Equation 3.17 is that the Z term is much greater in magnitude than the $Z + 1$ term. As seen in Equation 3.17, this must be true for all $k \in [1, i - 1]$. This can be expressed as:

$$\left|(d_k^Z - d_i^Z)\frac{(-t_{irr})^Z}{Z!}\right| \gg \left|(d_k^{Z+1} - d_i^{Z+1})\frac{(-t_{irr})^{Z+1}}{(Z+1)!}\right| \text{ for } k \in [1, i-1],\ i > 1, \tag{3.18}$$

This criterion is met when t_{irr} is small relative to the destruction rates, which has the physical interpretation of low burnup. By truncating the Taylor expansion in Equation 3.17 with $Z = i-1$ an expression can be found in the form of Equation 3.10. When $Z = i-1$, Equation 3.17 is reduced to:

$$N_i(t_{irr}) = N_1(0)\frac{t_{irr}{}^{i-1}}{(i-1)!}\prod_{j=2}^{i} P_j, \quad i > 1. \tag{3.19}$$

This is shown in Appendix A for $i \in [2, 5]$. This truncation requires that the following condition is met, which is found by setting $Z = i - 1$ in Equation 3.18:

$$\left|(d_k^{i-1} - d_i^{i-1})\frac{(-t_{irr})^{i-1}}{(i-1)!}\right| \gg \left|(d_k^i - d_i^i)\frac{(-t_{irr})^i}{i!}\right| \text{ for } k \in [1, i-1],\ i > 1. \tag{3.20}$$

In order for Equation 3.19 to satisfy Equation 3.10 only one of the production rates (P_j) may have a neutron flux dependence. Since N_1 was assumed to be stable, P_2 must be flux dependent (otherwise no transmutation occurs). If P_2 takes the form:

$$P_2 = \int_{E_n} \sigma_{1\to2}(E_n)\phi_n(E_n)\mathrm{d}\,E_n, \tag{3.21}$$

then Equation 3.19 becomes

$$N_i(t_{irr}) = N_1(0)\frac{t_{irr}{}^{i-1}}{(i-1)!}\prod_{j=3}^{i} P_j \int_{E_n} \sigma_{1\to2}(E_n)\phi_n(E_n)\mathrm{d}\,E_n, \quad i > 1. \tag{3.22}$$

This equation is now in the form of Equation 3.10. By observation, $U_i(E_n, t_{irr})$ is found to

be:

$$U_i(E_n, t_{irr}) = N_1(0)\sigma_{1\to 2}(E_n)\frac{{t_{irr}}^{i-1}}{(i-1)!}\prod_{j=3}^{i} P_j, \quad i > 1. \tag{3.23}$$

When the criteria in Equation 3.20 are not met, the Taylor expansion cannot be truncated after the $Z = i-1$ term. This means that additional terms are required to accurately capture the behavior of the exponentials. If an additional term in included (i.e., truncation with $Z = i$) Equation 3.17 is reduced to:

$$N_i(t_{irr}) = N_1(0)\frac{{t_{irr}}^{i-1}}{i!}\Big(i - t_{irr}\sum_{j=1}^{i} d_j\Big)\prod_{k=2}^{i} P_k, \quad i > 1. \tag{3.24}$$

This is shown in Appendix A for $i \in [2, 5]$. This expression cannot be cast into the form of Equation 3.10 because the product of all of the production rates is multiplied by each destruction rate. For a given chain, if P_k is flux-dependent, d_{k-1} must also be flux-dependent. This yields an expression for $N_i(t)$ that contains product(s) of flux-dependent terms, which is inconsistent with Equation 3.10. For example, in the case where $i = 2$, Equation 3.24 becomes:

$$N_2(t) = N_1(0)P_2 t_{irr} - N_1(0)P_2\frac{{t_{irr}}^2}{2}d_1 - N_1(0)P_2\frac{{t_{irr}}^2}{2}d_2 \tag{3.25}$$

If N_1 is stable and P_2 is in the form of Equation 3.21 then d_1 may equal P_2 (or P_2 plus a decay term). This yields the expression:

$$\begin{aligned} N_2(t) =& N_1(0)\Big(t_{irr} - \frac{{t_{irr}}^2}{2}d_2\Big)\int_{E_n}\sigma_{1\to 2}(E_n)\phi_n(E_n)\mathrm{d}\,E_n \\ &- N_1(0)\frac{{t_{irr}}^2}{2}\left(\int_{E_n}\sigma_{1\to 2}(E_n)\phi_n(E_n)\mathrm{d}\,E_n\right)^2. \end{aligned} \tag{3.26}$$

In this expression N_2 and $\phi_n(E_n)$ have a quadratic relation that cannot be cast into the

form of Equation 3.10.

3.2.3 SNILB Criteria and SNILB Solution

In Section 3.1 it was shown that a solution for $T(E_n, E_p)$ can be found in the case where $U_{c,i}(E_n, t_{irr})$ can be found that satisfy Equation 3.10. In Section 3.2.2 an expression for $U_{c,i}(E_n, t_{irr})$ for $i \in [2, i_c]$ was found, valid under a certain set of criteria. These criteria are summarized in Equation 3.27. Equation 3.27a states that the low burnup criteria for nuclide i found in Equation 3.20 must be met for nuclides $i \in [2, i_c]$. Equations 3.27b and 3.27c denote that the nuclide i_c must be produced by a transmutation pathway that contains a single neutron interaction: specifically the interaction that converts N_1 to N_2. These three equations in aggregate are referred to as the Single Neutron Interaction and Low Burnup (SNILB) criteria.

$$\left|(d_k^{i-1} - d_i^{i-1})\frac{(-t_{irr})^{i-1}}{(i-1)!}\right| \gg \left|(d_k^i - d_i^i)\frac{(-t_{irr})^i}{i!}\right| \text{ for } i \in [2, i_c],\ k \in [1, i-1], \tag{3.27a}$$

$$P_2 = \int_{E_n} \sigma_{1\to 2}(E_n)\phi_n(E_n)\,dE_n \tag{3.27b}$$

$$P_j \neq P_j(\phi_n(E_n)) \quad \text{for } j \in [3, i_c] \tag{3.27c}$$

Provided that these criteria are met, $U_{c,i}(E_n, t_{irr})$ for $i \in [2, i_c]$ from Equation 3.23 can be substituted in Equation 3.13 to form the following solution for $T(E_n, E_p)$, referred to as the SNILB solution for $T(E_n, E_p)$:

$$\mathsf{T}(\mathsf{E_n},\mathsf{E_p}) = \sum_{\mathsf{c}} \lambda_{\mathsf{c},\mathsf{i_c}}\, \mathsf{b}_{\mathsf{c},\mathsf{i_c}}(\mathsf{E_p})\mathsf{N}_{\mathsf{c},1}(0)\left[\left[\sigma_{\mathsf{c},1\to2}(\mathsf{E_n})\frac{\mathsf{t_{irr}}^{\,\mathsf{i_c}-1}}{(\mathsf{i_c}-1)!}\prod_{\mathsf{j}=3}^{\mathsf{i_c}}\mathsf{P}_{\mathsf{c},\mathsf{j}}\right]e^{-\mathsf{d}_{\mathsf{c},\mathsf{i_c}}\mathsf{t}_{\mathrm{dec}}} + \sum_{\mathsf{j}=2}^{\mathsf{i_c}-1}\left[\sigma_{\mathsf{c},1\to2}(\mathsf{E_n})\frac{\mathsf{t_{irr}}^{\,\mathsf{j}-1}}{(\mathsf{j}-1)!}\prod_{\mathsf{k}=3}^{\mathsf{j}}\mathsf{P}_{\mathsf{c},\mathsf{k}}\right]\mathsf{B}_{\mathsf{c},\mathsf{i_c},\mathsf{j}}(\mathsf{t}_{\mathrm{dec}})\right] \tag{3.28}$$

Recalling that $\mathsf{B}_{\mathsf{c},\mathsf{i_c},1} = 0$ (because N_1 is assumed to be stable), note that the summation over $\mathsf{B}_{\mathsf{c},\mathsf{i_c},\mathsf{j}}$ in this equation starts at $\mathsf{j} = 2$. The SNILB solution for $\mathsf{T}(\mathsf{E_n},\mathsf{E_p})$ is only dependent on the material at $\vec{\mathsf{r}}$. Therefore $\mathsf{T}(\vec{\mathsf{r}},\mathsf{E_n},\mathsf{E_p})$ is resolved by obtaining $\mathsf{T}(\mathsf{E_n},\mathsf{E_p})$ for each material in the problem and mapping this information to $\vec{\mathsf{r}}$:

$$\mathsf{T}(\vec{\mathsf{r}},\mathsf{E_n},\mathsf{E_p}) = \mathsf{T}(\mathsf{E_n},\mathsf{E_p}) \text{ for material at } \vec{\mathsf{r}}. \tag{3.29}$$

The $\mathsf{T}(\vec{\mathsf{r}},\mathsf{E_n},\mathsf{E_p})$ provided by Equations 3.28 and 3.29 can be substituted into Equation 2.36 to obtain the SNILB solution for the MS-CADIS adjoint neutron source.

3.3 Evaluating the SNILB Criteria

The validity of the SNILB solution for the MS-CADIS adjoint neutron source is contingent on the SNILB criteria being met. In principle, the SNILB criteria given in Equation 3.27 could be independently evaluated for every transmutation chain in a given material or problem. However, since the MS-CADIS adjoint neutron source is ultimately used for the purpose of MC VR, minor deviations from the SNILB criteria being met may still result in useful MC VR parameters. This motivates the development of a method for assessing the extent to which the SNILB criteria are met. Here, a heuristic method is proposed. As demonstrated in

Section 3.2.3, if the SNILB criteria are met a $T(E_n, E_p)$ can be found that satisfies Equation 2.33. Casting Equation 2.33 into a discretized form, for neutron energy group g, photon energy group h, within discrete volume ν yields:

$$q_{\nu,p,h} = \sum_{g} T_{\nu,g,h}\ \phi_{\nu,n,g}, \tag{3.30}$$

This implies that when the SNILB criteria are met the photon emission density in photon energy group h resulting from the irradiation of material with some flux ϕ_n, denoted $q_{p,h}(\phi_n)$, can be expressed as the summation of contributions of irradiations from each constituent neutron energy group (volume notation suppressed):

$$q_{p,h}(\phi_n) = \sum_{g} q_{p,h}(\phi_{n,g}). \tag{3.31}$$

This expression states that the superposition of the photon emission densities resulting from irradiations of neutrons in single energy groups is equivalent the photon emission density resulting from an irradiation with all neutron energy groups simultaneously. This important relationship will be referred to as the "superposition property". In situations where the SNILB criteria are violated, this superposition relationship will not be true. The extent to which the SNILB criteria are met for photon energy group h can therefore be quantified by η_h:

$$\eta_h = \frac{\sum_{g} q_{p,h}(\phi_{n,g})}{q_{p,h}(\phi_n)}. \tag{3.32}$$

When the SNILB criteria are met, $\eta_h = 1$. Values of $\eta_h < 1$ or $\eta_h > 1$ indicate either that photons in group h are being produced via multiple-neutron-interaction pathways or the burnup criteria are not being met.

If $\eta_h > 1$, the superposition property in Equation 3.31 overestimates the photon emission density and if $\eta_h < 1$ the photon emission density is underestimated. The quantity η_h is dependent on nuclide/material, neutron spectrum, irradiation and decay scenario, and also

h. In order to draw conclusions about the extent to which the SNILB criteria are met it is convenient to collapse the photon energy dimension, noting that no photon energy group is more or less likely to have an η_h far from 1. Ideally, this collapsing would be done by taking into account the importance of each photon energy group to the SDR, I_h:

$$\eta_I = \frac{\sum_g \sum_h q_{p,h}(\phi_{n,g}) I_h}{\sum_h q_{p,h}(\phi_n) I_h}. \tag{3.33}$$

Here, η_I accounts for the importance of different photon energy groups via weighing factors I_h. These weighting factors are application dependent. The true importance of photon energy groups is equivalent to the adjoint photon flux, which varies spatially and depends on the adjoint photon source. If I_h can be obtained that capture a characteristic adjoint photon flux, Equation 3.33 can be used to assess if the SNILB criteria are met for important energy groups, thereby providing a more useful metric for the expected efficacy of methods the rely on the SNILB solution for $T(\vec{r}, E_n, E_p)$.

Another approach is to assign all I_h to be equal to 1, so that all photon energy groups are weighted equally, regardless of how important they are to the SDR. This approach is preferable for assessing the extent to which the SNILB criteria are met in general, and when the photon importance is not known. This approach is equivalent to calculating η_h where there is only a single photon energy group. By setting all I_h to be equal to 1 the quantity, designated η, is obtained:

$$\begin{aligned} \eta &= \frac{\sum_g \sum_h q_{p,h}(\phi_{n,g})}{\sum_h q_{p,h,\phi_n}} \\ &= \frac{\sum_g q_p(\phi_{n,g})}{q_p(\phi_n)}. \end{aligned} \tag{3.34}$$

To calculate η or η_I an activation code can be used to perform irradiations using the neutron

flux ϕ_n, and each of the constituent single-energy-group neutron fluxes $\phi_{n,g}$ individually. This is done using a neutron spectrum of interest for an irradiation scenario of interest. The resulting photon emission densities are used to calculate η or η_I via Equations 3.34 and 3.33, respectively. By evaluating η or η_I for all neutron spectra and materials within a problem, the extent to which the SNILB criteria are met can be evaluated. If the SNILB criteria are acceptably met, the SNILB solution for the MS-CADIS adjoint neutron source will be effective in producing MC VR parameters for SDR neutron transport.

Chapter 4

GT-CADIS and SNILB-Violation Methods

In this chapter, a collection of methods are proposed for approximating T. These approximations of T are used to define the MS-CADIS adjoint neutron source to form implementations of the MS-CADIS method. The first method is Groupwise Transmutation (GT)-CADIS which provides a way of calculating T by performing a series of irradiations for the material and irradiation scenario of interest with single-energy-group neutron fluxes. The resulting T is equivalent to the SNILB solution for T when the SNILB criteria are met and provides one possible approximation otherwise. For cases when the SNILB criteria are not met, modifications to GT-CADIS method are proposed in order to improve the approximation of T. The "spectra" modification, GTS-CADIS, evaluates T using *a priori* spectral information. The "background" modification evaluates T with irradiations with multiple neutron energy groups simultaneously, providing a background spectrum for the calculation of T. The GTSB-CADIS method has the features of both GTS- and GTB-CADIS. These methods are described in this chapter and later demonstrated and assessed in Chapters 7 and 8.

4.1 GT-CADIS

Equations 3.28 and 3.29 provide a solution for $\mathsf{T}(\vec{r},\, \mathsf{E}_n,\, \mathsf{E}_p)$ that can be used in conjunction with the MS-CADIS adjoint neutron source (Equation 2.36) to generate optimal weight window and biased source distributions via the CADIS method. In practice, this adjoint neutron source must take the discrete form:

$$q^{+}_{\nu,n,g} = \sum_{h} \mathsf{T}_{\nu,\,g,\,h}\ \phi^{+}_{\nu,p,h}. \tag{4.1}$$

This is necessary because deterministic transport is used both to obtain $\phi^{+}_{\nu,p,h}$ and carry out transport with $q^{+}_{\nu,n,g}$. As a result, ν represents a mesh volume element of the mesh used to carry out deterministic transport. The GT-CADIS method provides a procedure for obtaining $T_{\nu,g,h}$.

If the SNILB criteria are met, then from Equation 3.30 it is apparent that

$$q_{p,h}(\phi_{n,g}) = T_{g,h}\ \phi_{n,g}, \tag{4.2}$$

for a particular material and irradiation scenario. The SNILB solution for $T_{g,h}$ can then be ascertained by solving for $T_{g,h}$:

$$T_{g,h} = \frac{q_{p,h}(\phi_{n,g})}{\phi_{n,g}} \tag{4.3}$$

The GT-CADIS method obtains $T_{g,h}$ by performing irradiations with an activation code to obtain $q_{p,h}(\phi_{n,g})$ for use in Equation 4.3. For a single-pulse irradiation scenario, each material in a problem is irradiated with a flux $\phi_{n,g}$, containing neutrons in energy group g (as illustrated in Figure 4.1). This irradiation is carried out using the t_{irr} and t_{dec} of interest. Since $T_{g,h}$ is not dependent on neutron flux when the SNILB criteria are met, the magnitude of $\phi_{n,g}$ is not paramount. The magnitude of $\phi_{n,g}$ should be large enough that important reaction channels are populated, but not so large that the SNILB criteria are violated due to high burnup. The resulting $q_{p,h}(\phi_{n,g})$ reported by the activation code for all h are used with Equation 4.3 to calculate $T_{g,h}$ for all h. This procedure is carried out for all materials and all g, meaning that the total number of irradiations required is the product of the number of materials and the number of neutron energy groups. Since $T_{g,h}$ is independent of neutron spectra (provided that the SNILB criteria are met), $T_{\nu,g,h}$ can be found by calculating $T_{g,h}$ for the material in ν:

$$T_{\nu,g,h} = T_{g,h} \quad \text{for material in } \nu. \tag{4.4}$$

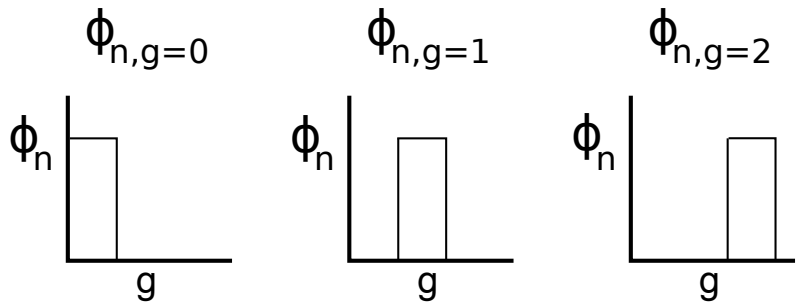

Figure 4.1: Example of the spectra used for GT-CADIS irradiations for a three neutron group case.

4.1.1 Practical Considerations

Applying GT-CADIS to realistic problems may require additional considerations for non-conformal meshes or complex irradiation scenarios. When meshes used for deterministic transport do not conform to geometry cells, each mesh volume element v may contain multiple materials. In this case, $T_{g,h}$ values for each material can be added by volume fraction. This additive property is demonstrated for two materials m_1 and m_2 with volume fractions of V_1 and V_2 within v in Equation 4.5.

$$\begin{aligned} q_{p,h,total} &= q_{p,h,m_1} + q_{p,h,m_2} \\ &= V_1 \sum_g T_{g,h,m_1}\, \phi_{n,g} + V_2 \sum_g T_{g,h,m_2}\, \phi_{n,g} \\ &= \sum_g \left(V_1 T_{g,h,m_1} + V_2 T_{g,h,m_2}\right) \phi_{n,g} \end{aligned} \tag{4.5}$$

All discussion to this point has considered only single-pulse irradiation and decay scenarios.

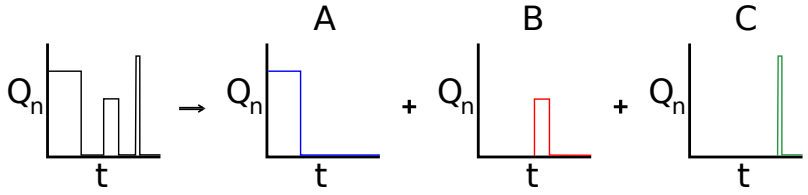

Figure 4.2: Splitting a multi-pulse irradiation scenario into individual pulses, with Q_n representing the neutron source intensity (n/s).

Realistic problems may involve irradiation scenarios with multiple pulses with different magnitudes, irradiation times, and decay times. When the SNILB criteria are met, $q_{p,h}$ from different pulses are independent because photon emission only results from single-neutron-interaction pathways. Figure 4.2 shows how a complex irradiation scenario can be thought of as superposition of three single-pulse irradiation scenarios: A, B, and C, with Q_n representing the neutron source intensity (n/s). The total photon source density in energy group h that results from irradiation with neutrons in group g with the scenario in Figure 4.2 is given by:

$$q_{p,g,h,total} = q_{p,g,h,A} + q_{p,g,h,B} + q_{p,g,h,C}. \tag{4.6}$$

The contribution from each pulse can be expressed in terms of the pulse-specific values for $T_{g,h}$ and neutron flux:

$$q_{p,g,h,total} = T_{g,h,A}\,\phi_{n,g,A} + T_{g,h,B}\,\phi_{n,g,B} + T_{g,h,C}\,\phi_{n,g,C}. \tag{4.7}$$

The ratio of neutron fluxes for any two pulses is equivalent to the ratio of the neutron source intensities. For example, $\phi_{n,g,A}$ and $\phi_{n,g,B}$ can be expressed in terms of $\phi_{n,g,C}$:

$$q_{p,g,h,total} = T_{g,h,A}\,\frac{Q_{n,A}}{Q_{n,C}}\phi_{n,g,C} + T_{g,h,B}\,\frac{Q_{n,B}}{Q_{n,C}}\phi_{n,g,C} + T_{g,h,C}\,\phi_{n,g,C}, \tag{4.8}$$

which simplifies to:

$$q_{p,g,h,total} = \left(T_{g,h,A}\,\frac{Q_{n,A}}{Q_{n,C}} + T_{g,h,B}\,\frac{Q_{n,B}}{Q_{n,C}} + T_{g,h,C}\right)\phi_{n,g,C}. \tag{4.9}$$

Dividing both sides of this equation by $\phi_{n,g,C}$ gives:

$$\frac{q_{p,g,h,total}}{\phi_{n,g,C}} = \left(T_{g,h,A}\,\frac{Q_{n,A}}{Q_{n,C}} + T_{g,h,B}\,\frac{Q_{n,B}}{Q_{n,C}} + T_{g,h,C}\right). \tag{4.10}$$

The quantity $q_{p,g,h,total}$ can be obtained by irradiating the material of interest with the full irradiation scenario (represented in the leftmost plot of Figure 4.2). Equation 4.10 states that

by dividing $q_{p,g,h,total}$ by the $\phi_{n,g,C}$ used for irradiation the result is equivalent to adding up the $T_{g,h}$ from individual pulses, weighted by the relative magnitude of the pulses. For irradiation scenarios containing many pulses, calculating $T_{g,h}$ for each pulse individually may be cumbersome. Instead, the $T_{g,h}$ for the total scenario can be calculated using the left hand side of Equation 4.10:

$$T_{g,h,total} = \frac{q_{p,g,h,total}}{\phi_{n,g,C}}. \tag{4.11}$$

The choice of $\phi_{n,g,C}$ is not unique — Equation 4.10 could have been defined in terms of $\phi_{n,g,A}$ or $\phi_{n,g,B}$. Furthermore, since $T_{g,h}$ is independent of flux when the SNILB are met, $T_{g,h,total}$ as calculated via Equation 4.11 is not sensitive to the magnitude of $\phi_{n,g,C}$. This strategy for calculating $T_{g,h}$ using a complex irradiation scenario is also applicable to the calculation of η and η_I described in Section 3.3.

4.1.2 GT-CADIS Procedure

In order to obtain neutron weight windows and a biased source via the GT-CADIS method, a deterministic adjoint photon transport step can be used to obtain $\phi^{+}_{p,h}$, using the dose rate tally(ies) of interest as the adjoint source. For each pure material in the problem, T is calculated by performing irradiations for each neutron energy group using the irradiation and decay scenario of interest. If mesh volume elements in the deterministic transport mesh cover multiple geometry cells with different materials, T values for each material are mixed by volume fraction to obtain the T of the mesh volume element. Then Equation 4.1 can be used as an adjoint neutron source and the standard CADIS method can be carried out in order to produce weight windows and a biased source for use with MC neutron transport. If the SNILB criteria are not met, this procedure can still be carried out, but the resulting VR parameters may not be effective. The expected efficacy can be predicted by calculating η or η_I for the materials, spectra, and irradiation scenario used in the problem.

4.1.3 Visualizing T

The quantity T can be easily visualized in the case of two-group neutron transport and activation. This will be useful in ensuing sections where situations that violate the SNILB criteria are considered. First consider a simple case where the SNILB criteria are met. In this case, photons are emitted after shutdown by N_2, which is produced via a single-step reaction with the stable nuclide N_1,

$$\mathsf{N}_1 \xrightarrow{\mathsf{n}} \mathsf{N}_2, \tag{4.12}$$

with the following production and destruction rates:

$$\mathsf{P}_2 = \sum_{\mathsf{g}} \sigma_{1\to 2,\mathsf{g}} \phi_{\mathsf{n},\mathsf{g}}, \tag{4.13}$$

$$\mathsf{d}_1 = \mathsf{P}_2, \tag{4.14}$$

$$\mathsf{d}_2 = \lambda_2. \tag{4.15}$$

For a sufficiently low irradiation time, such that the SNILB criteria are met, the photon emission density at the at time $\mathsf{t}_{\text{tot}} = \mathsf{t}_{\text{irr}} + \mathsf{t}_{\text{dec}}$ is given by:

$$\mathsf{q} = \lambda_2 \mathsf{b}_{2,\mathsf{h}} e^{-\lambda_2 \mathsf{t}_{\text{dec}}} \mathsf{N}_1(0) \mathsf{P}_2 \Big(\frac{e^{-\mathsf{d}_1 \mathsf{t}_{\text{irr}}} - e^{-\mathsf{d}_2 \mathsf{t}_{\text{irr}}}}{\mathsf{d}_2 - \mathsf{d}_1} \Big) \tag{4.16}$$

Using the parameters in Table 4.1, this equation is plotted as a function the two-group neutron fluxes $\phi_{\mathsf{g}=0}$ and $\phi_{\mathsf{g}=1}$ as seen in Figure 4.3. Using the GT-CADIS method, irradiations are performed with single-energy-group fluxes, represented by the red points. The slope of the green lines represent the values of $\mathsf{T}_{\mathsf{g}=0,\mathsf{h}}$ and $\mathsf{T}_{\mathsf{g}=1,\mathsf{h}}$. Since the plot is approximately planar the slope with respect to $\phi_{\mathsf{g}=0}$ and $\phi_{\mathsf{g}=1}$ is constant. This means that flux magnitudes used for these irradiations (e.g., 10^{13} cm^{-2}s^{-1}) are inconsequential, provided that they are low enough that there is not significant burnup. Due to the planar shape of the plot, it is also

Table 4.1: Parameters used in Figure 4.3.

parameter	value
$N_1(0)$	$1 \cdot 10^{22}$ cm^{-3}
t_{irr}	1 d
t_{dec}	30 d
$\sigma_{1\to2,g=0}$	100 b
$\sigma_{1\to2,g=1}$	200 b
$t_{1/2,1}$	∞ (stable)
$t_{1/2,2}$	1 y
$b_{2,h}$	1

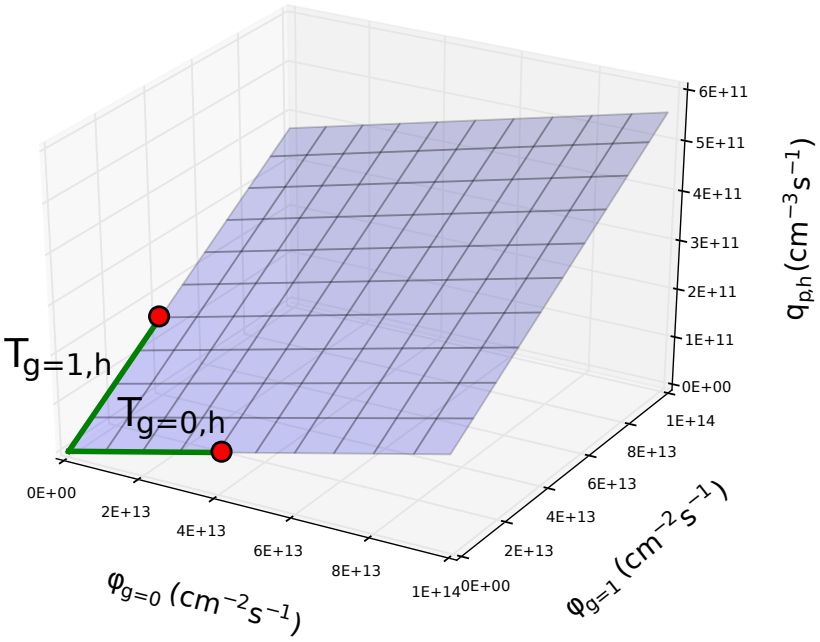

Figure 4.3: Photon emission density at time t_{tot}, given by Equation 4.16 with parameters from Table 4.1. Red points represent irradiations used to calculate $T_{g,h}$ values, which are represented by the slopes of the green lines.

apparent that the superposition property in Equation 3.31 is valid.

4.1.4 SNILB Violations Effect on GT-CADIS Estimates of T

If the SNILB criteria are not met, Equation 4.2 is not valid and the GT-CADIS method is not guaranteed to produce useful VR parameters. The SNILB criteria can be violated by irradiation scenarios that result in either high burnup, multiple neutron interactions yielding

important photons, or some combination of the two. Different violation mechanisms are expected to have different effects on $T_{g,h}$ values estimated by GT-CADIS, as discussed in this section.

4.1.4.1 High Burnup

Equation 3.27a provides a mathematical description of the low burnup portion of the SNILB criteria. One way this criterion can be violated is if the fluence is large enough that the concentration of important starting nuclides (i.e., N_1 for any linear decay chain) decreases significantly and cannot be assumed to be constant. The single-step reaction given in Equation 4.12 and the parameters in Table 4.2 results in such a situation. The parameters in Table 4.2 are identical to those in Table 4.1 except t_{irr} has been changed to 7 years.

A plot of $q_{p,h}$ as a function of the two-group neutron fluxes $\phi_{g=0}$ and $\phi_{g=1}$ for this scenario is shown in Figure 4.4. This figure shows photon emission density increases as a function of flux for low flux and decreases as a function of flux at high flux, as the concentration of N_1 depletes. Using the GT-CADIS method, calculated $T_{g,h}$ values would vary with the choice of $\phi_{g=0}$ and $\phi_{g=1}$, for choices past the linear region at low flux (i.e., choices greater than $1{\cdot}10^{13}$ $cm^{-3}s^{-1}$).

Since the plane has a negative concavity, $T_{g,h}$ will tend to be overestimated by the GT-CADIS method. For example, consider the case where the actual neutron spectrum experienced by a volume is $\phi_0 = 6 \cdot 10^{13}$ $cm^{-2}s^{-1}$, $\phi_1 = 6 \cdot 10^{13}$ $cm^{-2}s^{-1}$: the ϕ_0 and ϕ_1 coordinates of the yellow point in Figure 4.4. If $q_{p,h}$ was calculated via Equation 3.30 using the $T_{g,h}$ values calculated by the slopes in green, it is clear that the resulting $q_{p,h}$ will be much greater in magnitude than the $q_{p,h}$ represented by the yellow point. This could be predicted prior to performing the GT-CADIS method by calculating η_h via Equation 3.32, which would be found to be greater than one. Ultimately, this effect will manifest itself in weight windows and biased sources that overestimate the importance of regions that are subjected to significant burnup.

Table 4.2: Parameters used in Figure 4.4.

parameter	values
$N_1(0)$	$1 \cdot 10^{22}$ cm^{-3}
t_{irr}	7 y
t_{dec}	30 d
$\sigma_{1\to2,g=0}$	100 b
$\sigma_{1\to2,g=1}$	200 b
$t_{\frac{1}{2},1}$	∞ (stable)
$t_{\frac{1}{2},2}$	1 y
$b_{2,h}$	1

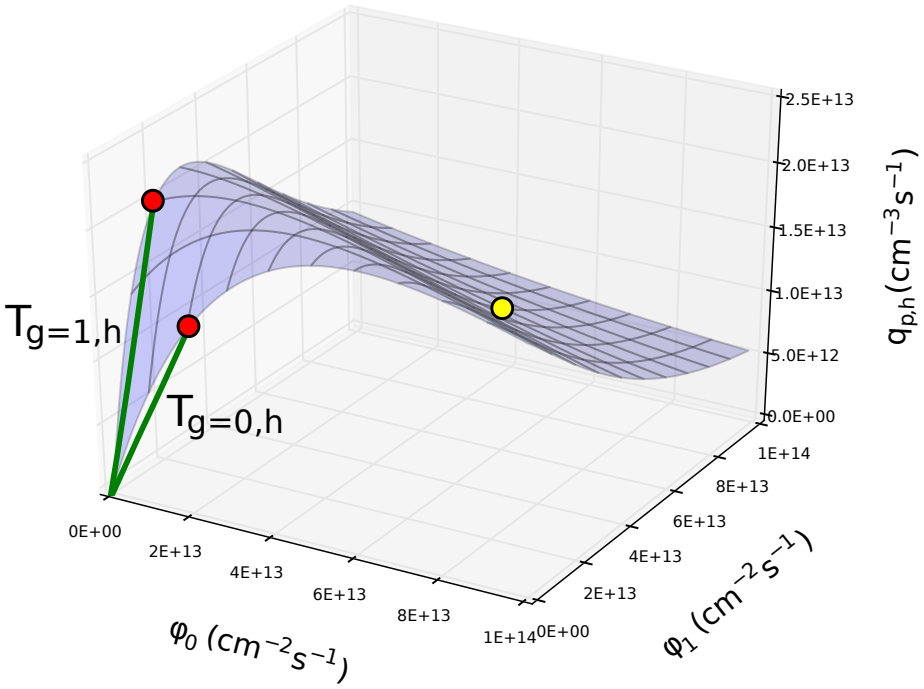

Figure 4.4: Photon emission density at time t_{tot}, given by Equation 4.16 with parameters from Table 4.2. Red points represent irradiations used to calculate $T_{g,h}$ values, which are represented by the slopes of the green lines. The yellow point represents the photon emission density for one possible known neutron spectrum.

4.1.4.2 Multiple Neutron Interactions

The SNILB criteria are also violated when photons are produced by pathways that involve multiple neutron interactions, which may affect the performance of the GT-CADIS method. Consider a reaction pathway given by

$$N_1 \xrightarrow{n} N_2 \xrightarrow{n} N_3, \tag{4.17}$$

where photons of interest are only emitted by N_3. The analytic solution for the photon emission density from N_3 in photon group h with an irradiation of time t_{irr} and a decay of time t_{dec} is found by combining Equations 3.14b and 3.7:

$$q_{p,h} = \lambda_3 b_{3,h} e^{-\lambda_3 t_{dec}} \frac{N_{1_0} P_2 P_3}{d_2 - d_1} \left(\frac{e^{-d_1 t_{irr}} - e^{-d_3 t_{irr}}}{d_3 - d_1} - \frac{e^{-d_2 t_{irr}} - e^{-d_3 t_{irr}}}{d_3 - d_2} \right). \tag{4.18}$$

where

$$\begin{aligned} P_2 &= \sigma_{1\to2,g=0}\phi_0 + \sigma_{1\to2,g=1}\phi_1 \\ P_3 &= \sigma_{2\to3,g=0}\phi_0 + \sigma_{2\to3,g=1}\phi_1 \\ d_1 &= P_2 \\ d_2 &= P_3 + \lambda_2 \\ d_3 &= \lambda_3 \end{aligned} \tag{4.19}$$

A plot of this equation using parameters from Table 4.3 is shown in Figure 4.5. Cross sections in Table 4.3 were chosen such that the production of N_2 is dominated by interactions with neutrons from group 0 and the production of N_3 is dominated by neutrons from group 1. In other words, the production rate of N_3 is expected to be much higher when both neutron groups are present. With the GT-CADIS method, single-energy-group irradiations are carried

out, ostensibly represented by the red points in Figure 4.5. Since the plane has a positive concavity, $T_{g,h}$ and therefore the importance of a region will tend to be underestimated by the GT-CADIS method: the opposite effect as described in the high burnup case in Section 4.1.4.1. For example, if the actual neutron spectrum is $\phi_0 = 6 \cdot 10^{13}$ cm^{-2}s^{-1}, $\phi_1 = 6 \cdot 10^{13}$ cm^{-2}s^{-1} (the ϕ_0 and ϕ_1 coordinates of the yellow point), the $q_{p,h}$ calculated via Equation 3.30 using the $T_{g,h}$ values calculated by the slopes in green, will be much smaller in magnitude that the $q_{p,h}$ represented by the yellow point. Again, this could be predicted by calculating η_h via Equation 3.32, which would be found to be less than one.

Table 4.3: Parameters used in Figure 4.5.

parameter	value
N_{1_0}	$1 \cdot 10^{22}$ cm^{-3}
t_{irr}	1 d
t_{dec}	30 d
$\sigma_{1\to2,g=0}$	500 b
$\sigma_{1\to2,g=1}$	50 b
$\sigma_{2\to3,g=0}$	1 b
$\sigma_{2\to3,g=1}$	150 b
$t_{1/2,1}$	∞ (stable)
$t_{1/2,2}$	1 y
$b_{3,h}$	20 d

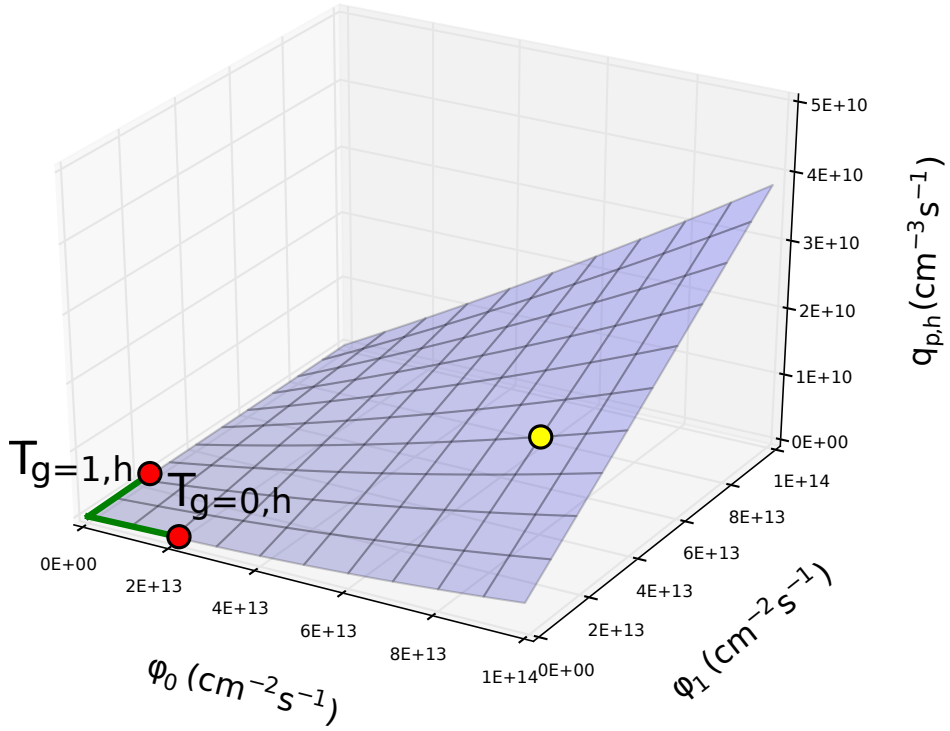

Figure 4.5: Photon emission density at time t_{tot} , given by Equation 4.18 with parameters from Table 4.3. Red points represent irradiations used to calculate $T_{g,h}$ values via GT-CADIS, which are represented by the slopes of the green lines. The yellow point represents the photon emission density for one possible known neutron spectrum.

4.2 SNILB-Violation Methods

In Section 4.1.3 it was shown that $q_{p,h}$ can be represented by a G-dimensional surface with G being the number of neutron energy groups. When the SNILB criteria are met, this surface is planar. In Section 4.1.4 it was shown that when the SNILB criteria are violated, the surface is no longer planar. The full shape of these nonlinear G-dimensional surfaces cannot be captured in using G $T_{g,h}$ values. In this case T can be chosen to somehow approximate the shape of the curve. These schemes, referred to as SNILB-Violation methods ideally would have the following three properties.

1. Shape: T should be chosen such that all $T_{g,h}$ values accurately represent that relative importance of neutron energy group g to the production of decay photons in energy group h.

2. Magnitude: T should be chosen such that the total magnitude of the photon emission density is correct. In other words, $q_{p,h}$ as calculated by Equation 3.30 is equivalent to the actual $q_{p,h}$.

3. Reduction to GT-CADIS: SNILB-violation methods should reduced down to the GT-CADIS method, thereby providing the SNILB solution for T, when the SNILB criteria are met.

As introduced in the beginning of Chapter 3, the linearization $f'(0)$ in Equation 3.5 can be used to define T. SNILB-violations methods are akin to defining T using $f'(a)$ where $a \neq 0$ (i.e., approximating the derivative around a nonzero flux) and/or accounting for nonzero $f(a)$, $f''(a)$, $f'''(a)$, etc., terms by modifying the $f'(a)$ term. Many schemes for generating T values using these strategies are possible.

In this section three SNILB-violation methods are proposed and the advantages and disadvantages of each are discussed. Like the GT-CADIS method, each one of these methods produces T and can then be used as an implementation of the MS-CADIS method. Though

these methods may be beneficial for both high-burnup and also multiple-neutron-interaction scenarios, multiple-neutron-interaction scenarios will be the primary focus. This is because multiple-neutron-interaction scenarios result in much more significant SNILB criteria violations as will be discussed in Chapter 6. In addition, in FES analysis the SDR is commonly desired far from the neutron source. In these cases , the adjoint photon flux will be low in the high-burnup regions near the source, mitigating the effects of poorly approximating T. The efficacy of the SNILB-violation methods introduced here is later tested in Chapter 8.

4.2.1 GTS-CADIS

The "spectra" modification to GT-CADIS, referred to as GTS-CADIS, uses *a priori* knowledge of neutron spectra to attempt to improve T. With this method, a deterministic forward neutron transport calculation is done prior to calculating T. A T is calculated for each volume element ν individually. For each ν, irradiations are conducted in a similar fashion to the GT-CADIS method. Instead of using a flat neutron spectrum as is done for the GT-CADIS method (i.e., Figure 4.1), the actual groupwise neutron fluxes within ν, $\phi_{n,\nu,g}$ are used, as seen in Figure 4.6. The intermediate quantities $\mathsf{T}'_{\nu,g,h}$ are then calculated by:

$$\mathsf{T}'_{\nu,g,h} = \frac{q_{p,h}(\phi_{n,\nu,g})}{\phi_{n,\nu,g}}. \tag{4.20}$$

An additional irradiation is performed using all neutron energy groups simultaneously (i.e $\phi_{n,\nu}$ in Figure 4.6). The $\mathsf{T}'_{\nu,g,h}$ values are then normalized such that total $q_{p,h}$ as calculated by Equation 3.30 is equivalent to the $q_{p,h}(\phi_{n,\nu})$ from this final irradiation. This is done using the formula:

$$\mathsf{T}_{\nu,g,h} = \mathsf{T}'_{\nu,g,h} \frac{q_{p,h}(\phi_{n,\nu})}{\sum_g \mathsf{T}'_{\nu,g,h}\,\phi_{n,\nu,g}}. \tag{4.21}$$

With $\mathsf{T}_{\nu,g,h}$ calculated for all ν, g, and h, the GTS-CADIS method proceeds in the same fashion as GT-CADIS.

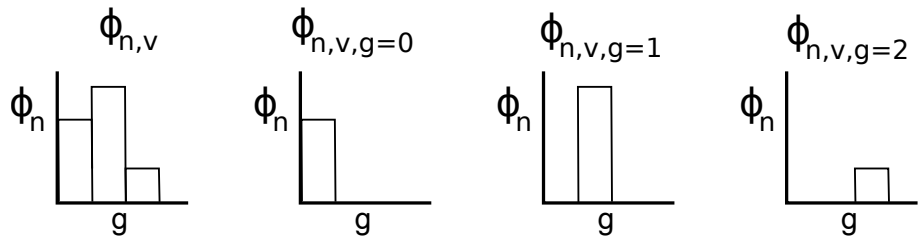

Figure 4.6: Example of spectra used for GTS-CADIS irradiations for a three neutron group case.

A graphical representation of the GTS-CADIS method is seen in Figure 4.7 for the multiple-neutron-interaction scenario described in Section 4.1.4.2. The red points represent irradiations conducted, with the red/yellow point representing an irradiation conducted with $\phi_{v,g}$. Upon normalization, the $T'_{v,g,h}$ values shown in this plot would be increased, but the ratio between them would remain the same.

GTS-CADIS offers an improvement over GT-CADIS for both high-burnup and multiple-neutron-interaction scenarios by ensuring that the magnitude of T is correct. However, since GTS-CADIS only uses single-energy-group irradiations like GT-CADIS, it is unlikely that shape of T will capture the behavior associated with multiple neutron interactions. When the SNILB criteria are met, $T'_{v,g,h}$ and $T_{v,g,h}$ values will be equal and will be equivalent to the SNILB solution.

A major disadvantage of the GTS-CADIS method is it requires a deterministic estimate of the forward neutron flux and subsequently the calculation of T for each v, which is computationally expensive. One possible modification to this method is to calculate $T'_{g,h}$ values for each material with a flat neutron spectrum (like GT-CADIS: without the actual spectrum in v), then normalize these $T'_{g,h}$ values within each v by conducting irradiations with $q_{p,h}(\phi_{n,v})$ and applying Equation 4.21. This simplification reduces the number of irradiations required per v from $G+1$ to 1 (where G is the number of neutron energy groups). This simplification will only be useful if $T'_{g,h}$ values calculated with a flat spectrum are similar to $T'_{v,g,h}$ values calculated with the actual spectrum in v. This is more likely to be the case for multiple-neutron-interaction pathways then for high-burnup pathways.

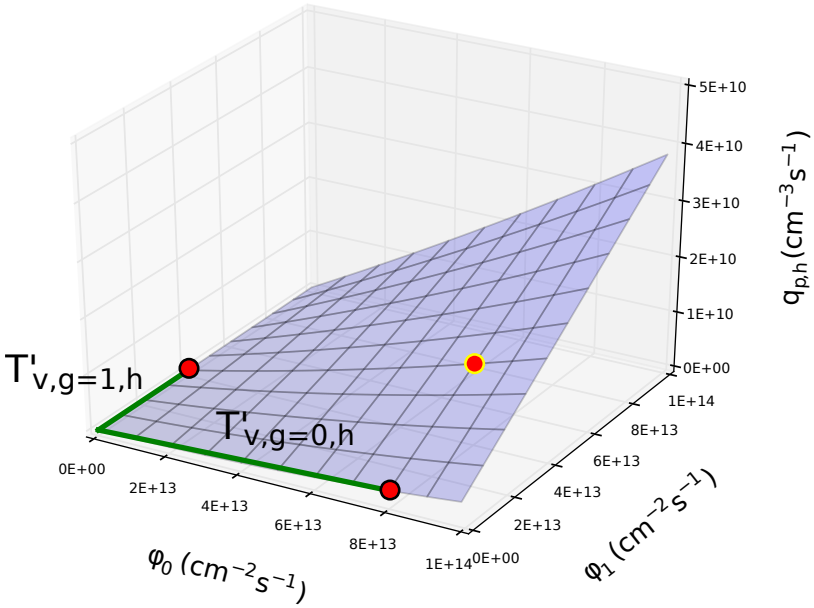

Figure 4.7: Graphical representation of the GTS-CADIS method for the multiple-neutron-interaction scenario described in Section 4.1.4.2. The red points represent irradiations conducted, with the red/yellow point representing an irradiation conducted with $\phi_{v,g}$.

4.2.2 GTB-CADIS

The "background" modification to the GT-CADIS method, referred to as GTB-CADIS, attempts to improve upon the GT-CADIS method by performing irradiations with multiple energy groups simultaneously. This should better capture the effects of multiple neutron interactions which may occur at different neutron energies. With this method, a "background" neutron spectrum $\phi_{n,b}$ is defined with uniform intensity across all energy groups. The magnitude of the background spectrum should be similar to that experienced in important regions within the problem. For each neutron energy group, a spectrum is defined that consists of the background spectrum, with a single neutron energy group perturbed by some multiplicative factor p. This factor may be any nonnegative value not equal to 1. For example, $p = 1.1$ would result in a 10% increase in the magnitude of the flux in the perturbed energy group, whereas $p = 0.9$ would result in a 10% decrease. An example of these spectra is shown in Figure 4.8.

Irradiations are then performed using the background spectrum and each perturbed spectra.

Values of $T_{g,h}$ are then calculated using the following formula, in which the contribution of the background spectrum to the photon emission density is subtracted from photon emission density resulting from the perturbed neutron spectra:

$$T_{g,h} = \frac{q_{p,h}(\phi_{n,b} + (p-1)\phi_{n,b,g}) - q_{p,h}(\phi_{n,b})}{(p-1)\phi_{n,b,g}}. \tag{4.22}$$

In this formulation, $T_{g,h}$ is akin to the partial derivative of $q_{p,h}$ with respect to $\phi_{n,b,g}$ around the point $\phi_{n,b}$, estimated with a linear perturbation. Likewise, Equation 4.22 is in the form

$$\frac{\partial q_{p,h}}{\partial \phi_{n,b,g}}\Big|_{\phi_{n,b}} \approx \frac{q_{p,h}(\phi_{n,b} + \Delta\phi_{n,b,g}) - q_{p,h}(\phi_{n,b})}{\Delta\phi_{n,b,g}}. \tag{4.23}$$

where the step size $\Delta\phi_{n,b,g}$ is equal to $(p-1)\phi_{n,b,g}$.

A graphical representation of the GTB-CADIS method is shown in Figure 4.9 for the multiple-neutron-interaction scenario described in Section 4.1.4.2. In both the GT- and GTS-CADIS methods, the shape of T is determined by the slopes of the surface around the origin. With GTB-CADIS, the shape of T is determined by the slopes of the surface around the $\phi_{n,b}$ point. The slopes are much steeper around the $\phi_{n,b}$ point because neutron flux in all energy groups allows for multiple neutron interactions that occur at different energy groups to be captured. This may improve the shape of T. However, the magnitude of T may not be correct. For example, the yellow point in Figure 4.9 represents some known neutron spectrum. Using GTB-CADIS it is not guaranteed that calculated $T_{g,h}$ values give the correct $q_{p,h}$ via Equation 3.30, for any arbitrary location of the yellow point.

One advantage of the GTB-CADIS method is that unlike GTS-CADIS, detailed *a priori* knowledge of the neutron spectrum for each ν is not required. However, some knowledge of the spectra may be necessary in order to choose the magnitude of the groupwise fluxes in $\phi_{n,b}$. Like GT-CADIS, T must be calculated only for each pure material in the problem, and these values can be mixed by volume fraction to obtain T in each ν. Furthermore, when

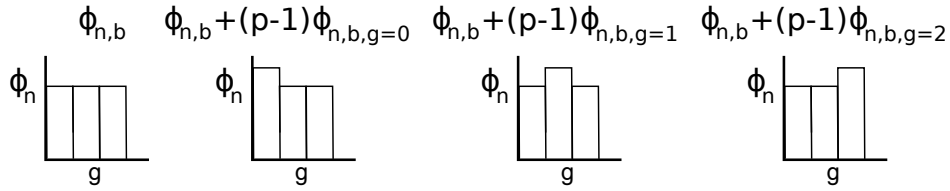

Figure 4.8: Example of spectra used for GTB-CADIS irradiations for a three neutron group case. Here, p is 1.25.

the SNILB criteria are met GTB-CADIS gives the same results as GT-CADIS. When the SNILB criteria met, the $q_{p,h}$ surface is planar. Since the slopes are the same at every point, it does not matter what point is chosen to calculate the slope. The principle disadvantage of the GTB-CADIS method is that it does not guarantee that $T_{g,h}$ values are positive for all g and h. This means GTB-CADIS is ill-suited for high-burnup scenarios like that described in Section 4.1.4.1, where the slope of $q_{p,h}$ is negative is some regions, as seen in Figure 4.4. GTB-CADIS may produce negative $T_{g,h}$ values in multiple-neutron-interaction scenarios as well, for neutron energy groups that are not important to dominant photon production pathways but still contribute the to destruction rates of important nuclides. It is suggested that any $T_{g,h}$ produced by GTB-CADIS that are found to be negative should be replaced by $T_{g,h}$ values calculated using the standard GT-CADIS method.

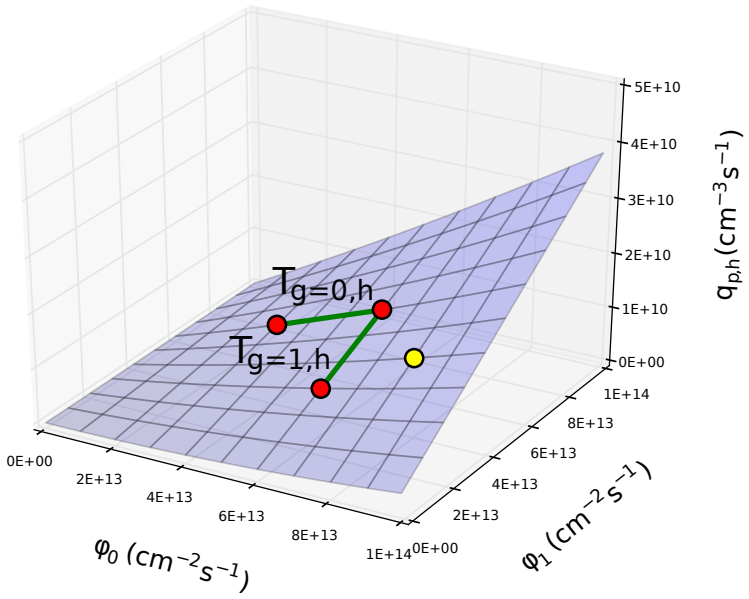

Figure 4.9: Graphical representation of the GTB-CADIS method for the multiple-neutron-interaction scenario described in Section 4.1.4.2. The red points represent irradiations conducted, here with $p = 0.5$. The yellow point represents one possible known neutron spectrum.

4.2.3 GTSB-CADIS

The GTSB-CADIS method is a combination of the "spectra" and "background" modifications described in Sections 4.2.1 and 4.2.2 respectively. As with GTS-CADIS, a deterministic forward neutron transport calculation is first done. Then irradiations are conducted in similar fashion to GTB-CADIS method. Instead of using a flat background spectrum, the known neutron spectra for each ν, $\phi_{n,\nu}$ is used. Perturbations are applied for each energy group as is done with the GTB-CADIS method. An example of the neutron spectra used by the GTSB-CADIS method is shown in Figure 4.10. Once irradiations are done for each of these spectra, the intermediate quantities $T'_{\nu,g,h}$ are calculated:

$$T'_{\nu,g,h} = \frac{q_{p,h}(\phi_{n,\nu} + (p-1)\phi_{n,\nu,g}) - q_{p,h}(\phi_{n,\nu})}{(p-1)\phi_{n,\nu,g}}. \tag{4.24}$$

These values are then normalized in a similar fashion to the GTS-CADIS method:

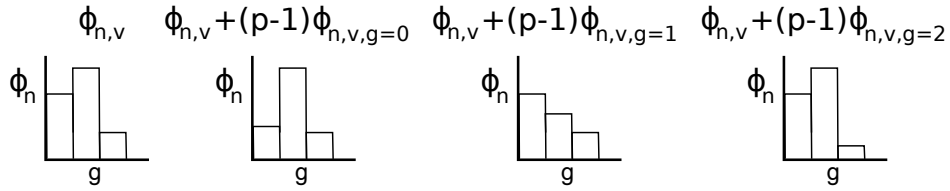

Figure 4.10: Example of spectra used for GTSB-CADIS irradiations for a three neutron group case. Here, p is 0.5.

$$T_{\nu,g,h} = T'_{\nu,g,h} \frac{q_{p,h}(\phi_{n,\nu})}{\sum_g T'_{\nu,g,h}\, \phi_{\nu,n,g}} \tag{4.25}$$

This process ensures that the magnitude of T is correct while capturing the behavior of multiple neutron interactions. When the SNILB criteria are met, T produced by GTSB-CADIS are equivalent to those produced by GT-CADIS, for the same reason stated in Section 4.2.2. Though this method combines the advantages of GTS- and GTB-CADIS into a single method, it also combines the disadvantages. Like GTS-CADIS, T must be calculated for each ν individually, which is likely to be computationally expensive. Like GTB-CADIS, $T_{g,h}$ values are not guaranteed to be nonnegative, which means that this method may not be suitable for high-burnup scenarios. If negative $T_{g,h}$ values are encountered, it is suggested that these individual values are recalculated with GTS-CADIS. A graphic representation of the GTSB-CADIS method for the multiple-neutron-interaction scenario described in Section 4.1.4.2 is shown in Figure 4.11.

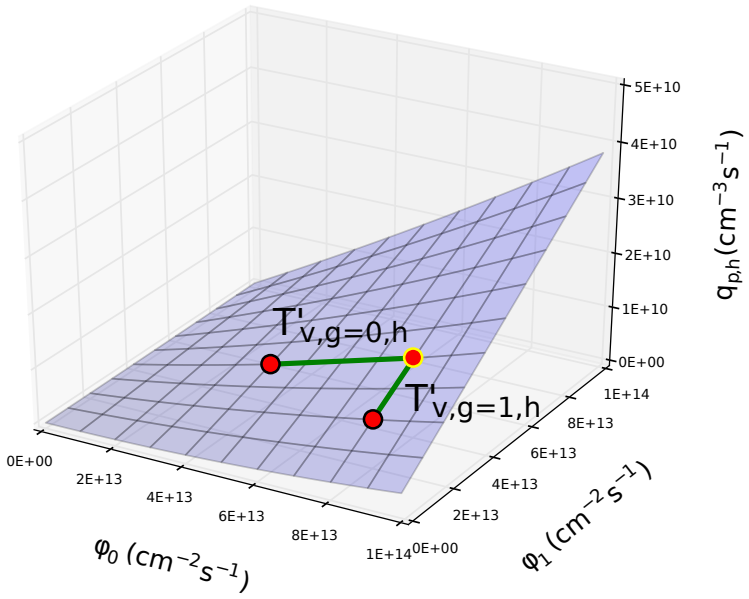

Figure 4.11: Graphical representation of the GTSB-CADIS method for the multiple-neutron-interaction scenario described in Section 4.1.4.2. The red points represent irradiations conducted, here with $p = 0.5$. The red/yellow point represents an irradiation conducted with $\phi_{v,g}$.

4.2.4 Summary of SNILB-Violation Methods

When the SNILB criteria are not met, the SNILB solution for T is not valid and variety of techniques can be used to ascertain T. The three techniques proposed in this section all have advantages and disadvantages that may limit their applicability or efficacy. These properties are summarized in Table 4.4.

Table 4.4: Advantages of GT-CADIS and SNILB-violation methods.

	method			
Advantage	GT	GTS	GTB	GTSB
T shape captures multiple neutron interactions			✓	✓
T magnitude correct		✓		✓
Equivalent to GT-CADIS when SNILB are met	✓	✓	✓	✓
T required only for pure materials	✓		✓	
$T_{g,h}$ guaranteed to be positive	✓	✓		

Chapter 5

Software Implementation

The numerical experiments conducted in this work have required the development and use of a significant collection of computational tools. An R2S workflow was required to calculate the SDR from MC neutron fluxes obtained using GT-CADIS or SNILB-violation methods. In order to obtain these VR parameters, deterministic adjoint flux distributions were required, in addition to T. Finally, mesh-based adjoint fluxes and an unbiased source must be converted to weight windows and a biased source using the CADIS method. In this chapter, the computational tools created to perform these operations are presented. Many components of this software have been written within the Python for Nuclear Engineering (PyNE) toolkit. PyNE is a trans-institutional, open-source project consisting of Python, C++, and Fortran code pertinent to nuclear engineering simulations and analysis [35].

5.1 R2S Workflow

The PyNE R2S workflow [5] was used in order to automatically calculate the SDR in this work. PyNE R2S is a Cartesian- and tetrahedral-mesh-based R2S workflow, that operates entirely on CAD geometry. PyNE R2S uses DAG-MCNP5 for both MC transport steps and the ALARA nuclear inventory analysis code. PyNE R2S has been validated with the Frascati Neutron Generator (FNG) ITER benchmark problem [36].

For this work, only Cartesian mesh was used. A neutron transport simulation is first done using DAG-MCNP5. Multigroup neutron fluxes are tallied using a standard MCNP5 mesh tally covering the geometry of interest for neutron activation. PyNE R2S then converts the resulting neutron fluxes, user-supplied irradiation scenario, and CAD geometry into the appropriate ALARA input files. Since an activation calculation must be done for each mesh

volume element, this process requires that the material composition is known within each mesh volume element. For Cartesian meshes, each mesh volume element may contain multiple geometry cells and therefore multiple materials. A ray-tracing technique is used to discretize the CAD geometry onto the mesh to obtain the volume fraction of each geometry cell with each mesh volume element [37]. This information is then used to generate aggregate material compositions for use in ALARA.

ALARA is then run and PyNE R2S is used to convert ALARA output to a mesh of multigroup photon emission densities. This mesh is then used as a source for DAG-MCNP5 photon transport. This is done by utilizing the PyNE `source_sampling` module. This module provides a generic method for sampling the initial position and energy of MC particles (both neutrons and photons) from a mesh-based source with biased or unbiased sampling. MCNP5 ships with a customizable source subroutine: source.F90. A source.F90 file was written, incorporating the functionality of PyNE `source_sampling`, and was then compiled into DAG-MCNP5. DAG-MCNP5 photon transport is run with tallies in the region(s) of interest modified with flux-to-dose-rate conversion factors, which are used to obtain the SDR.

5.2 Deterministic Transport

PARTISN was used for all deterministic transport in this work. The PyNE `partisn` module contains functionality necessary to generate PARTISN input files automatically from CAD geometries and also read PARTISN output. This is done using the same geometry discretization capabilities described in Section 5.1. GT-CADIS and SNILB-violation methods require two deterministic adjoint transport steps: adjoint photon transport and adjoint neutron transport. For the adjoint photon step, the adjoint source is the detector of interest, which may be defined a by volume in a CAD geometry or a mesh. For the adjoint neutron transport step, the adjoint neutron source is defined by a mesh. The PyNE `partisn` module allows either CAD geometry cells or a mesh to used be to define PARTISN sources. In both cases the

source must be isotropic. The former case is implemented by discretizing the source volumes onto the mesh using the CAD geometry discretization capabilities described in Section 5.1, then using the mesh-based source capability.

5.3 T from GT-CADIS and SNILB-Violation Methods

A free-standing package referred to as gtcadis_tools has been written in order to calculate T using GT-, GTS-, GTB-, and GTSB-CADIS methods, as described in Chapter 4, as well as η and η_I as described in Section 3.3. These quantities are calculated by automatically carrying out the necessary irradiations using ALARA and then applying the appropriate formula to the resulting photon emission densities. In the case of T calculated by GTB- and GTSB-CADIS, individual $\mathsf{T}_{g,h}$ values may be negative as described in Section 4.2. These nonphysical quantities are replaced $\mathsf{T}_{g,h}$ values calculated by GT- or GTS-CADIS respectively (as described in Section 4.2).

A few special provisions are also made in the calculation of η. In the case where both the numerator and denominator of η are zero, η is assigned to be 1. If a material does not emit photons after irradiation and decay, GT-CADIS or the SNILB methods will produce the correct result, with all values in T equal to zero. Since $\eta = 1$ indicates that the GT-CADIS method will perform optimally, assigning $\eta = 1$ in the case of no photon emission is consistent with this designation. If the numerator of η is nonzero and the denominator is zero then η is set to infinity.

In Chapter 6, η is evaluated for a variety of materials and nuclides. For some of these materials/nuclides, the photon emission density after irradiation and decay is extremely small, and dominated by the decay of a radioactive starting material. Photons emitted from radioactive starting materials are unlikely to play a role in SDR analysis for realistic problems. However, these photons interfere with the calculation of η. To combat this, an additional irradiation/decay is conducted with all neutron fluxes set to zero in order to determine the

photon emission density contribution from radioactive starting materials. This contribution is then subtracted from both the numerator and denominator of η. The provisions made in the calculation of η are also made in the calculation of η_I.

5.4 CADIS

Sections 5.2 and 5.3 explained how deterministic transport is conducted and how T is obtained. Using the capabilities in these sections adjoint neutron fluxes can be obtained (via GT-CADIS or SNILB-violation methods), which must be converted into weight windows and biased sources via the CADIS method as discussed in Section 2.2.2. This is done using the `cadis` function in the PyNE `variance_reduction` module. This function reads a source density distribution from a mesh, as well as mesh-based adjoint fluxes and outputs a biased source density distribution and weight window lower bounds in the form of an MCNP5 WWINP file. The resulting biased source density distribution can be used for MC transport with the biased sampling mode of the PyNE `source_sampling` module described in Section 5.1. The PyNE `source_sampling` routine will sample these biased emission densities and adjust the statistical weight of the particles accordingly. One limitation of this approach is that in order to use biased neutron source sampling via GT-CADIS or SNILB-violation methods, the forward neutron source must be defined on a mesh.

Chapter 6

Evaluation of the SNILB Criteria for FES Scenarios

The SNILB solution for T is only valid if the SNILB criteria are met. If this is the case, the GT-CADIS method will produce optimal neutron VR parameters — otherwise SNILB-violation methods are necessary. In this chapter the extent to which the SNILB criteria are met for typical FES spectra, materials, and irradiation scenarios is explored in order to predict the applicability of the GT-CADIS and SNILB-violation methods. A set of characteristic neutron spectra for a first wall, shield, and vacuum vessel were obtained from a deterministic radiation transport calculation with a 2D model of an ITER blanket module. Characteristic materials were obtained from the ITER CLITE SDR model, version 1, release 131031. This collection of materials should not be considered exhaustive; ITER is an experimental device and not a fusion power plant.

Using each material in the ITER CLITE SDR model, η (defined in Equation 3.34) was evaluated for a wide range of irradiation/decay times. Values of η far from 1 were investigated through analysis of reaction pathways. This process was also done for η_{I}, (defined in Equation 3.33) in order to determine the extent to which SNILB violations affect important photon energy groups for the case of SDR analysis. Finally, η was evaluated for every nuclide in the FENDL-3.0 nuclear data library [38] in order to determine the extent to which the SNILB criteria are met for nuclides that may be relevant to fusion neutronics (or other applications) but do not appear in the ITER CLITE SDR model.

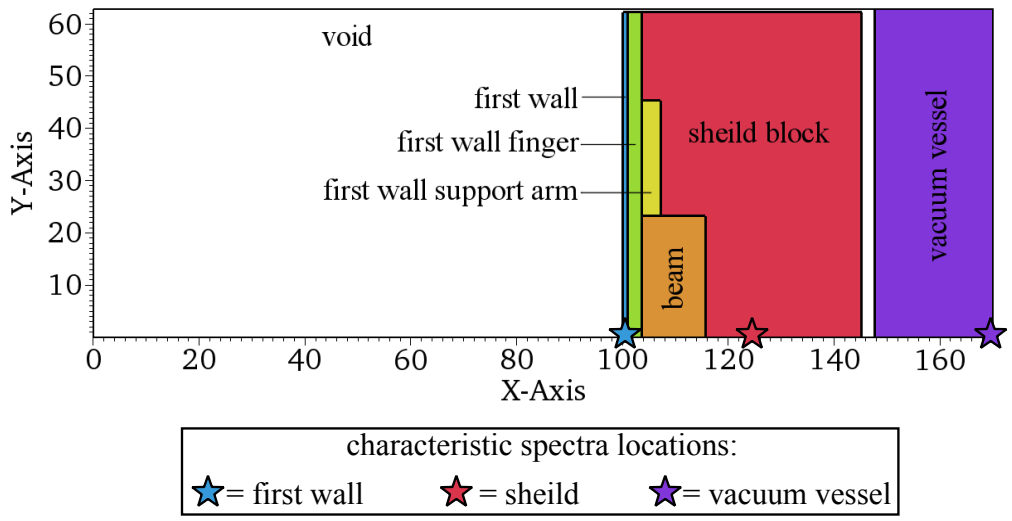

Figure 6.1: Simplified 2D model of ITER EHF BM14, produced by Mohamed E. Sawan [39].

6.1 Characteristic Spectra

The quantities η and η_I are dependent on the neutron spectrum used for the irradiations which determine the photon emission densities for the numerators and denominators. In order to assess the extent to which the SNILB criteria are valid for FES scenarios, characteristic neutron spectra were obtained. The spectra were obtained from a deterministic neutron transport calculation using a 2D model of an ITER blanket module, originally used for estimating nuclear heating and radiation damage parameters within published work [39]. The model represents Enhanced Heat Flux (EHF) Blanket Module (BM) 14 and contains a first wall, shield block, and vacuum vessel. BM14 is located on the outboard, immediately above the ITER midplane. Since the neutron wall loading is highest near the midplane [39], and the SNILB are expected to be violated with high fluences, neutron spectra from this model provide a conservative choice of characteristic spectra for further analysis.

The geometry specification for this 2D model is shown in Figure 6.1. The accompanying material specifications for each geometry volume are shown in Table 6.1. The model represents half of EHF BM 14, with reflecting boundaries both each sides (i.e., reflecting over $y = 0$ and $y = 62.85$). An additional reflecting boundary exists on the left side of the geometry (i.e., reflecting over $x = 0$) in order to account for contributions from other portions of the

Table 6.1: Material compositions for ITER EHF BM14 2D model.

region	volume fraction				
	stainless steel	water	CuCrZr	Be	void
first wall	-	-	-	1.00	-
first wall finger	0.389	0.218	0.366	-	0.027
first wall support arm	0.682	0.267	0.010	-	0.041
beam	0.738	0.238	-	-	0.024
shield block	0.861	0.083	-	-	0.056
vacuum vessel	0.700	0.300	-	-	-

geometry. A vacuum boundary condition is used behind the vacuum vessel (i.e., $\mathfrak{x} = 170$). Though it is difficult to discern in Figure 6.1, there is a 0.75 cm void gap connecting the void region within the chamber and the void region between the shield block and vacuum vessel. A ray-tracing first collision source was used in order to specify an isotropic 14.1 MeV neutron source, distributed uniformly within the void region in front of the first wall. A complete PARTISN input file for this geometry, materials, and source was obtained directly from the author of the paper, Mohamed E. Sawan.

Using the provided PARTISN input file, PARTISN was run with $\mathsf{P}_5\mathsf{S}_{16}$, FENDL-2.1 nuclear data [40], and the VITAMIN-J [41] group structure (175 neutron groups). An example neutron flux distribution for the 12.5 – 12.8 MeV energy group is shown in Figure 6.2. This figure shows that the 12.5 – 12.8 MeV energy group flux drops by four orders of magnitude through the first wall, shield, and vacuum vessel with minimal variation in the $\mathfrak{y}$-direction. Characteristic neutron spectra were then taken from locations in the first wall, shield block, and vacuum vessel, denoted in Figure 6.1. These spectra are shown in Figure 6.3.

Figure 6.3 shows that at the first wall, fast neutrons dominate. Within the shield block, fast, epithermal, and thermal neutron intensities are commensurate, in the 10^{11} – 10^{12} range. Within the vacuum vessel, fast and epithermal neutrons have intensities that are an order of magnitude lower than thermal neutron intensities. The total neutron flux for the three

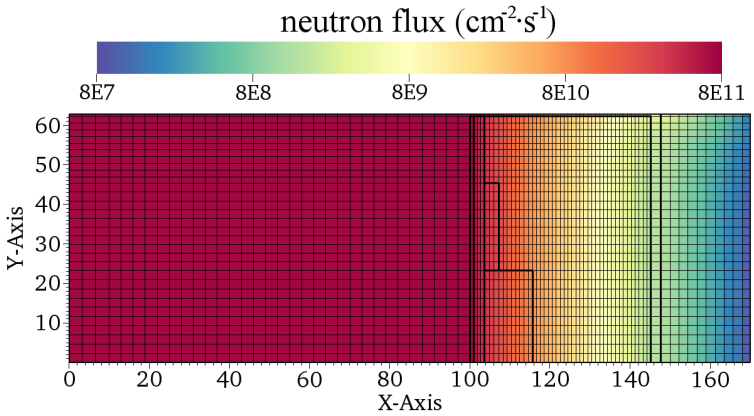

Figure 6.2: Neutron flux distribution for the 12.5 – 12.8 MeV energy group.

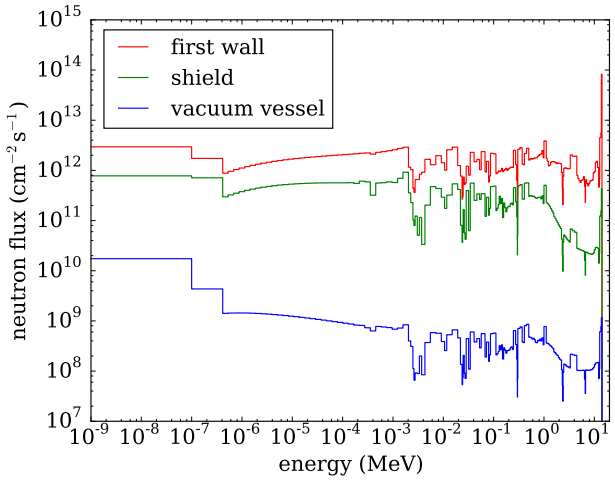

Figure 6.3: Characteristic neutron fluxes from the locations shown in Figure 6.1. Total fluxes for the first wall, shield, and vacuum vessel are $3.18 \cdot 10^{14}$, $4.27 \cdot 10^{13}$, and $9.57 \cdot 10^{10}$ cm^{-2} s^{-1}, respectively.

characteristic spectra are $3.18 \cdot 10^{14}$, $4.27 \cdot 10^{13}$, and $9.57 \cdot 10^{10}$ cm^{-2} s^{-1}, respectively. These three spectra are both characteristic of neutron spectra found within FES and provide variety in terms of relative intensities of fast, epithermal, and thermal neutrons. These properties make these spectra good choices for further investigation of the validity of the SNILB criteria for FES applications.

6.2 Characteristic Materials

Characteristic materials are required to assess the extent to which the SNILB criteria are met within FES scenarios. For this, the ITER CLITE SDR MCNP5 model, version 1, release 131031 was chosen as a representative sample of typical FES materials. This model is a detailed 40° sector endorsed by the ITER organization for SDR analysis. Though in the past separate material definitions were used for transport and activation (in order to save computer memory for transport), this model contains complete material definitions suitable for activation [42]. In addition to pure materials, this model contains some mixtures of pure materials (e.g., 94.89 vol. % SS316L(N)-IG and 5.11 vol. % water mixture) used within homogenized regions of the problem. For this analysis only the 22 pure materials within the geometry were considered, with the understanding that any mixture can be created through the linear combination of these materials.

The pure materials from this model are shown in Table 6.2 along with brief descriptions. Each material is assigned a unique name that will be used throughout the remainder of this document. Several of these materials are the names of elements (i.e., “beryllium”, “copper”, “tungsten”). These refer to bulk materials, with impurities present as specified by manufacturers. To avoid confusion, written-out names will be used to specify these mixtures, whereas chemical symbols (i.e., “Be”, “Cu”, “W”) will be used to specify pure elements. Several materials in Table 6.2 contain “M” followed by a number in the unique name. This is the MCNP material number within the model and is only present to create a unique name. Though these materials (e.g., SS316L M106, SS316L M108) are similar in composition, the importance of impurities in nuclear activation analysis motivates the inclusion of all variants.

In addition to analysis using the CLITE materials, analysis with all nuclides in the FENDL-3.0 nuclear data library is also done, to account for any nuclides that may be important to FES analysis but not present within the CLITE model. This is discussed in Section 6.5.

Table 6.2: Materials from the ITER CLITE SDR model, version 1, release 131031 and accompanying details [43].

Unique name	Description/comments
Beryllium	99 w% Be, additional impurities, first wall material
Concrete	Bioshield material
Copper	Oxygen-free copper, 99 w% Cu, additional impurities, for electronics
CuCrZr-IG	Additional impurities, for blanket modules
NiAl Bronze	$CuAl_{10}Ni_5Fe_4$, additional impurities, for blanket
SS304	Grade X5CrNi18-10, for vacuum vessel ports
SS304B4	A borated steel for in-wall shielding
SS304B7	A borated steel for in-wall shielding
SS304L	Grade X2CrNi18-9, for vacuum vessel ports
SS304LN	Grade X2CrNiN18-10 (No. 1.4311) austenitic stainless steel, for vacuum vessel/cryostat thermal shields
SS304/304L	Dual marked austenitic steel for cryostat
SS316L M106	Grade X2CrNiMo17-12-2, for vacuum vessel piping, vacuum vessel ports piping, upper and equatorial generic port plug piping
SS316L M108	EN grade No. 1.4404, for divertor piping
SS316L M111	Austenitic stainless steel for PF coil
SS316LN	Austenitic stainless steel for PF coil
SS316L(N)-IG M100	Austenitic steel for blanket
SS316L(N)-IG M101	Austenitic steel for divertor, vacuum vessel bars, vacuum vessel ports, vacuum vessel gravity supports, upper and equatorial generic port plugs
SS430	For in-wall shielding
Steel 660	Grade X6NiCrTiMoVB25-15-2 (No. 1.4980), for blanket
Tungsten	Guaranteed 99.96 w% W, numerous impurities, manufacturer: Plansee AG, used in divertor
Water	Specification includes ^2H
XM-19	Austenitic steel used within blanket

6.3 Evaluation of η for FES Materials

As discussed in Section 3.3, the quantity η can be used to assess the extent to which the SNILB criteria are met. The quantity η_I can assess the extent to which the SNILB criteria are met for important reaction pathways (i.e., pathways that produce photons important to a response function), which ultimately determines the efficacy of the GT-CADIS method. However, η_I requires the assignment of importance factors to photon energy groups. This is an application-specific task, as different applications may require different response functions. For this reason, the evaluation of η is attractive for drawing general conclusions about the extent to which the SNILB criteria are met, and the general applicability of the GT-CADIS method. The evaluation of η_I for the specific application of SDR analysis is done in the next section.

The quantity η was evaluated for each of the 22 materials in Table 6.2 using each of the three neutron spectra in Figure 6.3 for a sweep of irradiation and decay times. For the sweep, 30 irradiation and 30 decay intervals were chosen, logarithmically spaced between 10^0 s and 10^9 s (~ 31.7 years). For each combination of irradiation and decay times, η was evaluated using the software described in Section 5.3. The η values were then plotted.

An example of such a plot is shown in Figure 6.4 for beryllium and the first wall spectrum.

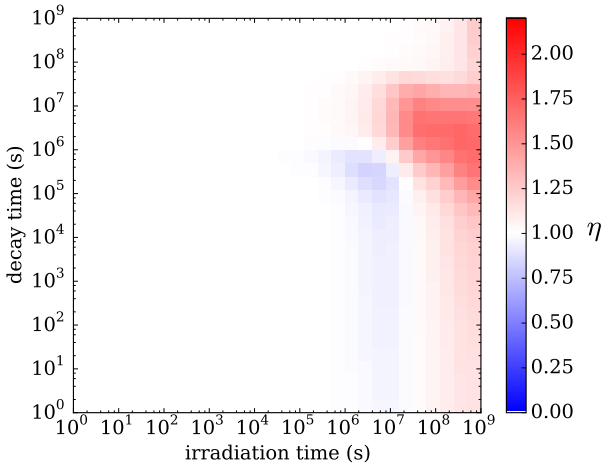

Figure 6.4: Example η plot: beryllium from Table 6.2 with the first wall neutron spectrum from Figure 6.3.

Table 6.3: Minimum and maximum η values for the materials in Table 6.2, the spectra from Figure 6.3, and irradiation and decay times sweeping over the interval 10^1 – 10^9 s.

	η					
	first wall		shield		vacuum vessel	
Material	min	max	min	max	min	max
Beryllium	0.83	1.72	0.89	2.10	1.00	1.00
Concrete	1.00	2.17	1.00	1.37	1.00	1.00
Copper	0.90	1.04	0.85	1.02	1.00	1.00
CuCrZr-IG	0.92	1.18	0.92	1.28	1.00	1.00
NiAl Bronze	0.94	1.26	0.88	1.67	1.00	1.00
SS304	0.98	1.12	0.95	1.15	1.00	1.00
SS304B4	0.93	1.13	1.00	1.07	1.00	1.00
SS304B7	0.93	1.13	1.00	1.07	1.00	1.00
SS304L	0.98	1.12	0.95	1.15	1.00	1.00
SS304LN	1.00	1.12	1.00	1.08	1.00	1.00
SS304/304L	1.00	1.12	1.00	1.08	1.00	1.00
SS316L M106	0.89	1.27	0.83	1.63	1.00	1.00
SS316L M108	0.97	1.17	0.88	1.30	1.00	1.00
SS316L M111	1.00	1.13	1.00	1.08	1.00	1.00
SS316LN	1.00	1.13	1.00	1.08	1.00	1.00
SS316L(N)-IG M100	0.95	1.14	0.96	1.15	1.00	1.00
SS316L(N)-IG M101	0.95	1.14	0.96	1.15	1.00	1.00
SS430	0.96	1.19	1.00	1.07	1.00	1.00
Steel 660	1.00	1.18	0.89	1.28	1.00	1.00
Tungsten	0.06	2.84	0.59	1.20	1.00	1.00
Water	1.00	1.00	1.00	1.00	1.00	1.00
XM-19	0.94	1.13	0.97	1.14	1.00	1.00

The irradiation and decay times used to generate each square in the plot are the times at the center of the square. This figure shows that for irradiation times less than $\sim 10^5$ s, the SNILB criteria are met. At long irradiation times, the superposition assumption in Equation 3.31 either overestimates the photon emission density (red region, $\eta > 1$), or underestimates (blue region, $\eta < 1$). The maximum overestimation is $\eta = 1.73$ and the minimum underestimation is $\eta = 0.83$. This minimum and maximum information, as well as the analogous information for the η plots for each material and neutron spectra are shown in Table 6.3.

In Table 6.3 it can be seen that for the majority of the material and spectrum combinations,

η is near 1.0. For most materials, η has less deviation from 1 for the shield spectrum than the first wall spectrum. With the vacuum vessel spectrum, every material yielded $\eta = 1.00$ for all irradiation/decay times. In the η plot in Figure 6.4, and the other η plots in this section, η is near 1 at short irradiation times and deviates at long irradiation times. This evidence suggests the general trend that η deviation increases with fluence. This is consistent with the SNILB criteria: both burnup and the importance of pathways that involve multiple neutron interactions are positively correlated with fluence.

Though most η values in Table 6.3 are near 1, nearly all materials except water had at least a 10% deviation for some combination of spectrum and irradiation/decay scenario. An η of 1.1 indicates that GT-CADIS will overestimate the importance of a material by 10%. Since VR parameters generally vary by many orders of magnitude, 10% overestimations of importance are unlikely to have a significant impact on performance. Since Table 6.3 shows minimum and maximum deviations from $\eta = 1$ for each of the spectra, some of these deviations may result from irradiations that are unlikely to occur in FES applications. For example, concrete, a bioshield material is unlikely to experience a first wall spectrum, let alone for 10^9 s.

Despite the fact that most η deviations are small, and some η deviations result from material, spectra, and irradiation/decay scenario combinations unlikely to occur in FES applications, it worthwhile to explore the mechanisms that result in η deviations in order to better understand how the SNILB criteria can be violated. The reaction pathways that cause these discrepancies are determined for the six materials with the largest deviation from $\eta = 1$: beryllium, NiAl bronze, concrete, tungsten, SS316L M106, and SS316L M108. All of these materials have η deviations of at least 30%. This analysis is done in the following subsections.

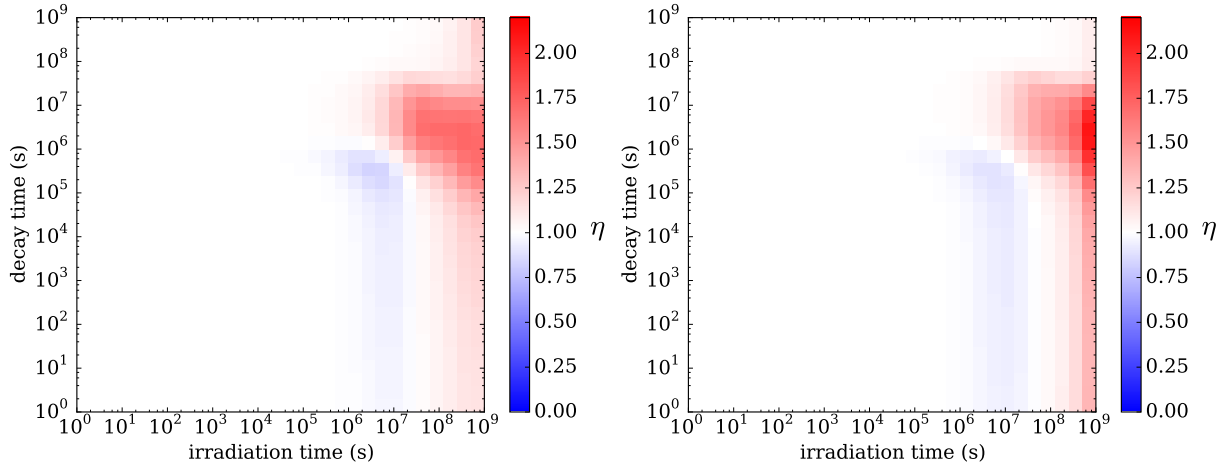

(a) First wall (b) Shield

Figure 6.5: Plots of η for beryllium using the first wall and shield neutron spectra from Figure 6.3.

6.3.1 Beryllium

Many materials in Table 6.3 showed their largest deviations from $\eta = 1$ with the first wall spectrum. Since beryllium is the ITER first wall material, it is guaranteed to experience this spectrum, so it is of special interest. As mentioned in Section 6.2, the beryllium material is not exclusively Be, but contains a large number of impurities, including ^{181}Ta. A full material specification can by found within ITER documents [42].

The η plots for beryllium using the first wall and shield spectra are shown in Figure 6.5. The η plot for the vacuum vessel spectrum is omitted here (and in proceeding sections for other materials) because $\eta = 1.00$ for all irradiation and decay times, as seen in Table 6.3. The plots in Figure 6.5 have a similar shape, with blue and red regions appearing at similar irradiation and decay times.

6.3.1.1 $\eta > 1$

The mechanism causing the $\eta > 1$ behavior was first explored. This was done with an ALARA calculation using the first wall spectrum for an irradiation time of 10^9 s and a decay time of 10^6 s. This combination of irradiation and decay appears in the middle of the red

Table 6.4: Values of η for nuclides from the irradiation of the beryllium material, with an irradiation time of 10^9 s and a decay time of 10^6 s. The numerator and denominator of η, $\sum_g q_p(\phi_{n,g})$ and $q_p(\phi_n)$ respectively are also included. Nuclides appear in descending order of $q_p(\phi_n)$.

nuclide	$\sum_g q_p(\phi_{n,g})$ ($s^{-1}cm^{-3}$)	$q_p(\phi_n)$ ($s^{-1}cm^{-3}$)	η
total (all nuclides)	$1.05 \cdot 10^9$	$6.23 \cdot 10^8$	1.68
Top 11 nuclides:			
^{55}Fe	$1.79 \cdot 10^8$	$1.54 \cdot 10^8$	1.16
^{54}Mn	$1.10 \cdot 10^8$	$1.15 \cdot 10^8$	0.963
^{60}Co	$1.56 \cdot 10^8$	$1.13 \cdot 10^8$	1.39
^{57}Co	$1.20 \cdot 10^8$	$1.10 \cdot 10^8$	1.08
^{58}Co	$9.99 \cdot 10^7$	$6.05 \cdot 10^7$	1.65
^{192}Ir	$2.98 \cdot 10^4$	$1.29 \cdot 10^7$	$2.32 \cdot 10^{-7}$
^{191m}Ir	$4.65 \cdot 10^4$	$1.00 \cdot 10^7$	$4.61 \cdot 10^{-7}$
^{185}Os	$5.18 \cdot 10^2$	$8.00 \cdot 10^6$	$6.47 \cdot 10^{-5}$
^{46}Sc	$6.14 \cdot 10^6$	$7.42 \cdot 10^6$	0.827
^{51}Cr	$5.99 \cdot 10^6$	$6.07 \cdot 10^6$	0.987
^{182}Ta	$3.11 \cdot 10^8$	$5.21 \cdot 10^6$	59.8

region within Figure 6.5(a). This irradiation and decay scenario resulted in an η of 1.68. In addition to total photon emission densities, ALARA outputs photon emission densities for each nuclide individually. This allows for the calculation of η for individual nuclides. Table 6.4 show η values for the top 11 nuclides that contribute to photon emission density. It also shows the photon emission density calculated via the superposition of single-energy-group neutron irradiations (i.e., the numerator of Equation 3.34) and the photon emission density calculated with an irradiation of all energy groups simultaneously (i.e., the denominator of Equation 3.34). Note that the summation over all photon energy groups is suppressed.

Table 6.4 shows that the largest contributor to the photon emission density is ^{55}Fe, with an η of only 1.16. Most of the other nuclides have large η deviations as well, notably ^{192}Ir, ^{191m}Ir, ^{185}Os, with η values close to zero. The main cause of the overall η value of 1.68 for the beryllium material is the overestimation of the ^{182}Ta photon emission density, with $\eta = 59.8$, which suggests an excess of ^{182}Ta.

Using the ALARA tree file output capability it was found that ^{182}Ta results from ^{181}Ta,

^{182}W, and ^{183}W starting nuclides. During irradiation, the number densities of ^{181}Ta and ^{182}W decreased by factors of 58.7 and 19.6, respectively. In other words, the low-burnup component of the SNILB criteria is egregiously violated. This manifests itself in an η much greater than 1.0 because irradiations with neutrons from a single energy group cause significantly less burnup then irradiating will all energy groups simultaneously, so the ^{182}Ta production rate does not slow down as much. For the 175 single-energy-group irradiations (with the first wall spectrum) ^{181}Ta had an average burnup of less than 2%. In conclusion, though ^{182}Ta is a minor contributor to the total photon source density when irradiating with all energy groups simultaneously, the burnup of its parents violates the SNILB so severely that the total photon emission density calculated though groupwise irradiations differs by a factor of 59.8, skewing η. This mechanism is consistent with the high-burnup effect on the GT-CADIS estimate of T, as described in Section 4.1.4.1.

6.3.1.2 $\eta < 1$

To investigate the cause of the blue region in Figure 6.5(a), an ALARA calculation was done using the first wall neutron spectrum with an irradiation time of $2 \cdot 10^6$ s and a decay time of $2 \cdot 10^5$ s. This resulted in an η of 0.889. As was done in Section 6.3.1.1, a table

Table 6.5: Values of η for nuclides from the irradiation of the beryllium material, with an irradiation time of $2 \cdot 10^6$ s and a decay time of $2 \cdot 10^5$ s. The numerator and denominator of η, $\sum_g q_p(\phi_{n,g})$ and $q_p(\phi_n)$ respectively are also included. Nuclides appear in descending order of $q_p(\phi_n)$.

nuclide	$\sum_g q_p(\phi_{n,g})$ ($s^{-1}cm^{-3}$)	$q_p(\phi_n)$ ($s^{-1}cm^{-3}$)	η
total (all nuclides)	$4.64 \cdot 10^8$	$5.22 \cdot 10^8$	0.889
Top 5 nuclides:			
^{187}W	$1.69 \cdot 10^8$	$1.68 \cdot 10^8$	1.00
^{24}Na	$1.09 \cdot 10^8$	$1.09 \cdot 10^8$	1.00
^{182}Ta	$1.03 \cdot 10^8$	$9.38 \cdot 10^7$	1.09
^{183}Ta	$4.58 \cdot 10^5$	$6.69 \cdot 10^7$	0.00685
^{58}Co	$2.33 \cdot 10^7$	$2.16 \cdot 10^7$	1.08

of η and its subcomponents for the top contributing nuclides is shown in Table 6.5. This table shows that groupwise irradiations result in a deficit in photon emission density of $5.22 \cdot 10^8 - 4.64 \cdot 10^8 = 5.80 \cdot 10^7$ cm^{-3}s^{-1}. Besides ^{183}Ta, every nuclide in the top 5 is within 10% of $\eta = 1.0$. This deficiency is entirely accounted for by the lack of ^{183}Ta. The production of ^{183}Ta is dominated by:

$$\underset{(1.0)}{^{181}\text{Ta}} \xrightarrow{(\text{n},\,\gamma)} \underset{(0.00994)}{^{182}\text{Ta}} \xrightarrow{(\text{n},\,\gamma)} \underset{(0.00803)}{^{183}\text{Ta}} \xrightarrow{\text{other reactions}} \underset{(0.000456)}{\ldots} \tag{6.1}$$

where the numbers in parenthesis denote the number density of each nuclide relative to the parent (^{181}Ta). This pathway involves two neutron interactions and therefore violates the single-neutron-interaction portion of the SNILB criteria. The underestimation of ^{183}Ta production comes from the fact that the two neutron interactions occur predominantly at different neutron energy groups. Figure 6.6 shows the amount of ^{182}Ta and ^{183}Ta produced as a function of neutron energy using groupwise irradiations for this irradiation/decay scenario. The production of ^{182}Ta is dominated by a single neutron energy group: 3.93 –5.04 eV. The production of ^{183}Ta comes primarily from the two lowest energy neutron groups, despite the fact that only a small amount of ^{182}Ta is present.

This observation is supported by the cross section data shown in Figure 6.7. In this plot, the 3.93 –5.04 eV energy group is highlighted and shows that a large resonance for ^{182}Ta occurs within this group. Likewise, the cross section for ^{183}Ta production in this group is several orders of magnitude lower than the cross sections for lower neutron energies. In conclusion, η is less than 1.0 because groupwise irradiations underestimate the production of ^{183}Ta because it is produced via a pathway involving multiple neutron interactions that primarily occur at different energies. This mechanism is consistent with the mechanism originally described in Section 4.1.4.2.

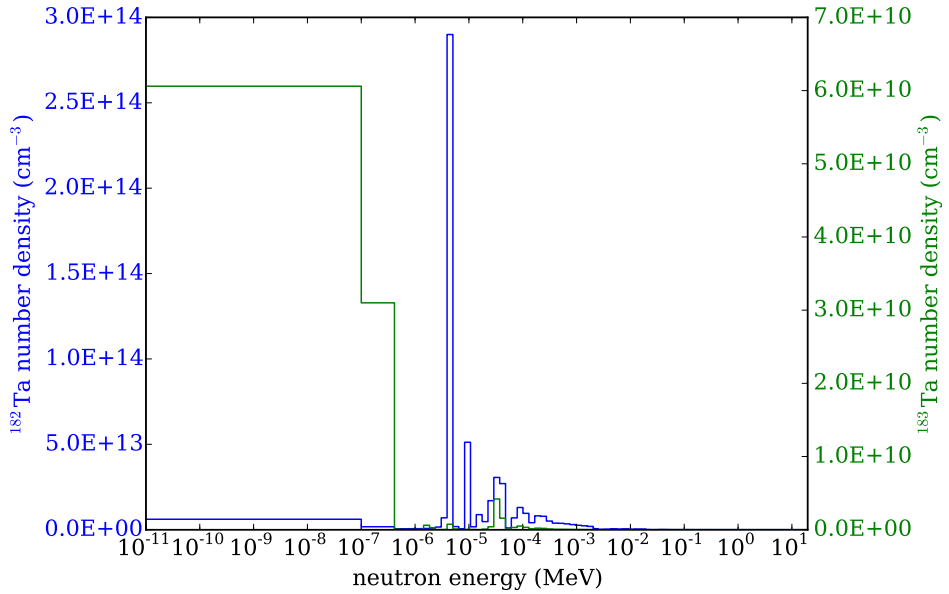

Figure 6.6: ^{182}Ta and ^{183}Ta production as function of neutron energy using groupwise irradiations with an irradiation time of $2 \cdot 10^6$ s and a decay time of $2 \cdot 10^5$ s.

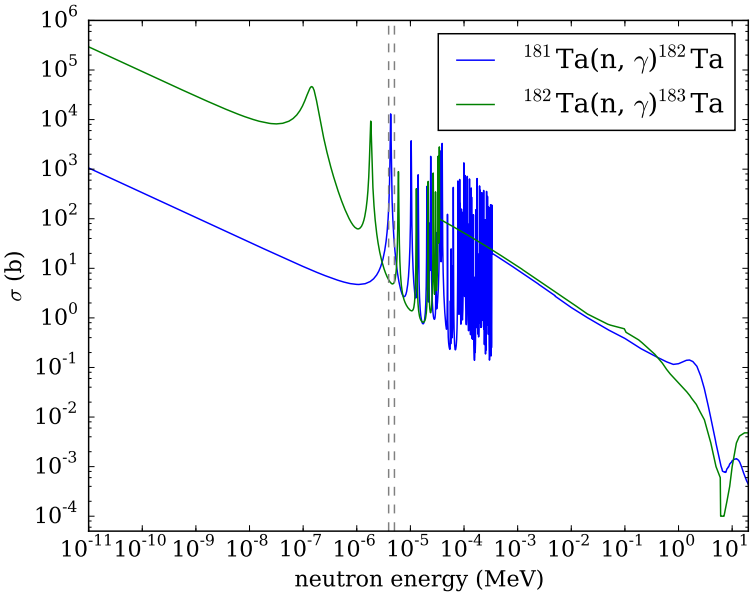

Figure 6.7: Cross sections for ^{182}Ta and ^{183}Ta production from ENDF/B-VII.1 [44]. Dashed lines show the bounds of the 3.93 – 5.04 eV energy group.

6.3.2 Concrete

Plots for η for the concrete material are shown in Figure 6.8. Unlike the beryllium material, η is never less than 1 for concrete. However, η is greater than 2 for scenarios with the longest

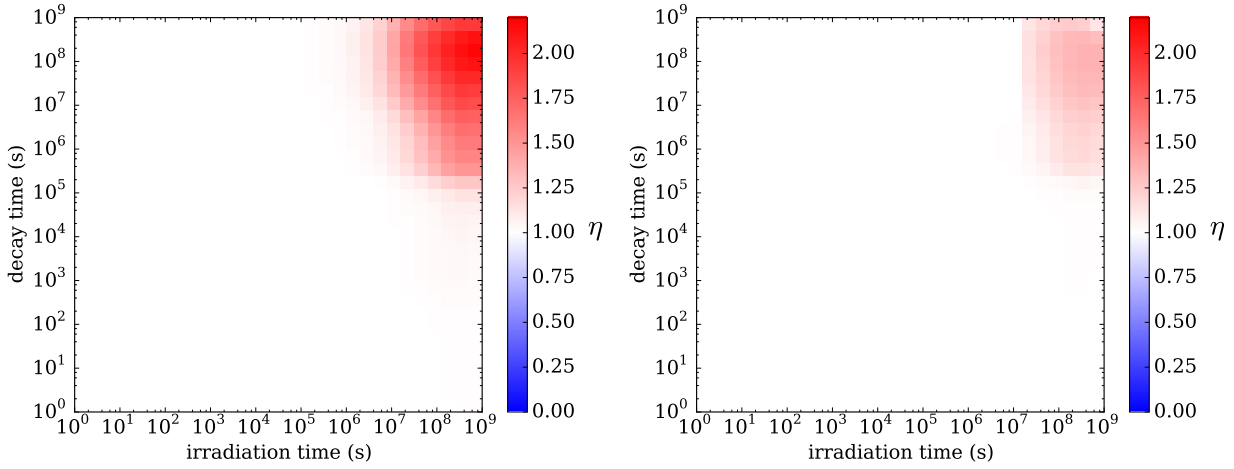

(a) First wall (b) Shield

Figure 6.8: Plots of η for concrete using the first wall and shield neutron spectra from Figure 6.3.

irradiation and decay times. To investigate this, an ALARA calculation was done with an irradiation time of $1 \cdot 10^9$ s and a decay time of $1 \cdot 10^6$ s. Values for η for the top 5 contributing nuclides are shown in Table 6.6. From this table is apparent that the $\eta > 1$ behavior comes from an excess of ^{22}Na. This nuclide is predominantly produced and subsequently destroyed by the following pathway:

$$\underset{(1.0)}{^{23}\text{Na}} \xrightarrow{\text{(n, 2n)}} \underset{(0.00126)}{^{22}\text{Na}} \xrightarrow{\text{(n, p) or } \beta^+ \text{ decay}} \underset{(0.00123)}{^{22}\text{Ne}} \tag{6.2}$$

Though this mechanism involves two neutron interactions, it does not violate the single-neutron-interaction portion of the SNILB criteria because the nuclide of interest, ^{22}Na, is in fact produced by a single neutron interaction. Instead, this mechanism violates the low-burnup portion of the SNILB criteria (Equation 3.27a). For the transmutation chain beginning with ^{23}Na and ending with ^{22}Na Equation 3.27a, simplifies to

$$(d_1 + d_2)t_{irr} \ll 2. \tag{6.3}$$

It is clear that t_{irr} is large relative to d_2 because nearly all of the ^{22}Na is transmuted to ^{22}Ne.

Table 6.6: Values of η for nuclides from the irradiation of the concrete material, with an irradiation time of $1 \cdot 10^9$ s and a decay time of $1 \cdot 10^6$ s. The numerator and denominator of η, $\sum_g q_p(\phi_{n,g})$ and $q_p(\phi_n)$ respectively are also included. Nuclides appear in descending order of $q_p(\phi_n)$.

nuclide	$\sum_g q_p(\phi_{n,g})$ ($s^{-1}cm^{-3}$)	$q_p(\phi_n)$ ($s^{-1}cm^{-3}$)	η
total (all nuclides)	$1.04 \cdot 10^{10}$	$6.57 \cdot 10^9$	1.58
Top 5 nuclides:			
^{55}Fe	$3.27 \cdot 10^9$	$2.81 \cdot 10^9$	1.17
^{54}Mn	$1.60 \cdot 10^9$	$1.74 \cdot 10^9$	0.919
^{37}Ar	$1.76 \cdot 10^9$	$1.58 \cdot 10^9$	1.12
^{22}Na	$3.52 \cdot 10^9$	$1.45 \cdot 10^8$	24.3
^{46}Sc	$2.09 \cdot 10^7$	$9.02 \cdot 10^7$	0.232

This violation is exacerbated by the fact that the two neutron interactions have cross sections that peak at much different neutron energies, as seen in Figure 6.9. The first reaction in Equation 6.2, ^{23}Na(n, 2n)^{22}Na is a threshold reaction that only occurs above ~13.0 MeV. The second reaction ^{22}Na(n, p)^{22}Ne has a much lower cross section above 13.0 MeV than at thermal energies. These cross sections further explain the $\eta > 1$ behavior: with groupwise irradiations, irradiations with high-energy neutrons result in production of ^{22}Na without significant (n, p) destruction. When irradiation is done with all energy groups simultaneously, the ^{22}Na produced from high-energy neutrons is consumed by reactions with low-energy neutrons.

Since concrete is used for the ITER bioshield it is unlikely to experience the first wall or shield spectra. Nonetheless, the mechanism described in this section may be relevant to any material containing ^{23}Na that does experience these spectra.

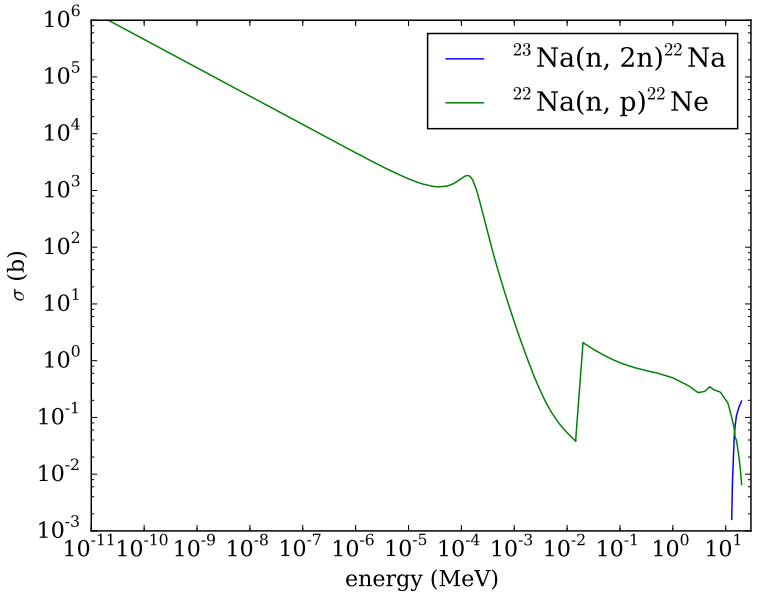

Figure 6.9: Cross sections for ^{22}Na and ^{22}Ne production via Equation 6.2 from ENDF/B-VII.1.

6.3.3 NiAl Bronze

Plots of η for NiAl bronze are shown in Figure 6.10. Qualitatively, the shape of these plots appear similar to those of beryllium in Figure 6.5. It was confirmed by an ALARA calculation with an irradiation time $2 \cdot 10^6$ s and a decay time of $2 \cdot 10^5$ s that the blue region results

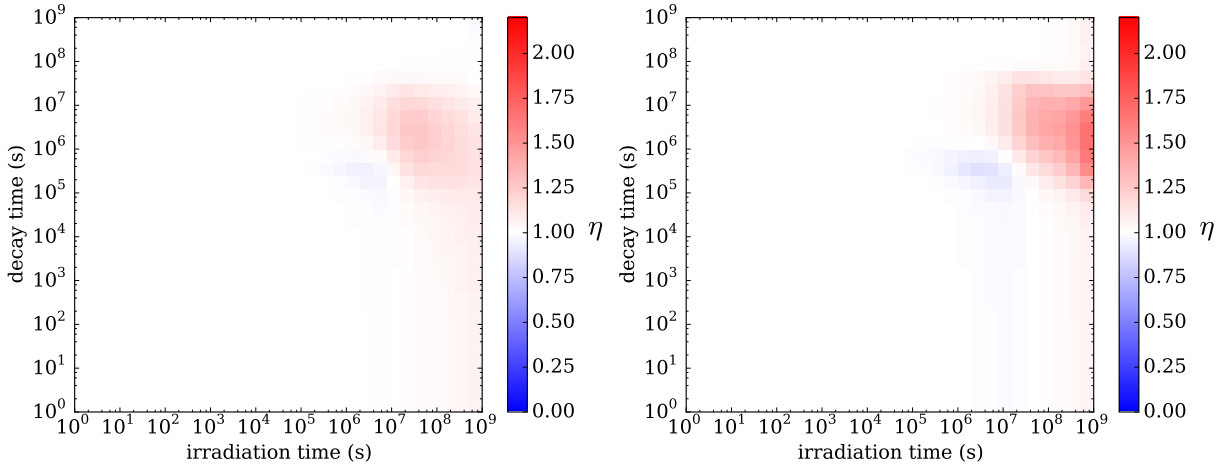

(a) First wall (b) Shield

Figure 6.10: Plots of η for NiAl Bronze using the first wall and shield neutron spectra from Figure 6.3.

Table 6.7: Values of η for nuclides from the irradiation of the beryllium material, with an irradiation time of $1 \cdot 10^9$ s and a decay time of $1 \cdot 10^6$ s. The numerator and denominator of η, $\sum_g q_p(\phi_{n,g})$ and $q_p(\phi_n)$ respectively are also included. Nuclides appear in descending order of $q_p(\phi_n)$.

nuclide	$\sum_g q_p(\phi_{n,g})$ ($s^{-1}cm^{-3}$)	$q_p(\phi_n)$ ($s^{-1}cm^{-3}$)	η
total (all nuclides)	$1.067 \cdot 10^{12}$	$9.577 \cdot 10^{11}$	1.11
Top 10 nuclides:			
^{60}Co	$4.361 \cdot 10^{11}$	$4.477 \cdot 10^{11}$	0.974
^{57}Co	$2.364 \cdot 10^{11}$	$2.183 \cdot 10^{11}$	1.08
^{58}Co	$1.859 \cdot 10^{11}$	$1.165 \cdot 10^{11}$	1.6
^{54}Mn	$8.666 \cdot 10^{10}$	$7.925 \cdot 10^{10}$	1.09
^{65}Zn	$5.926 \cdot 10^{8}$	$4.161 \cdot 10^{10}$	0.0142
^{55}Fe	$4.546 \cdot 10^{10}$	$3.970 \cdot 10^{10}$	1.15
^{59}Fe	$4.553 \cdot 10^{9}$	$7.084 \cdot 10^{9}$	0.643
^{95}Nb	$3.106 \cdot 10^{7}$	$1.862 \cdot 10^{9}$	0.0167
^{92m}Nb	$1.674 \cdot 10^{9}$	$1.604 \cdot 10^{9}$	1.04
^{182}Ta	$6.701 \cdot 10^{10}$	$7.207 \cdot 10^{8}$	93.0

from a deficit of ^{183}Ta, via the same mechanism described in Section 6.3.1.2.

Within the red region, top contributing nuclides are seen in Table 6.7. As with beryllium, an excess of ^{182}Ta is observed from the burnup of ^{181}Ta. In addition, ^{58}Co, the nuclide with the third-highest photon emission density has an η of 1.6. ^{58}Co is produced via a complex network of reactions from nuclides present within the starting materials: ^{58}Ni, ^{60}Ni, and ^{59}Co. After irradiation, ^{58}Ni is burned up by a factor of 0.859 and ^{60}Ni and ^{59}Co number densities increase by factors of 1.14 and 1.79 respectively. The fact that important nuclides both significantly increased and decreased in number density from irradiation indicates that the SNILB criteria are violated via multiple mechanisms which may include those which applied to the red regions for beryllium and concrete as discussed in Sections 6.3.1.1 and 6.3.2.

6.3.4 Tungsten

The η plots for tungsten are shown in Figure 6.11. These plots are more complex than plots shown previously. The first wall plot has two distinct red and two distinct blue regions,

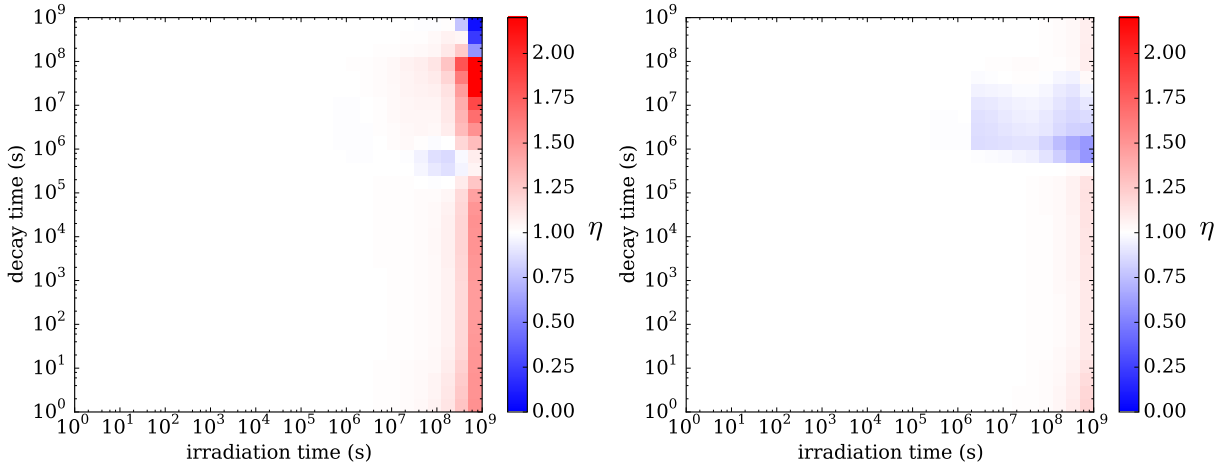

(a) First wall (b) Shield

Figure 6.11: Plots of η for tungsten using the first wall and shield neutron spectra from Figure 6.3.

though all of these regions occur at long irradiation times. The shield plot only has one blue region, but this region extends to lower irradiation times than the blue region in the first wall plot. Likewise, it was found that a multitude of nuclides contribute to these deviations from $\eta = 1.0$.

An ALARA calculation was carried out with an irradiation time of 10^9 s and a decay time of $3 \cdot 10^7$ s, yielding a total η of 2.55. The top 11 contributing nuclides by photon emission density are shown in Table 6.8. This table shows that nearly every nuclide within the top 11 greatly deviates from $\eta = 1.0$, with 7 nuclides deviating by more than an order of magnitude. The complex shape of the η plots — especially the dependence of η on decay time in the first wall plot — comes from different collections of these nuclides dominating the photon emission density at different times. Though some of the nuclides in Table 6.8 originate from impurities, many of the nuclides (e.g., ^{185}Os) originate from the W within the starting material, indicating that this SNILB violation is inherent within the tungsten material.

Table 6.8: Values of η for nuclides from the irradiation of the tungsten material, with an irradiation time of 10^9 s and a decay time of $3 \cdot 10^7$ s. The numerator and denominator of η, $\sum_g q_p(\phi_{n,g})$ and $q_p(\phi_n)$ respectively are also included. Nuclides appear in descending order of $q_p(\phi_n)$.

nuclide	$\sum_g q_p(\phi_{n,g})$ ($s^{-1}cm^{-3}$)	$q_p(\phi_n)$ ($s^{-1}cm^{-3}$)	η
total (all nuclides)	$5.69 \cdot 10^{11}$	$2.23 \cdot 10^{11}$	2.55
Top 11 nuclides:			
^{185}Os	$4.53 \cdot 10^{6}$	$7.03 \cdot 10^{10}$	$6.44 \cdot 10^{-5}$
^{192}Ir	$1.37 \cdot 10^{4}$	$6.99 \cdot 10^{10}$	$1.96 \cdot 10^{-7}$
^{182}Ta	$2.39 \cdot 10^{9}$	$3.61 \cdot 10^{10}$	0.0662
^{181}W	$4.69 \cdot 10^{11}$	$1.86 \cdot 10^{10}$	25.2
^{193}Pt	$6.65 \cdot 10^{3}$	$1.36 \cdot 10^{10}$	$4.89 \cdot 10^{-9}$
^{184}Re	$4.27 \cdot 10^{10}$	$6.31 \cdot 10^{9}$	6.76
^{184m}Re	$4.08 \cdot 10^{10}$	$6.12 \cdot 10^{9}$	6.67
^{60}Co	$2.15 \cdot 10^{9}$	$1.37 \cdot 10^{9}$	1.57
^{185}W	$2.05 \cdot 10^{8}$	$1.88 \cdot 10^{8}$	1.09
^{194n}Ir	$4.58 \cdot 10^{5}$	$1.81 \cdot 10^{8}$	$2.53 \cdot 10^{-9}$
^{179}Ta	$1.18 \cdot 10^{10}$	$1.17 \cdot 10^{8}$	101

6.3.5 SS316L M106 and M108

The SS316L M106 and M108 materials have similar compositions. The principle difference between these two materials is that M106 has more than twice as much ^{181}Ta as M108 and also contains Ti and Cu, which are not present in M108. These materials are used for piping within the vacuum vessel, port plugs, and divertor. Due to the small quantities of these materials present in the ITER device, the Ta content is not subject to standard radioprotection requirements [43].

Plots of η for the first wall and shield spectra for M106 and M018 are shown in Figures 6.12 and 6.13. These plots have similar shapes to the plots of the beryllium material in Figure 6.5, suggesting that ^{181}Ta may be the cause of the SNILB violations as it was for the beryllium material. Plots of η were also created for M106 and M108 with ^{181}Ta removed.

The minimum and maximum η values for these plots are shown in Table 6.9. This table shows that ^{181}Ta appears to be the principle contributor to the largest SNILB violations,

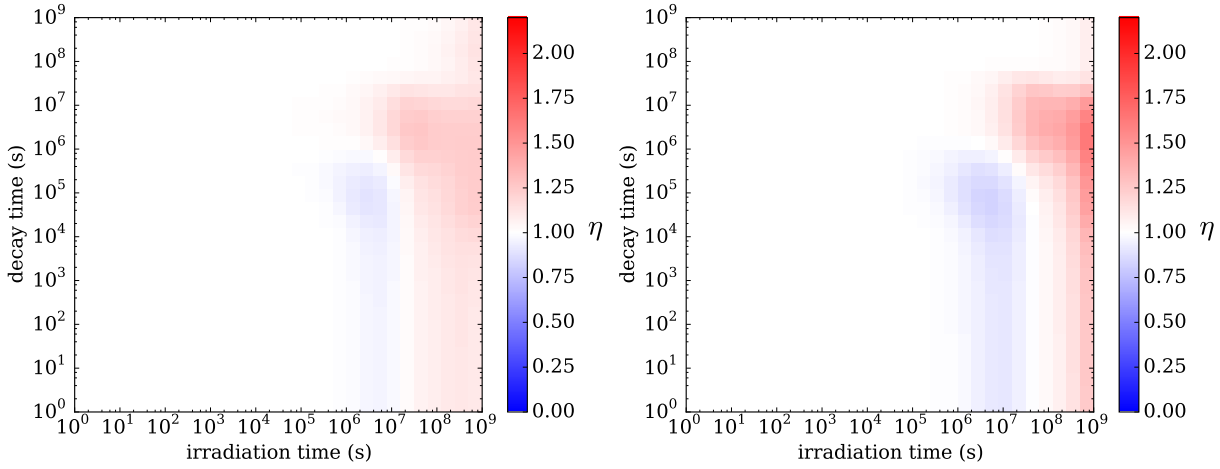

(a) First wall (b) Shield

Figure 6.12: Plots of η for SS316L (M106) using the first wall and shield neutron spectra from Figure 6.3.

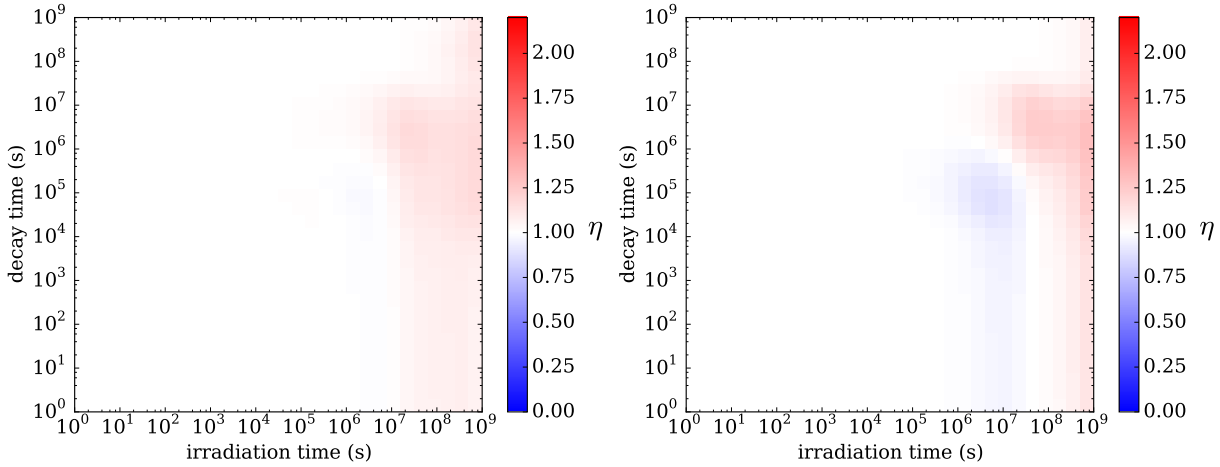

(a) First wall (b) Shield

Figure 6.13: Plots of η for SS316L (M108) using the first wall and shield neutron spectra from Figure 6.3.

occurring in the shield. Within the shield, η values for M106 and M108 without ^{181}Ta are similar to those found for structural stainless steels found in Table 6.3.

Table 6.9: Minimum and maximum η values for M106 and M108 in Table 6.2 with and without ^{181}Ta, the spectra from Figure 6.3, and irradiation and decay times sweeping over the interval 10^1 – 10^9 s.

	η					
	first wall		shield		vacuum vessel	
SS316L M106	0.89	1.27	0.83	1.63	1.00	1.00
SS316L M106, no ^{181}Ta	1.00	1.14	1.00	1.08	1.00	1.00
SS316L M108	0.97	1.17	0.88	1.30	1.00	1.00
SS316L M108, no ^{181}Ta	1.00	1.14	1.00	1.08	1.00	1.00

6.4 Evaluation of η_I for FES Materials

In Section 6.3, η was evaluated for all materials in the ITER CLITE SDR model using characteristic spectra for a sweep of irradiation and decay times. As discussed in Section 3.3, this evaluation of η provides an estimate of the extent to which the SNILB criteria are met for these scenarios. However, since the formulation of η in Equation 3.34 weights all energy groups equally, η does not directly measure the extent to which the GT-CADIS method will be effective. The GT-CADIS method can be effective if the SNILB criteria are violated, provided that the pathways which violate the SNILB criteria do not result in a significant quantity of photons in energy groups that are important. The opposite is also true; the case of $\eta = 1.0$ does not definitively indicate that the GT-CADIS method will be effective. It is possible that the SNILB criteria are met for pathways that produce a large quantity of unimportant photons, washing out the SNILB violations for important photons.

This issue is addressed with the quantity η_I defined in Equation 3.33. This quantity weights the photon intensity within each photon energy by factors I_h. For η_I to be meaningful, I_h must represent the importance of each photon energy group relative to a specific detector response function. Mathematically, I_h should be equivalent to adjoint photon flux resulting from adjoint transport using the detector response function of interest as the adjoint source (per Equation 2.8).

The response function of interest is application-specific; for SDR analysis, flux-to-dose-

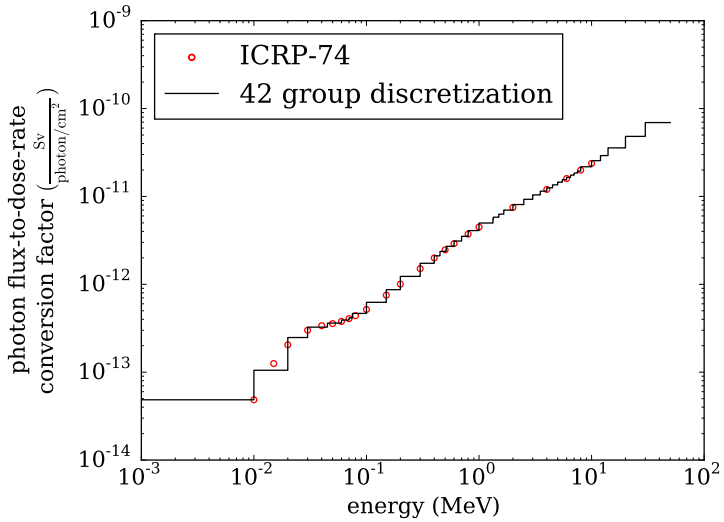

Figure 6.14: ICRP-74 pointwise flux-to-dose-rate conversion factors, collapsed into 42 energy groups using log-log interpolation.

rate conversion factors give the shape of the detector response function in energy space. However, since maintenance operations may be required in many different areas of a device, the position of the detector is not well-defined. Furthermore, even for a simple detector (e.g., flux-to-dose-rate conversion factors at a single point), the spectral shape of the adjoint flux is expected to vary strongly as a function of position due to the energy-dependence of photon cross sections. For these reasons it is challenging to select adjoint photon fluxes to use for I_h that will yield useful η_I. One solution is to simply use flux-to-dose-rate conversion factors as I_h; forgoing the introduction of any transport effects. Generally speaking, flux-to-dose-rate conversion factors are smooth functions that increase with energy. Since high-energy photons generally have longer mean free paths than low-energy photons, the disparity between high- and low-energy I_h values is less when using flux-to-dose-rate conversion factors for I_h as opposed to adjoint fluxes. This means that when using flux-to-dose-rate conversion factors as I_h, any differences observed between η_I and η may be less than if adjoint fluxes are used for I_h.

For analysis in this section (and the rest of this work) ICRP-74 flux-to-dose-rate conversion factors were used for I_h. In order to do this, the pointwise ICRP-74 data was discretized into

the 42 VITAMIN-J photon energy groups. This was done using the `pointwise_collapse` function in the PyNE `bins` module. Log-log interpolation was used for this collapsing. The lowest energy point in the pointwise data is 1 keV. The first energy bin in the 42 group structure is 0.0 – 1.0 keV, so this bin was assigned the flux-to-dose-rate conversion factor equal to that of the 1 keV point. For energy bins above the highest energy point in ICRP-74 (10 MeV), flux-to-dose-rate conversion factors were extrapolated. The 42-group discretization is compared to the pointwise data in Figure 6.14.

Using ICRP-74 flux-to-dose-rate conversion factors for I_h, η_I plots were created in the same fashion as the η plots produced in Section 6.3. The minimum and maximum η_I values from these plots are shown in Table 6.10. In general, η_I values in this table are close to the η values in Table 6.3, indicating that violations of the SNILB criteria for these materials occur for photons that are important with respect to dose rates. Values are within 20% of the corresponding η values from Table 6.3 for all materials except for the concrete and tungsten: materials identified in Section 6.3 to have the largest SNILB criteria violations.

In Section 6.3 it was concluded that for typical FES materials, neutron spectra, and irradiation scenarios, the SNILB criteria are generally met, with minor violations. No major violations were identified from the calculation of η_I that did not occur in the calculation of η. These results indicate that the GT-CADIS method should be effective for typical FES scenarios and that either η or η_I can be used to estimate this efficacy.

Table 6.10: Minimum and maximum η_I values using ICRP-74 flux-to-dose-rate conversion factors for I_h for the materials in Table 6.2, the spectra from Figure 6.3, and irradiation and decay times sweeping over the interval 10^1 – 10^9 s.

	η					
	first wall		shield		vacuum vessel	
Material	min	max	min	max	min	max
Beryllium	0.99	1.77	0.99	1.75	1.00	1.00
Concrete	1.00	16.0	1.00	4.77	1.00	1.00
Copper	0.95	1.03	0.94	1.01	1.00	1.00
CUCRZR-IG	0.99	1.09	0.99	1.18	1.00	1.00
NiAl Bronze	0.99	1.30	0.99	1.43	1.00	1.00
SS304	0.93	1.21	1.00	1.15	1.00	1.00
SS304B4	0.88	1.23	1.00	1.07	1.00	1.00
SS304B7	0.88	1.23	1.00	1.07	1.00	1.00
SS304L	0.93	1.21	1.00	1.15	1.00	1.00
SS304LN	0.96	1.20	1.00	1.08	1.00	1.00
SS304/304L	0.95	1.20	1.00	1.08	1.00	1.00
SS316L M106	1.00	1.38	0.97	1.44	1.00	1.00
SS316L M108	0.99	1.26	0.98	1.21	1.00	1.00
SS316L M111	0.97	1.22	1.00	1.08	1.00	1.00
SS316LN	0.97	1.22	1.00	1.08	1.00	1.00
SS316L(N)-IG M100	0.89	1.23	1.00	1.15	1.00	1.00
SS316L(N)-IG M101	0.89	1.23	1.00	1.15	1.00	1.00
SS430	0.88	1.23	1.00	1.07	1.00	1.00
Steel 660	0.99	1.30	0.99	1.21	1.00	1.00
Tungsten	0.31	1.94	0.26	1.21	1.00	1.00
Water	1.00	1.00	1.00	1.00	1.00	1.00
XM-19	0.89	1.20	1.00	1.13	1.00	1.00

6.5 Evaluation of η for FENDL-3.0 Nuclides

Though the CLITE model provides a survey of materials important to FES analysis, it is not comprehensive. For this reason, the analysis performed in Section 6.3, where η was calculated over a sweep of 30 irradiation and decay times from 10^0 s and 10^9 s (~ 31.7 years), was repeated for all 180 nuclides in the FENDL-3.0 nuclear data library. This was done using the shield neutron spectrum from Figure 6.3. This spectrum was chosen because most nuclides are unlikely to be exposed to a first wall spectrum, and the vacuum vessel spectrum is not

intense enough to provide significant SNILB criteria violations (as seen in Table 6.3).

The minimum and maximum η values for this sweep of irradiation and decay times were ascertained for each nuclide. For brevity, only nuclides with minimum or maximum η values that were 30% from 1 are shown in Table 6.11. Some nuclides appear in this table twice because they have both minimums less than 0.7 and maximums greater than 1.3. As discussed in Section 6.3, more severe SNILB violations generally occur at long irradiation and decay times. For this reason, the minimum and maximum η values for a sweep of shorter irradiation and decay times are also tabulated in Table 6.12. For this table, the sweep entailed 15 irradiation and decay times between 1 s and 34.6 h.

From these tables, it is apparent that only a small number of nuclides violate the SNILB criteria in a manner that results in a significant overestimation of the photon emission density ("significant", here meaning $\eta > 1.3$). However, several of these nuclides (e.g., ^{23}Na, ^{181}Ta, isotopes of W) are relevant to FES analysis. A large fraction of nuclides violate the SNILB criteria in a manner that results in an η significantly less than 1; notably isotopes of Cr, Mn, Fe, and which are likely to be present in structural material. Many of these nuclides have η values that are 3–5 orders of magnitude less than 1, whereas no nuclide was observed to have an η greater than 2 orders of magnitude larger than 1. This indicates that underestimation is both more common and more severe, probably due to threshold reactions. Of the nuclides with η much less than 1, ^{183}W and ^{186}W are of the greatest concern, as they are major isotopes found in elemental tungsten.

These results show that although the bulk materials used in the CLITE model generally only produce minor SNILB violations, this is not true of all nuclides. Because of this, in combination with the large number of dimensions that affect η, it is recommended that η or η_I be calculated for any bulk material prior to using the GT-CADIS method. This will predict if the GT-CADIS method will be effective, or if SNILB-violation methods must be employed.

Table 6.11: Minimum and maximum η values for all nuclides in the FENDL-3.0 data library for a sweep of irradiation and decay times ranging from 10^0 s to 10^9 s (~ 31.7 years).

η violation	nuclides
$0 < \eta < 10^{-5}$	^{36}S, ^{38}Ar, ^{40}K, ^{62}Ni, ^{71}Ga, ^{81}Br, ^{155}Gd, ^{156}Gd, ^{157}Gd, ^{158}Gd, ^{160}Gd, ^{162}Er, ^{166}Er, ^{167}Er, ^{176}Lu, ^{176}Hf, ^{177}Hf, ^{182}W, ^{186}W
$10^{-5} < \eta < 10^{-4}$	^{40}Ar, ^{46}Ca, ^{48}Ti, ^{51}V, ^{64}Ni, ^{65}Cu, ^{96}Zr, ^{96}Mo, ^{130}Ba, ^{139}La, ^{183}W, ^{196}Pt
$10^{-4} < \eta < 10^{-3}$	^{54}Cr, ^{68}Zn, ^{74}Ge, ^{100}Mo, ^{138}Ba, ^{168}Er, ^{179}Hf, ^{187}Re
$10^{-3} < \eta < 0.01$	^{33}S, ^{55}Mn, ^{79}Br, ^{106}Cd, ^{113}Cd, ^{115}Sn, ^{127}I, ^{180}Hf, ^{184}W, ^{190}Pt, ^{232}Th, ^{235}U, ^{238}U
$0.01 < \eta < 0.1$	^{29}Si, ^{39}K, ^{57}Fe, ^{58}Fe, ^{69}Ga, ^{97}Mo, ^{107}Ag, ^{111}Cd, ^{112}Cd, ^{119}Sn, ^{122}Sn, ^{121}Sb, ^{123}Sb, ^{137}Ba, ^{138}La, ^{152}Gd, ^{154}Gd, ^{164}Er, ^{175}Lu, ^{174}Hf, ^{178}Hf, ^{204}Pb
$0.1 < \eta < 0.7$	^{34}S, ^{41}K, ^{43}Ca, ^{44}Ca, ^{50}V, ^{67}Zn, ^{73}Ge, ^{76}Ge, ^{93}Nb, ^{94}Mo, ^{98}Mo, ^{114}Cd, ^{117}Sn, ^{120}Sn, ^{135}Ba, ^{140}Ce, ^{170}Er, ^{181}Ta, ^{180}W, ^{195}Pt, ^{207}Pb, ^{209}Bi
$1.3 < \eta < 10$	^{23}Na, ^{103}Rh, ^{107}Ag, ^{109}Ag, ^{108}Cd, ^{110}Cd, ^{112}Sn, ^{133}Cs, ^{138}La, ^{152}Gd, ^{154}Gd, ^{162}Er, ^{175}Lu, ^{176}Lu, ^{174}Hf, ^{179}Hf, ^{181}Ta, ^{180}W, ^{182}W, ^{185}Re, ^{187}Re, ^{192}Pt, ^{197}Au, ^{238}U
$10 < \eta < 100$	^{112}Cd, ^{113}Cd, ^{114}Cd, ^{116}Sn, ^{178}Hf
$100 < \eta < \infty$	—

Table 6.12: Minimum and maximum η values for all nuclides in the FENDL-3.0 data library for a sweep of 30 irradiation and decay times ranging from 1 s to 32.6 d.

η violation	nuclides
$0 < \eta < 10^{-5}$	—
$10^{-5}\eta < 10^{-4}$	—
$10^{-4} < \eta < 10^{-3}$	—
$10^{-3} < \eta < 0.01$	^{113}Cd, ^{167}Er, ^{186}W
$0.01 < \eta < 0.1$	^{138}La, ^{157}Gd, ^{158}Gd, ^{164}Er, ^{177}Hf, ^{183}W, ^{235}U
$0.1 < \eta < 0.7$	^{170}Er, ^{175}Lu, ^{190}Pt
$1.3 < \eta < 10$	—
$10 < \eta < 100$	—
$100 < \eta < \infty$	—

6.6 Conclusion

In this chapter, the extent to which the SNILB criteria are met was assessed for typical materials, spectra, and irradiation scenarios encountered in FES analysis. It was found that in general, the SNILB criteria are reasonably met for most of the cases tested and SNILB violations are more severe with high fluence. The reaction pathways that resulted in significant SNILB violations were determined and these pathways were consistent with theoretical expectations. Namely, the mechanisms for the overestimation and underestimation of the photon emission density via superposition were consistent with those presented in Sections 4.1.4.1 and 4.1.4.2, respectively. It was confirmed through the calculation of η_I that these minor SNILB violations often occur for pathways that produce important photons for SDR analysis. Finally it was found that a large number of nuclides not considered in the analysis of CLITE materials can significantly violate the SNILB criteria. It was found that violations for which η is much less than one are both more common and several orders of magnitude more severe.

The fact that the SNILB criteria are generally met for the ITER CLITE materials with typical spectra and irradiation scenarios indicates that the SNILB solution for T should accurately represent the transmutation process. This suggests that T (as calculated via groupwise irradiations) could be used with the D1S method described Section 2.4.1. It is much more important that the SNILB criteria are met in order to use groupwise irradiations to calculate T for the D1S method because T will affect the final answer for the SDR. In contrast, using the GT-CADIS T for VR purposes will not affect the SDR, provided that the estimate of T is not so poor that there is significant undersampling of important phase space regions in the MC neutron transport calculation.

Though the results presented in this chapter are promising, due to the large number of dimensions that affect the SNILB criteria (i.e., nuclide composition, neutron spectrum, and irradiation scenario), it is recommended that η or η_I be calculated for materials prior to using the GT-CADIS method. The calculation of η and η_I are no more computationally

expensive than the calculation of T, so this additional step do not impose a significant burden. This step will be carried out in the ensuing chapters, which will demonstrate the GT-CADIS method and SNILB-violation methods.

Chapter 7

Performance of the GT-CADIS Method

For problems where the SNILB criteria are met, the GT-CADIS method yields the SNILB solution for T, thereby producing VR parameters that optimize neutron transport with respect to a photon SDR detector. In this chapter, this is demonstrated with a simple problem. In the problem, a 13.8–14.2 MeV neutron source irradiates a stainless steel block with an air cavity inside. The SDR is then measured in a detector within the cavity. The material and irradiation scenario are chosen so that η is close to 1 for a range of neutron spectra/intensities.

Neutron VR parameters were generated using the GT-CADIS and FW-CADIS method. MC neutron transport was carried out in analog, with GT-CADIS weight windows and source biasing, and with FW-CADIS weight windows and source biasing. Here, analog denotes MC transport with no VR except implicit capture. For each of the 3 methods, MC neutron transport was done with 9 different computer processor times, in order to get neutron flux distributions over a range of convergence extents. For each of the 9 processor times, 10 trials were conducted, and the SDR was calculated for each trial. This was done by first performing an activation calculation for each trial. The resulting photon emission density distribution for each trial was then combined with the adjoint photon flux distribution to calculate the SDR for each trial via Equation 2.8. This allowed for the standard deviation in the SDR to be calculated as a function of neutron transport processor time for each of the three methods. It is shown that GT-CADIS weight windows and source biasing parameters yield faster convergence rates than both FW-CADIS and analog neutron transport.

Table 7.1: Material composition for SS316L M106, used as the primary material in the demonstration problem.

element	mass %	element	mass %
Fe	64.0135	Ta	0.1500
Cr	17.5000	N	0.1100
Ni	11.5000	Nb	0.1000
Mo	2.2500	Ti	0.1000
Mn	2.0000	C	0.0300
Cu	1.0000	P	0.0300
Si	1.0000	S	0.0150
Co	0.2000	B	0.0018

7.1 Problem Description

For this problem, the geometry (shown in Figure 7.1) is a rectangular prism that is 240 cm $\times$ 240 cm $\times$ 350 cm. In the z-direction, the first 10 cm are occupied by air. From $z = 10$ to $z = 350$ is a block of SS316L M106 (a material discussed in Section 6.2). This material composition is listed in Table 7.1. Within the SS316L M106 block, there is an air duct that is U-shaped in the y-z plane, centered around z-axis at $x = 0$, $y = 0$, with the prongs facing in the negative z-direction. The prongs extend from $z = 150$ to $z = 310$ and have a cross section in the x-y plane that is 20 cm $\times$ 20 cm. In the y-direction, the prongs are spaced so that the bottom of the bottom prong is at $y = -80$ and the top of the top prong is at $y = 80$. The connector between the prongs (which forms the "U") is also 20 cm $\times$ 20 cm in cross section. A CAD model of this geometry was created in CUBIT.

The neutron source occupies the entire x-y plane from $z = 0$ to $z = 5$. The source only has intensity in the 13.8 – 14.2 MeV energy group. The source intensity varies as a function of y-position: it linearly increases by an order of magnitude from $y = -120$ to $y = 120$. The neutron source is normalized such that the total neutron source intensity is $1.25 \cdot 10^{19}$ n/s.

The goal of the problem is to obtain the SDR in a detector in the duct after a single-pulse irradiation scenario consisting of 10^5 s (27.78 h) of irradiation and 10^5 s (27.78 h) of decay. The detector is a 5 cm radius sphere with ICRP-74 flux-to-dose-rate conversion factors. The

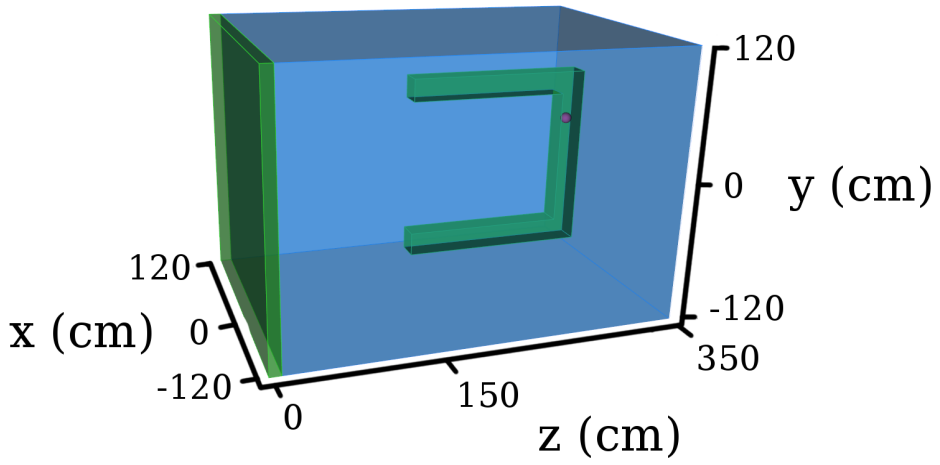

Figure 7.1: CAD geometry representation used for both MC and deterministic transport. The dosimeter was removed for both MC and deterministic neutron transport. Green: air; blue: SS316L M106; purple: dosimeter.

detector is located in the vertical part of the duct (i.e., the portion parallel to the y-axis) at $y = 35$. The material composition of the detector was chosen to be the same as the dosimeter in the FNG ITER benchmark problem (^{1}H: 52.34 a%, ^{12}C: 47.66 a%)[36]. The detector location can be seen in Figure 7.1. Since the detector is located near the top of the duct and the neutron source is most intense at the bottom of the geometry, the pathways of important neutrons are not known *a priori*, which makes this problem a good candidate for the application of automated VR.

For this problem, DAG-MCNP5 with FENDL-2.1 nuclear data was used for all MC transport. All deterministic transport was carried out with PARTISN using P_5S_{16}, FENDL-2.1 nuclear data, and the VITAMIN-J group structure (175 neutron groups, 42 photon groups). Activation was done with ALARA with FENDL/A-3.0 nuclear data.

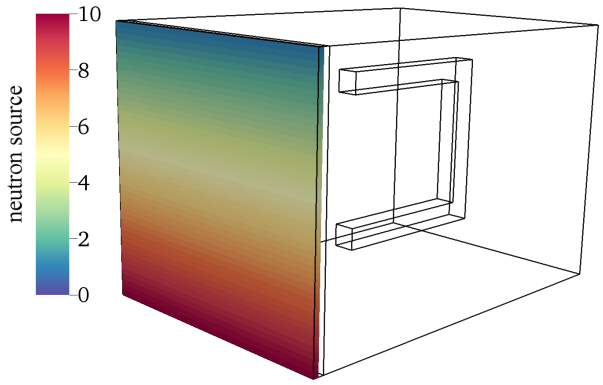

Figure 7.2: PDF of the neutron source distribution for the 13.8–14.2 MeV energy group. All other neutron groups have zero source intensity.

7.2 Generating GT-CADIS Weight Windows and Biased Source

In order to generate GT-CADIS weight windows and a biased source the following steps were carried out:

1. Deterministic adjoint photon transport,
2. Generation of the GT-CADIS adjoint neutron source,
3. Deterministic adjoint neutron transport,
4. Conversion of adjoint neutron fluxes to weight windows and a biased source.

These steps were carried out using the capabilities described in Chapter 5. For adjoint photon transport a PARTISN input file was created using the spherical detector as an isotropic adjoint source. A 42-group discretization of ICRP-74 flux-to-dose-rate conversion factors was used as the adjoint source spectrum, as shown in Figure 6.14. For adjoint photon transport — and the rest of this problem — a 48 × 48 × 70 mesh was used, resulting in 161,280 mesh volume elements, each 5 cm × 5 cm × 5 cm. The adjoint photon flux is shown in Figure 7.3.

Figure 7.3(a) shows that the photon importance in this energy group decreases by 2 orders of magnitude as it penetrates ~20 cm into the SS316L M106. The importance of the prongs of the duct is much greater than the surrounding material, indicating the importance of

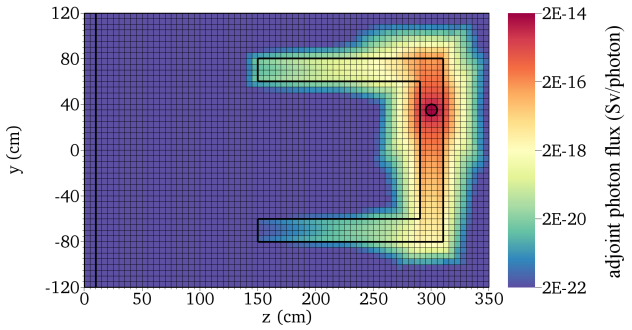

(a) Spatial distribution, $\mathfrak{x} = 0$, 0.8 –1.0 MeV

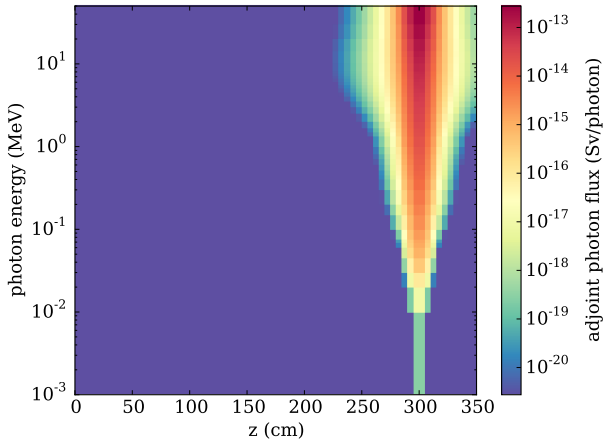

(b) Energy spectrum along the mesh row in Figure 7.4

Figure 7.3: GT-CADIS adjoint photon flux distribution.

streaming. The importance in the top prong is approximately 2 orders of magnitude larger than the bottom prong due to the position of the detector. Figure 7.3(b) shows how the adjoint photon spectra changes as a function of position. The abscissa of this plot represents the z position with the mesh row shown in Figure 7.4. This plot shows that the importance of low-energy photons drops off even closer to the detector than the 0.8 –1.0 MeV photons shown in Figure 7.3(a). This is due to both the reduced intensity of the adjoint photon source (i.e., the ICRP-74 flux-to-dose-rate conversion factors) for low energies and also the smaller mean free paths of low-energy photons.

Once the adjoint photon fluxes were obtained, an adjoint neutron source distribution was calculated using Equation 4.1. This equation requires T for each material in the problem. In Figure 6.12 is it shown that for SS316 M106 with an irradiation time of 10^5 s and a decay

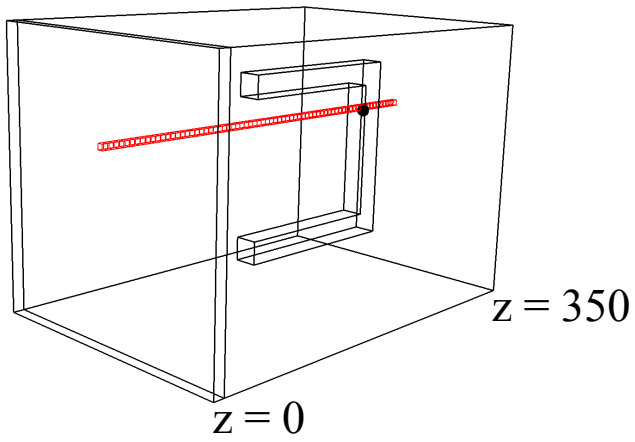

Figure 7.4: Mesh row selected for analyzing neutron and photon energy spectra as a function of z position.

time of 10^5 s, η is near 1.0 for the characteristic spectra for Figure 6.3. Plots of η for air were also created and no nontrivial deviation from 1.0 was observed for any of the characteristic spectra. Since $\eta \sim 1$ for both materials at the irradiation and decay scenario of interest, as long as the neutron spectra in this problem is less intense than the characteristic first wall spectrum in Figure 6.3, the SNILB criteria will be met. A forward neutron flux distribution is shown in Figure 7.5. This figure shows that this is indeed the case for majority of the geometry. On the source side of the geometry, where the neutron flux is most intense, minor SNILB violations may be present, but due to the extremely low adjoint photon flux in this region, this is unlikely to have any measurable impact on the performance of the resulting VR parameters.

T was calculated using the GT-CADIS method for SS316L M106 and air using the capabilities described in Section 5.3. This was done with $1.75 \cdot 10^{14}$ cm^{-2} s^{-1} fluxes within each neutron energy group individually for the 10^5 s irradiation and 10^5 s decay scenario. The choice of $1.75 \cdot 10^{14}$ cm^{-2} s^{-1} is not unique; as shown in Equation 3.28, T is independent of the neutron flux magnitude when the SNILB are met. In other words, any flux magnitude could be used, provided it is not so large that the SNILB criteria are violated. The choice of $1.75 \cdot 14^{12}$ cm^{-2} s^{-1} is large enough that important reaction channels will be populated, but still within the range of the characteristic spectra in Figure 6.3 (all of which result in $\eta \approx 1$

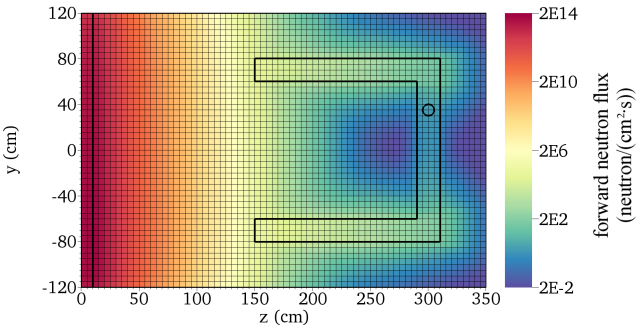

(a) Spatial distribution, $\mathtt{x} = 0$, 12.5 – 12.8 MeV

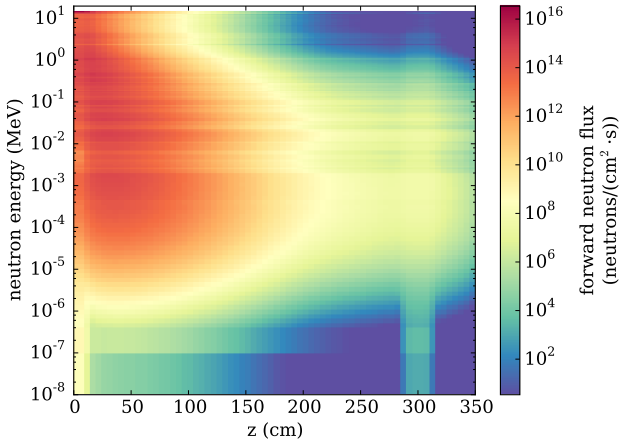

(b) Energy spectrum along the mesh row in Figure 7.4

Figure 7.5: Forward neutron flux distribution.

in this case).

The calculated T for SS316L M106 is shown in Figure 7.6. In addition to being necessary for GT-CADIS, this plot of T has a useful physical interpretation. A unit flux of neutrons in neutron energy group $\mathtt{g}$ ($\frac{1}{\mathrm{cm}^2 \cdot \mathrm{s}}$) on the $\mathtt{x}$-axis of this plot should result in a photon emission density of $\mathtt{q}_{\mathtt{p},\mathtt{h}}$ cm^{-3} s^{-1}, on the $\mathtt{y}$-axis of the plot after an 10^5 s irradiation and 10^5 s decay. The value of $\mathtt{q}_{\mathtt{p},\mathtt{h}}$ is indicted by the color bar. This interpretation is only valid when the SNILB criteria are met.

The shape of the plot of T in Figure 7.6 indicates that for SS316L M106, neutrons of every energy group can result in photon emissions and that a wide range of photon energies are represented. The horizontal patterns on the plot come from the fact that photons are emitted from activation products in discrete lines. The vertical line patterns reflect the neutron

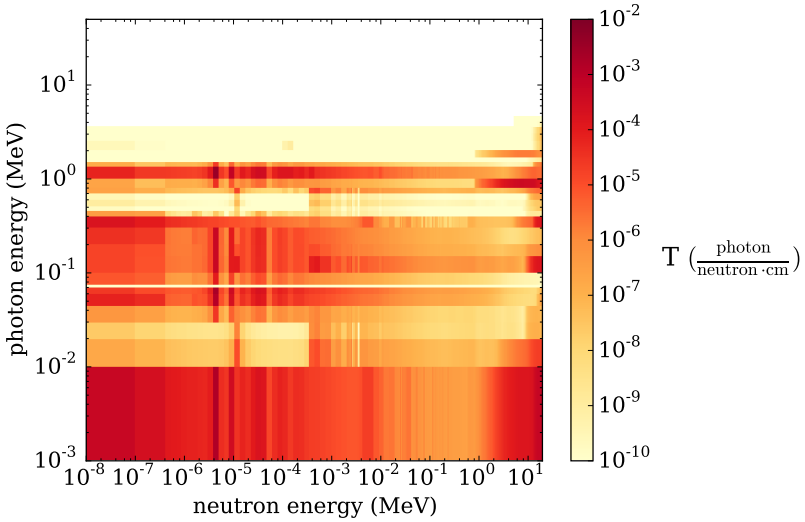

Figure 7.6: T for SS316L M106 with 10^5 s of irradiation and 10^5 s of decay.

energies that have high reaction cross sections for nuclides within SS136L M106. The T for air was also calculated, and found to be 0 for all neutron/photon energy group combinations; air does not produce any photons with the irradiation and decay scenario of interest.

Using the aforementioned method, the GT-CADIS adjoint neutron source distribution was obtained. A plot of the adjoint neutron source distribution for the 12.5 – 12.8 MeV energy group is shown in Figure 7.7(a). As expected, the shape of the adjoint neutron source is similar to the adjoint photon flux Figure 7.3(a) with the notable exception that the intensity is zero within the duct, as this volume contains air for which $\mathsf{T}_{g,h} = 0$ for all g and h. The spectral distribution shown in Figure 7.7(b) shows that the shape of T is carried over to the adjoint neutron source. For example, the elevated T at a neutron energy of ~4 eV as seen in Figure 7.6 dramatically increases the adjoint neutron source at ~4 eV.

Adjoint neutron transport was then done using this adjoint neutron source. The resulting adjoint neutron flux distribution for the 12.5 – 12.8 MeV energy group is shown in Figure 7.8(a). This plot represents the importance of neutrons to the photon SDR. The elevated adjoint neutron flux above a neutron energy of ~4 eV seen in Figure 7.8(b) comes from the elevated adjoint neutron source intensity at ~4 eV, bearing in mind that for adjoint particles, scattering is transposed so particles primarily scatter up in energy. The adjoint neutron flux

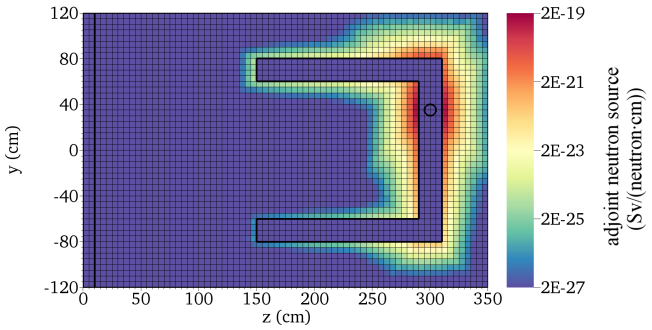

(a) Spatial distribution, $\mathrm{x} = 0$, 12.5 – 12.8 MeV

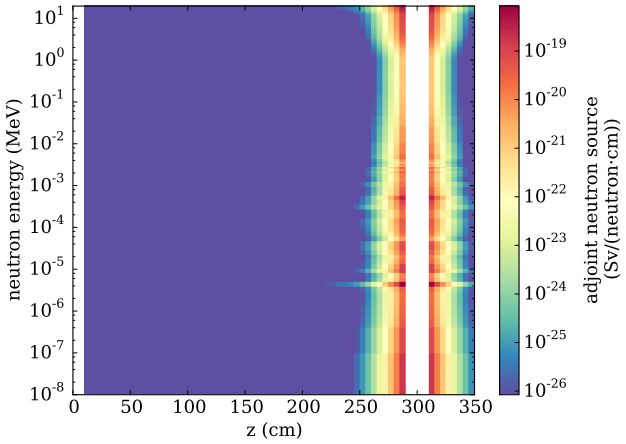

(b) Energy spectrum along the mesh row in Figure 7.4

Figure 7.7: The adjoint neutron source distribution calculated via the GT-CADIS method.

distribution is then used to calculate the weight window distribution and the biased source distribution using Equations 2.17 and 2.18 respectively.

The neutron weight window distribution for the 12.5 – 12.8 MeV energy group is shown in Figure 7.9(a) with the spectral distribution shown in Figure 7.9(b). As expected, the shape of these plots mirrors those of Figure 7.8. The biased source density distribution for the 13.8 – 14.2 MeV energy group (the only neutron group with nonzero intensity) is shown in Figure 7.10. This figure, which has a linear color scale, shows that a large amount of the area covered by the source is important, concentrated around the area that lines up with the top duct. This suggests that particles born anywhere have a nontrivial likelihood of traveling (likely scattering) into an important region of phase space.

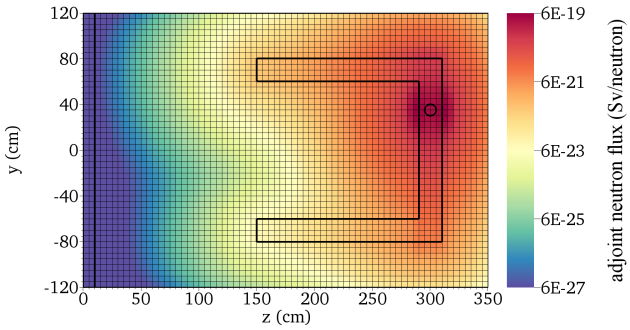

(a) Spatial distribution, $x = 0$, 12.5–12.8 MeV

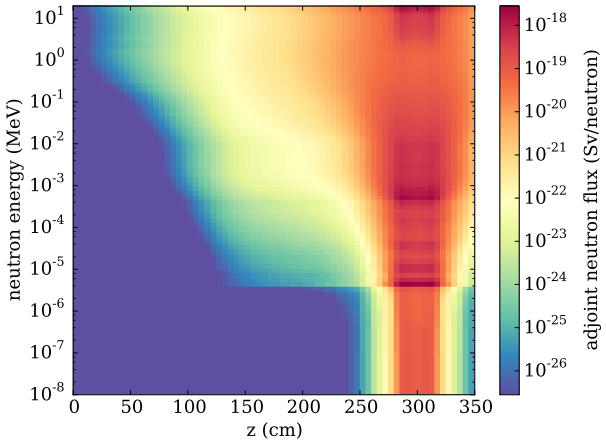

(b) Energy spectrum along the mesh row in Figure 7.4

Figure 7.8: The adjoint neutron flux distribution resulting from deterministic adjoint neutron transport using the GT-CADIS adjoint neutron source.

The adjoint neutron flux shown in Figure 7.8, combined with the forward neutron flux shown in Figure 7.5 enable the calculation of the neutron contributon flux as expressed in Equation 2.9. This quantity represents the paths that neutrons take in order to cause activation that produces important photons. This interpretation is only valid when the SNILB criteria are met because T is implicitly used to represent the activation process. The spatial distribution of the total contribution flux (i.e., the summation over all energy groups) is shown in Figure 7.11. In this figure, a threshold is applied such that only contribution fluxes within two orders of magnitude of the maximum contributon flux are shown. This figure shows that the dominant pathway for contributing particles is particle birth near the upper center of the source region, followed by scattering into the upper duct. This pathway is

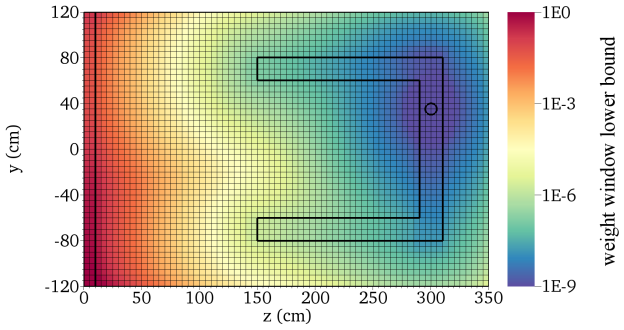

(a) Spatial distribution, $\mathrm{x} = 0$, 12.5–12.8 MeV

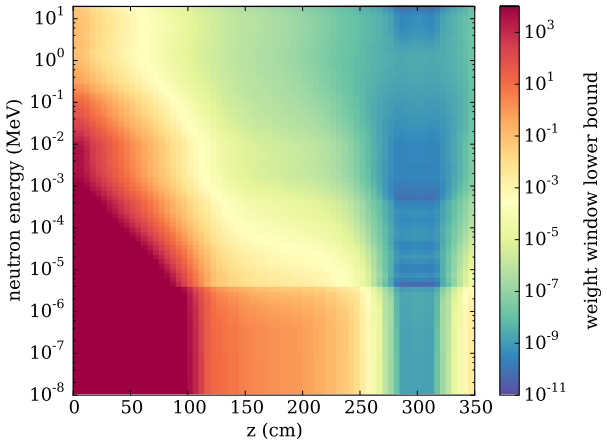

(b) Energy spectrum along the mesh row in Figure 7.4

Figure 7.9: Neutron weight window distribution calculated via the GT-CADIS method.

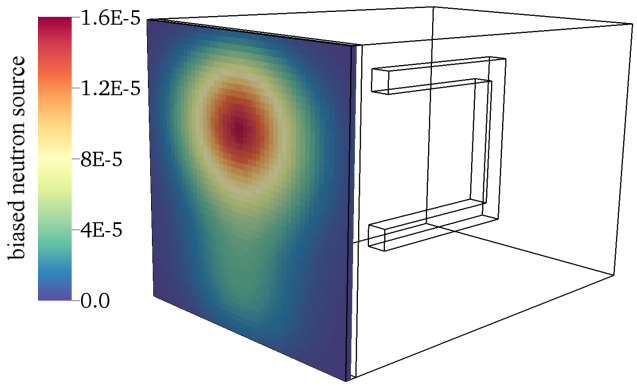

Figure 7.10: Biased neutron source as calculated with the GT-CADIS method for the 13.8 – 14.2 MeV energy group.

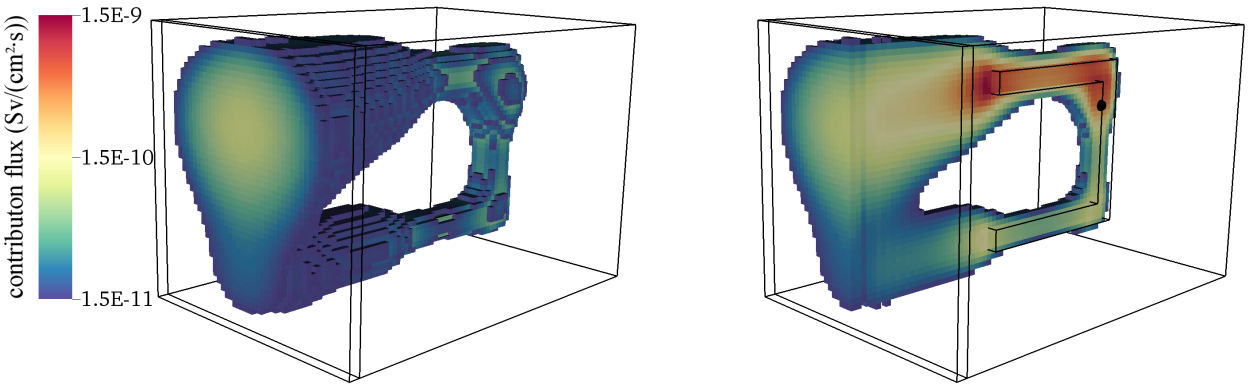

(a) Full distribution.

(b) Clip, $x = 0$.

Figure 7.11: Total (over all energy groups) neutron contributon flux distribution. A threshold has been applied so that any values less than $1.5 \cdot 10^{-11}$ Sv/(cm^2 s) (the minimum on the color scale) are not shown.

about an order of magnitude more likely than the corresponding pathway through the lower duct.

The energy spectrum of the contributon flux in shown in Figure 7.12. This figure shows how neutrons downscatter from the 13.8 – 14.2 MeV energy group to the dominant scoring energies in the 10^{-4}–10^{-1} MeV energy range. The contributon intensity is lower at $z = 225$ cm than at $z = 150$ cm or $z = 300$ cm. This is because the mesh row used for this figure (shown in Figure 7.4) is near the upper duct where the contributon flux is highest due to particle streaming. Particles that pass through the mesh row at $z = 150$ cm may still scatter into the upper duct and particles that reach $z = 300$ cm on the mesh row may have scattered out of the duct. However, particles that pass through mesh row at $z = 225$ cm on average cover less distance in the duct, so the contributon flux is lower.

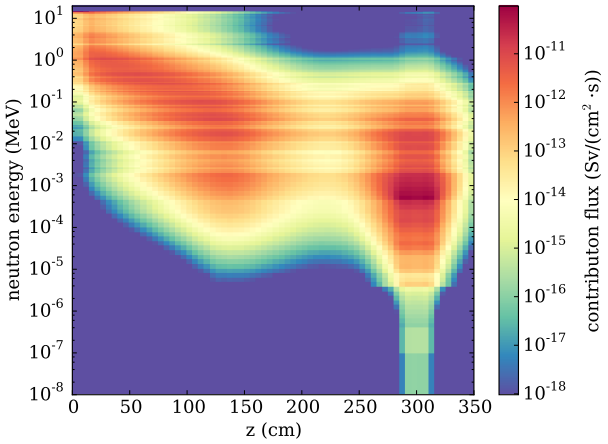

Figure 7.12: Contributon flux energy spectra along the mesh row in Figure 7.4.

7.3 Generating FW-CADIS Weight Windows and Biased Source

VR parameters were also generated using the FW-CADIS method, using the same 48 × 48 × 70 Cartesian mesh used for GT-CADIS. An FW-CADIS adjoint neutron source was calculated using the forward flux from Figure 7.5 and Equation 2.20. Equation 2.20 defines an adjoint source that provides equal weighting to all regions of phase space. The adjoint neutron source for the 12.5–12.8 MeV energy group is shown in Figure 7.13(a).

The shape of the spatial distribution in Figure 7.13(a) can be compared directly to the shape of the adjoint neutron flux distribution calculated via the GT-CADIS method as shown in Figure 7.7(a); for both plots the color scale spans 8 orders of magnitude. In contrast to the GT-CADIS distribution where the most intense adjoint neutron source surrounds the detector, in the FW-CADIS distribution the regions of highest adjoint neutron source are regions of lowest forward flux: the back portions of the geometry and the region between the prongs of the duct. In energy space, the FW-CADIS method assigns the most intense adjoint neutron source to the highest and lowest neutron energy groups in the back of the geometry seen in Figure 7.13(b), which differs greatly from the GT-CADIS distribution in Figure 7.7(b), where all energy groups are nearly equally represented in the region surrounding the detector.

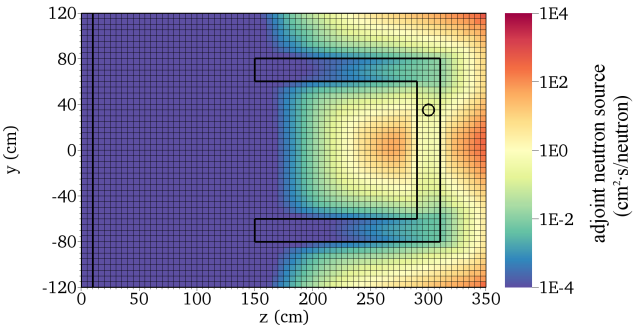

(a) Spatial distribution, $\chi = 0$, 12.5 –12.8 MeV

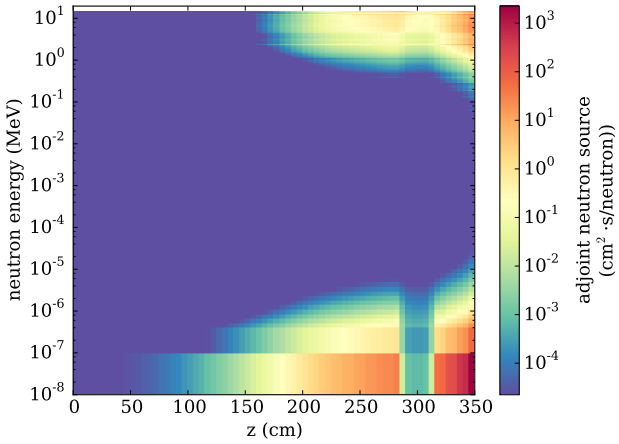

(b) Energy spectrum along the mesh row in Figure 7.4

Figure 7.13: Adjoint neutron source distribution calculated via the FW-CADIS method.

Using the adjoint neutron source in Figure 7.13 adjoint neutron transport was carried out. The resulting neutron flux distribution is shown in Figure 7.14. From this adjoint neutron flux distribution weight windows and a biased source were generated, as shown in Figures 7.15 and 7.16 respectively. As expected the shape of the weight window distribution both spatially and spectrally is the inverse of the adjoint neutron flux distribution. The biased source has increased source density in the regions aligning with the top and bottom duct prongs. Unlike the GT-CADIS biased source distribution, in this distribution the biased source density is higher in the region aligned with the bottom prong than the region aligned with the top prong. The weight windows produced from the FW-CADIS will strongly bias neutrons toward the back portion of the geometry. Though these weight windows are not expected to be optimal, they are expected to improve the efficiency of neutron transport

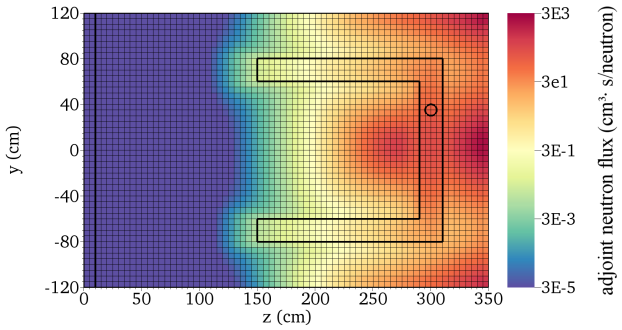

(a) Spatial distribution, $\varkappa = 0$, 12.5 – 12.8 MeV

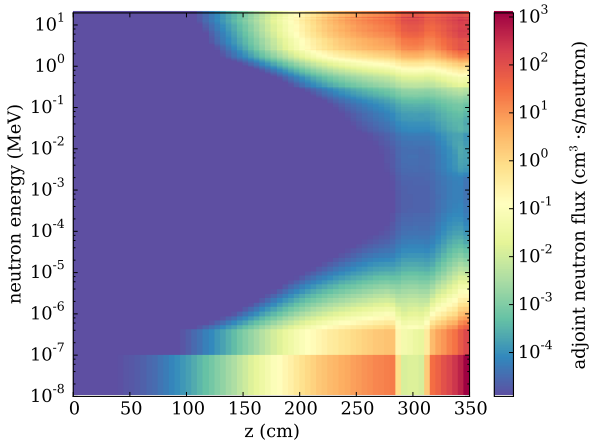

(b) Energy spectrum along the mesh row in Figure 7.4

Figure 7.14: Adjoint neutron flux distribution using the adjoint neutron source shown in Figure 7.13.

relative to analog neutron transport.

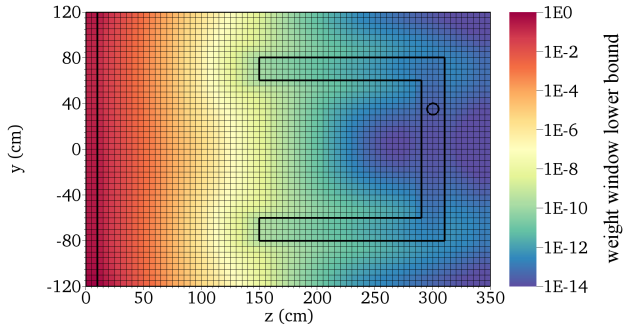

(a) Spatial distribution, $\mathrm{x} = 0$, 12.5 – 12.8 MeV

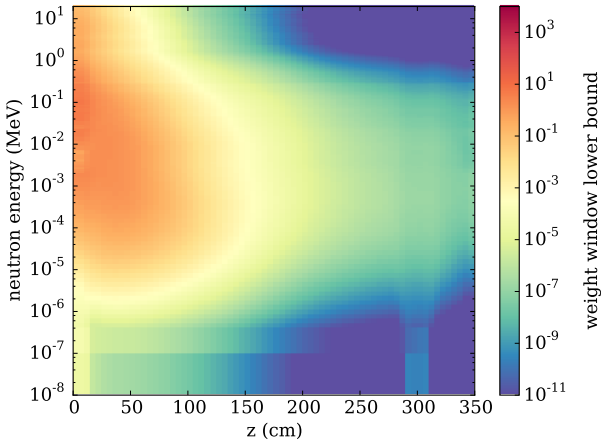

(b) Energy spectrum along the mesh row in Figure 7.4

Figure 7.15: Neutron weight window distribution calculated via the FW-CADIS method.

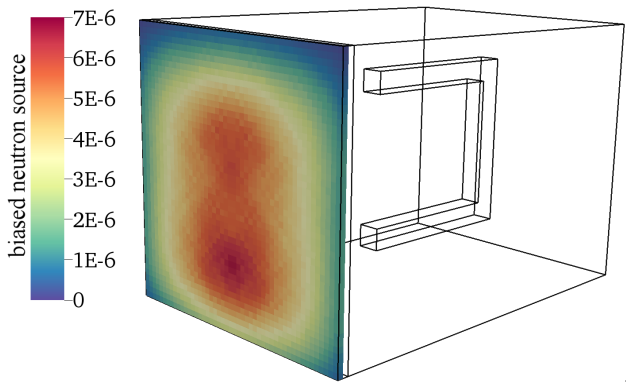

Figure 7.16: Biased neutron source as calculated with the FW-CADIS method for the 13.8 – 14.2 MeV energy group.

7.4 Neutron Transport and R2S

In order to assess the efficiency of neutron transport with GT-CADIS and FW-CADIS VR parameters and in analog, neutron transport was done over a range of processor times. Nine processor times were chosen, approximately logarithmically spaced between 10^1 min and 10^5 min. For each processor time, 10 neutron transport simulations were carried out for each of the three methods, each using different random number seeds to give statically independent results. For each of the resulting neutron flux distributions, an R2S calculation was done in order to obtain the SDR. This allowed for the relative error of the SDR as a function of processor time to be ascertained for each method, allowing for the calculation of the standard MC FOM.

All neutron transport was done on identical hardware with identical run configuration. Each trial was runs on 5 computer cluster nodes with 20 cores per node and 100 MPI processes. Each node was an Intel® Xeon® E5-2670 v2 CPU with a clock speed of 2.50 GHz and 128 GB of RAM. Each trial was run by specifying a number of particle (NPS) termination criterion in DAG-MCNP5 rather than a processor time (CTME) termination criterion to avoid complications with rendezvousing. For each processor time the required NPS was found via trial and error. Since the NPS was held constant for each trial within each target processor time, minor variations for the actual processor time required by each trial were observed. For each trial, the MCNP5 PRDMP card was used to limit simulations to a single rendezvous at the end of the run in order to mitigate load balancing effects.

Once neutron flux distributions were obtained for each of the 270 trials (10 trials $\times$ 9 processor times $\times$ 3 transport methods), PyNE R2S was used to generate ALARA input for each trial. ALARA was then run for the chosen irradiation and decay scenario yielding 270 photon source distributions. If MC photon transport were done for each of these distributions, the resulting SDRs would have statistical error from photon transport. In order to avoid this, the SDR was calculated for each of these distributions via Equation 2.8, using the adjoint photon flux from Figure 7.3 (which used the spherical detector as the adjoint source).

The resulting SDRs only have error from the MC neutron transport step and systematic discretization error from deterministic adjoint photon transport. Since the same deterministic adjoint photon flux is used for all trials, this latter component will not contribute to differences in convergence rates for the three methods.

7.5 Results

Neutron transport relative error distributions for each of the three methods for a subset of the processor times are shown in Figure 7.17. Only one of the ten trials for each processor time are represented in this figure. With analog neutron transport, the region where there are tally scores slowly propagates forward with increased processor time. With processor times less than ~1,000 minutes most of the mesh volume elements in the back of the geometry do not have a single tally score. This undersampling is expected to result in an underestimation of the SDR. In contrast, neutron transport using both FW-CADIS and GT-CADIS results in a tally scores in the back of the geometry with the first processor time. Using the GT-CADIS method, the relative error in the upper prong of the duct appears to decrease at a faster rate than the FW-CADIS method, as expected. Likewise, the FW-CADIS method results in low relative error throughout the entire geometry, whereas with the GT-CADIS method the back corners of the geometry have no tally scores even at the longest processor time.

Photon SDR results for each of the 270 trials are shown in Figure 7.18. The average SDRs for each of the 9 processor times are shown in Figure 7.19. In this latter plot, error bars represent the standard deviation in the estimated SDR from the 10 trials and also the standard deviation in the processor time from each of the 10 trials. With analog neutron transport, the SDR is underestimated by many trials at short processor times, which is consistent with the lack of tally scores in the back of the geometry as seen in Figure 7.17. For some of the trials, the SDR is greatly overestimated (off of the plot) due to low-probability streaming events that cause overestimations of the neutron flux in the back of the geometry,

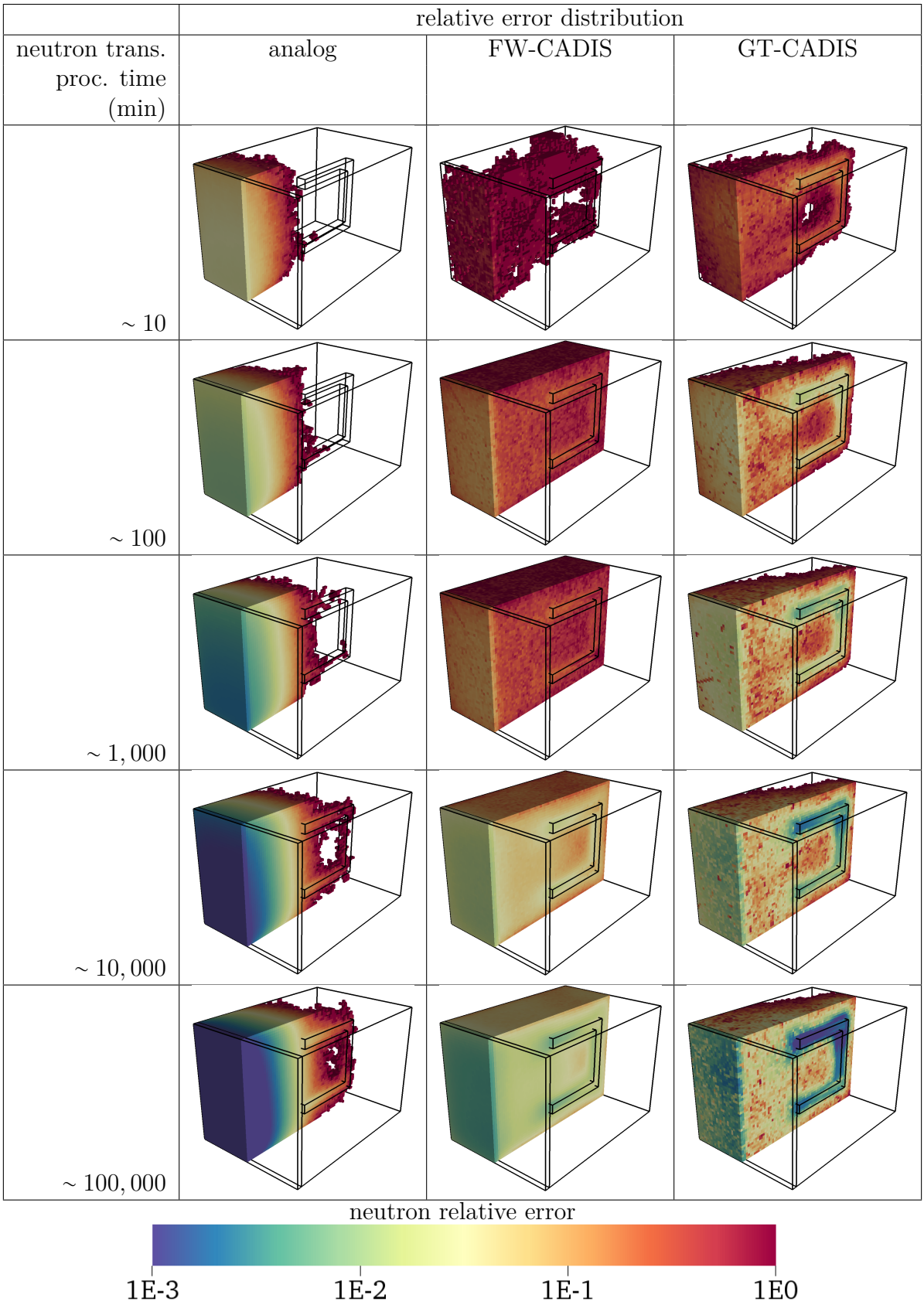

Figure 7.17: Neutron transport relative error distribution for analog, FW-CADIS, and GT-CADIS neutron transport. Each plot shows a clip on the y-z plane at $x = 0$. The wireframe geometry outline is not clipped.

yielding vary large standard deviations. For long processor times, the SDR estimates begin to converge.

For transport with FW-CADIS and GT-CADIS, results are within one standard deviation of the converged result for all processor times, suggesting that the effect of undersampling with short processor times is limited. The standard deviation of the GT-CADIS results is less than the standard deviation of the FW-CADIS results at all processor times, indicating that the GT-CADIS method is more effective.

To further quantify the efficacy of the GT-CADIS method the FOM was calculated at each processor time using Equation 2.13, as shown in Figure 7.20. The uncertainty in the processor time was propagated in order to obtain an error estimate for the FOM. The FOM should converge upon a constant value for a given method within a given simulation. For analog transport, it appears that the FOM is converging, however it is unlikely that is fully converged. Even with a processor time of 100,000 min, the relative error in the total neutron flux is still high, as seen in Figure 7.17. This suggests that many of the 175 neutron energy groups may not have a single score. This undersampling skews the estimate of FOM. As a result, the representative estimate of the FOM was chosen to be the average of the final three processor times and found to be $2.6 \pm 0.8 \cdot 10^{-3}$ min^{-1}.

For GT-CADIS and FW-CADIS, the FOM remains relatively constant across all processor times. After the 100 min processor time, tally scores were observed in all important regions of the problem. For this reason the representative FOM for GT-CADIS and FW-CADIS was chosen to be average of the FOM values for the processor times between 100–100,000 min. This yields FOMs of 200 ± 100 min^{-1} and 1.5 ± 0.7 min^{-1} for GT-CADIS and FW-CADIS respectively. Using these calculated FOMs, the speedup (the ratio of FOMs) was also calculated. The GT-CADIS method yields a speedup of $9 \pm 5 \cdot 10^4$ compared to analog and 200 ± 100 compared to FW-CADIS.

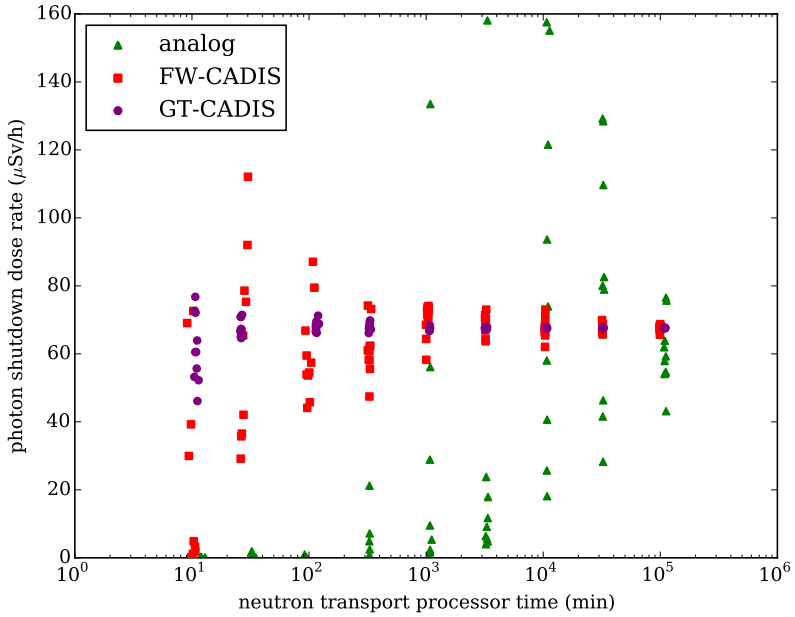

Figure 7.18: Photon SDR results from neutron transport over a range of computer processor times.

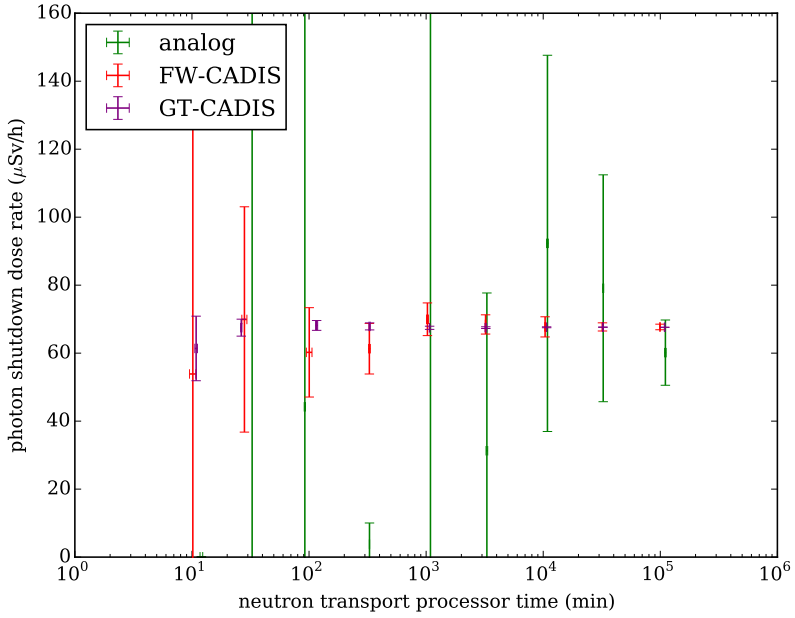

Figure 7.19: Average of the SDR results from Figure 7.18. Error bars show the standard deviation of the SDR and neutron transport processor time.

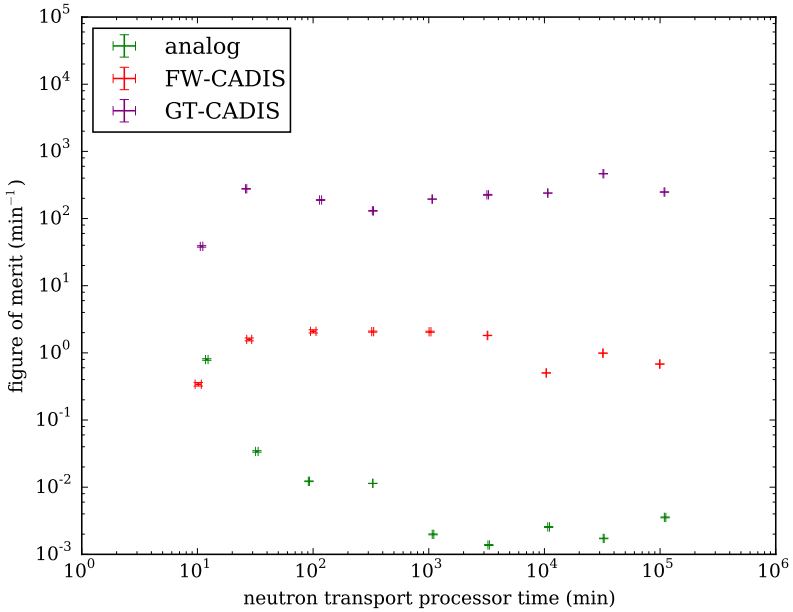

Figure 7.20: FOM as a function of neutron transport processor time.

7.6 Conclusion

In this chapter a simple problem where the SNILB criteria are met was constructed in order to quantify the performance of the GT-CADIS method relative to FW-CADIS and analog neutron transport. The shapes of the neutron weight windows and biased source distributions produced by the GT-CADIS method are consistent with expectations both in space and in energy. These VR parameters result in a much faster convergence of the neutron flux in important regions relative to FW-CADIS, as indicated by analysis of the relative error distributions as a function of processor time. The large speedups resulting from the use of the GT-CADIS method — $9 \pm 5 \cdot 10^4$ relative to analog transport and 200 ± 100 relative to FW-CADIS — indicate that the required computational resources for SDR analysis are drastically reduced by using the GT-CADIS method. This is a promising result, considering the evidence set forth in Chapter 6 that suggests that the SNILB criteria are generally met for typical FES scenarios, indicating a broad applicability of GT-CADIS. The GT-CADIS method will be demonstrated for one such FES scenario in Chapter 9.

Chapter 8

Performance of SNILB-Violation Methods

As discussed in Section 4.2, the efficacy the GT-CADIS method is not guaranteed when the SNILB criteria are violated. This can be predicted by calculating η and/or η_I for the materials, spectra, and irradiation scenarios of interest. In this chapter a problem is contrived where a significant portion of the SDR comes from a material for which η and η_I are extremely small, as a result of dominant photons being produced by a multiple-neutron-interaction pathway. This form of SNILB violation was chosen because in Chapter 6 it was shown that this mechanism can result in more severe SNILB violations. For the chosen problem, weight windows and biased sources are first produced via the GT-, GTS-, GTB-, and GTSB-CADIS methods. As in Chapter 7, neutron transport is carried out over a range of computer processor times using each set of VR parameters. For each trial, the SDR is calculated using the same procedure as in Chapter 7. The uncertainty in the SDR as a function of computer processor time is assessed in order to determine the efficacy of each method.

8.1 Problem Description

The geometry (shown in Figure 8.1) consists of a cube occupying the region -122.5 cm to 122.5 cm in x, -122.5 cm to 122.5 cm in y, and 0 cm to 245 cm in z. The first 10 cm in the z-direction are occupied by air. From z =10 cm to z =245 cm the geometry is a block of water with several features inside. A T-shaped air duct within the water is aligned parallel to the z-axis, centered around the origin. The duct has a 15 cm $\times$ 15 cm cross section and extends from 60 cm to 170 cm in z. The "cross" portion of the "T" extends from -7.5 cm to 7.5 cm in x, -32.5 cm to 32.5 cm in y, and 155 cm to 170 cm in z. Three 5 cm $\times$ 5 cm $\times$ 5 cm blocks are also inside the water block, centered at the points (0, 100, 162.5), (0, -100,

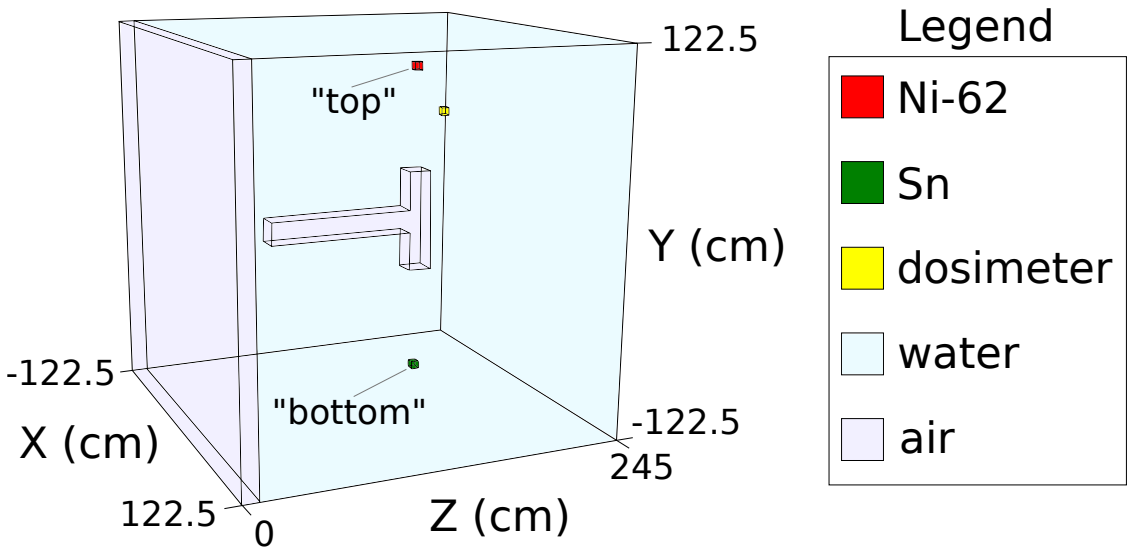

Figure 8.1: Geometry used for SNILB-violation methods experimentation.

162.5), and (0, 70, 182.5). The blocks consist of ^{62}Ni with a density of 1 g/cm^3, Sn (natural abundance) with a density of 1 g/cm^3, and a photon dosimeter. The dosimeter has the same composition as used in Chapter 7 and also uses ICRP-74 flux-to-dose-rate conversion factors. For convenience, the volumes containing ^{62}Ni and Sn are referred to as the "top" and "bottom" volumes, respectively. The mesh used for this problem is 49×49×49 (117,649 mesh volume elements) and conforms to all geometry features.

The neutron source for this problem occupies the region from $z = 0$ cm to $z = 5$ cm. The PDF describing this source is given by:

$$q = 1 + \sin\left(2\pi\sqrt{\left(\frac{x - 122.5}{245}\right)^2 + \left(\frac{y - 122.5}{245}\right)^2}\right). \tag{8.1}$$

The normalized version of this PDF is shown in Figure 8.2. A single-pulse irradiation scenario was chosen with 10^8 s (~ 3.17 y) of irradiation followed by 10^8 s (~ 3.17 y) of decay using a source normalizations of 10^{23} n/s. With this problem, only activation from ^{62}Ni and Sn is considered. This problem was chosen because it has important characteristics for experimentation with SNILB-violation methods, as discussed in the next section.

For this problem, DAG-MCNP5 with FENDL-2.1 nuclear data was used for all MC

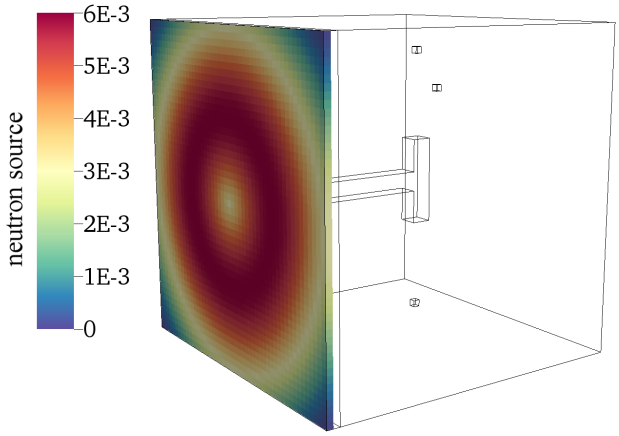

Figure 8.2: Normalized PDF of the neutron source density for SNILB-violation methods experimentation.

transport. All deterministic transport was carried out with PARTISN using P_5S_{16}, FENDL-2.1 nuclear data, and the VITAMIN-J group structure (175 neutron groups, 42 photon groups). Activation was done with ALARA with FENDL/A-3.0 nuclear data.

8.2 Problem Characteristics

The problem described in Section 8.1 was designed to have two important characteristics. First, the SDR resulting from the top and bottom volumes are nearly equal, which means that neutrons must be directed to both volumes in order to get the correct answer. Second, the bottom volume meets the SNILB criteria and the top volume violates the SNILB criteria due to a dominant multiple-neutron-interaction pathway (with $\eta << 1$). This means that the GT-CADIS method is not expected to recognize the importance of the top volume, thereby producing poor VR parameters. The procedure used to verify the properties of this problem are described in this section.

First, MC neutron transport was conducted in order to obtain *a priori* knowledge of the converged neutron flux. This was done using FW-CADIS in order to minimize the relative error in the top and bottom volume simultaneously; noting that this optimization is distinct from minimizing the relative error in only important phase space regions — the

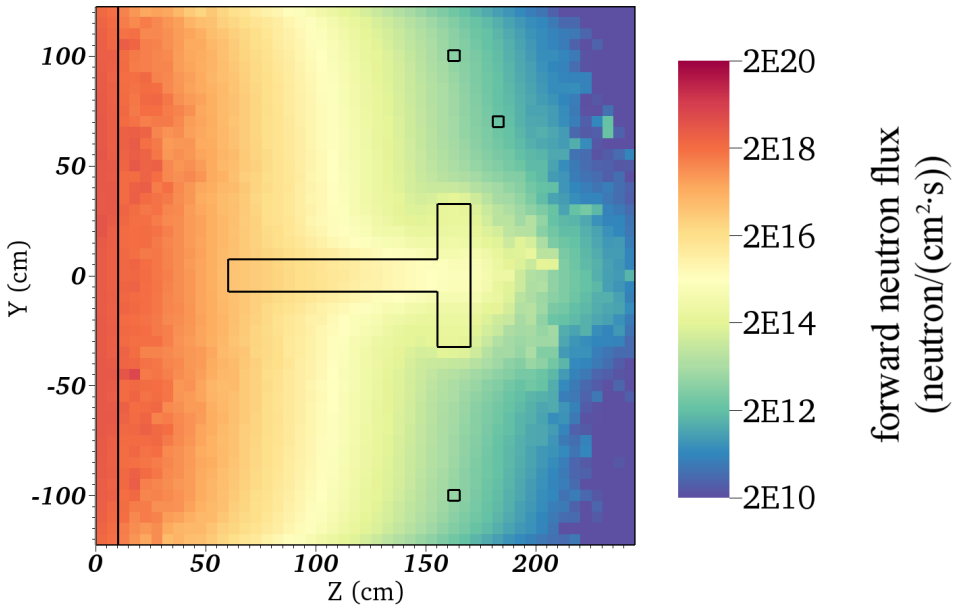

Figure 8.3: Total forward neutron flux at $x = 0$.

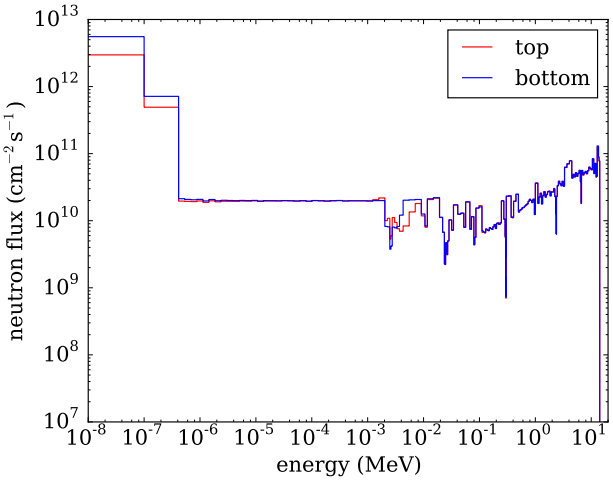

Figure 8.4: Forward neutron flux within the top and bottom volumes.

goal of GT-CADIS and SNILB-violation methods. This MC neutron transport resulted in a maximum groupwise relative error of 0.2% in the top volume and 0.21% in the bottom volume (for energy groups below the source energy), with many energy groups having a significantly lower relative error. The neutron flux distribution is shown in Figure 8.3 with the neutron spectra in the top and bottom volumes shown in Figure 8.4. The neutron flux in these two volumes is nearly identical, which indicates that the effects of self-shielding within these volumes (which have different cross sections) is minimal.

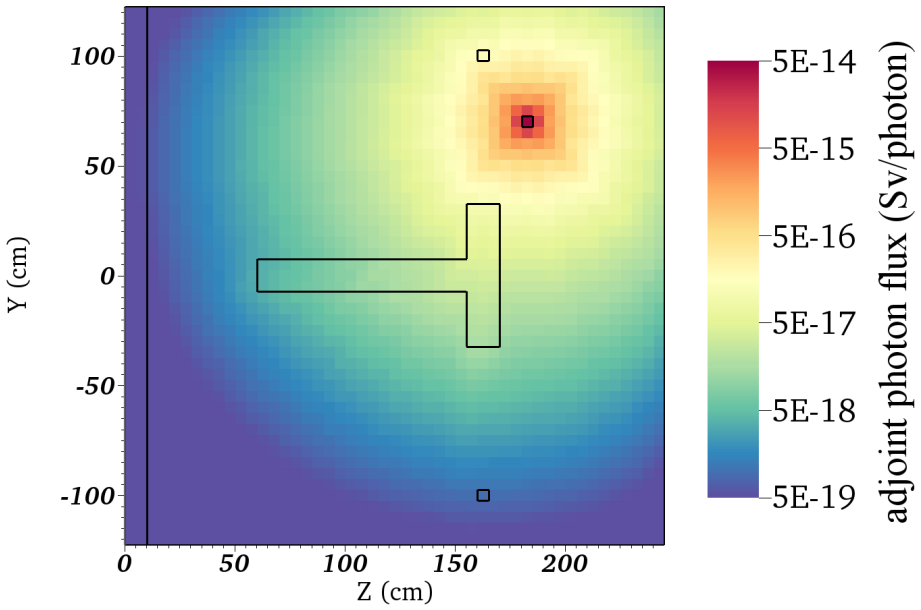

Figure 8.5: Adjoint photon flux for the 0.7 – 0.8 MeV energy group at $x = 0$.

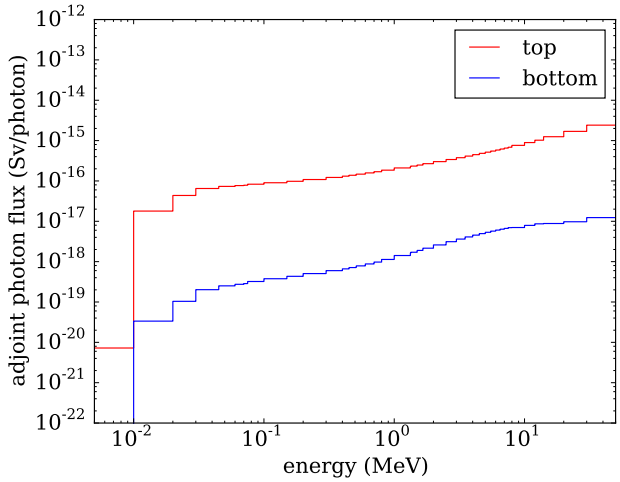

Figure 8.6: Adjoint photon flux within the top and bottom volumes.

Next, an adjoint photon transport calculation was performed using the detector as the adjoint source. The adjoint photon flux distribution for the 0.7 – 0.8 MeV energy group is shown in Figure 8.5. The photon spectrum in the top and bottom volumes is shown in Figure 8.6. The flux in the top volume is approximately three orders of magnitude higher than the bottom volume.

Using the MC neutron spectra in Figure 8.4, η and η_I were calculated for the top and bottom volumes. For η_I, two different functions for I_h were used: ICRP-74 flux-to-dose-rate

conversion factors, and the actual adjoint photon spectra shown in Figure 8.6. Activation was also done in the top and bottom volumes and the SDR was then calculated using the discrete form of Equation 2.8:

$$\mathsf{SDR} = \sum_{h} \phi^{+}_{p,h} q_{p,h}. \tag{8.2}$$

These values are summarized in Table 8.1. The SDR resulting from the two volumes are nearly equal. The SDRs are expected to be the actual converged SDRs because they result from the converged neutron flux and full transmutation calculations. The η and both η_I values are extremely small for the top volume and near 1 for the bottom volume, meaning this problem has the desired characteristics. Further analysis was performed for the activation of the top volume. It was found that 99.9994% of the SDR comes from ^{60}Co and that 99.15% of ^{60}Co is produced via the following two mechanisms:

$$\begin{array}{l} {}^{62}\underset{(1.0)}{\mathrm{Ni}} \xrightarrow{(n,\,\alpha)} {}^{59}\underset{(1.39\cdot10^{-6})}{\mathrm{Fe}} \xrightarrow{\beta^-} {}^{59}\underset{(1.32\cdot10^{-6})}{\mathrm{Co}} \xrightarrow{(n,\,\gamma)} {}^{60}\underset{(3.24\cdot10^{-9})}{\mathrm{Co}} \\ \qquad\qquad\qquad\qquad\qquad\qquad\qquad\qquad\quad \xrightarrow{(n,\,\gamma)} {}^{60m}\underset{(4.06\cdot10^{-9})}{\mathrm{Co}} \xrightarrow{IT} {}^{60}\underset{(4.05\cdot10^{-9})}{\mathrm{Co}} \end{array} \tag{8.3}$$

where values in parenthesis under nuclides denote number densities with respect to the parent nuclide. These mechanisms violate the SNILB criteria because each consists of two neutron interactions: first ^{62}Ni(n, α) ^{59}Fe then either ^{59}Co(n, γ) ^{60}Co or ^{59}Co(n, γ) ^{60m}Co. The cross sections for these reactions are shown in Figure 8.7. The first reaction is a threshold reaction, occurring only with fast neutrons. The second reactions are dominated by thermal neutrons. In other words, both fast and thermal neutrons must be present to produce appreciable amounts of ^{60}Co. This behavior cannot be captured with single-energy-group irradiations, as indicted by the low value of η and η_I, and therefore the standard GT-CADIS method is not expected to be effective for this problem.

Table 8.1: Problem characteristics. SDRs are calculated via Equation 8.2 using the neutron flux distribution in Figure 8.3 and the adjoint photon flux distribution in Figure 8.5. The η_I actual is calculated using the actual photon spectra in Figure 8.5 as I_h in Equation 3.33.

	^{62}Ni (top)	Sn (bottom)
converged SDR (Sv/s)	$9.45 \cdot 10^{-9}$	$9.19 \cdot 10^{-9}$
η	$6.69 \cdot 10^{-6}$	1.002
η_I ICRP-74	$1.98 \cdot 10^{-5}$	1.001
η_I actual	$6.31 \cdot 10^{-6}$	1.002

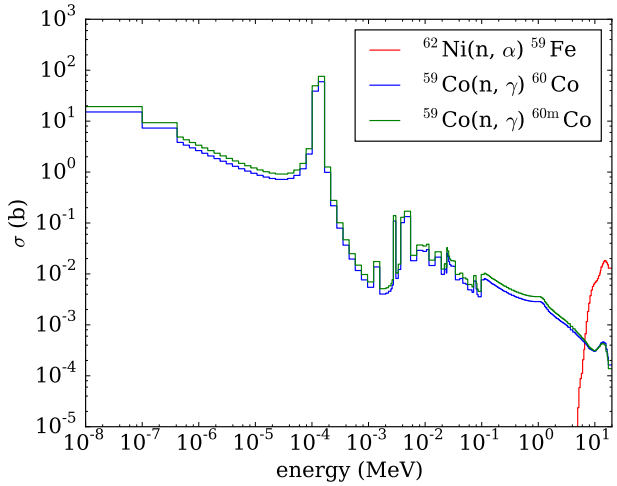

Figure 8.7: Cross sections for the neutron interactions shown in Equation 8.3 from FENDL-2.1.

8.3 Generating Weight Windows and Biased Sources

In order to generate weight windows and biased sources, T was calculated for the top volume with the GT-, GTS-, GTB-, and GTSB-CADIS methods using the computational tools described in Section 5.3. From the results in Table 8.1 it is clear the SNILB criteria are met in the bottom volume. For this reason, T was calculated once for the bottom volume using the GT-CADIS method. This bottom volume T was paired with a T from the top volume from each of the four methods to calculate adjoint neutron sources. Adjoint neutron sources were calculated using the adjoint photon flux distribution in Figure 8.5 via Equation 4.1. Since the converged neutron flux was already obtained (Figure 8.3), one method for assessing these adjoint neutron sources is by calculating the SDR via the discrete form of Equation 2.6:

$$SDR = \sum_{g} \phi_{n,g} q^{+}_{n,g}. \tag{8.4}$$

Comparing these values to the expected SDRs in Table 8.1 is a way of comparing how well T calculated by each method approximates the transmutation process, as these T determine the magnitude of the adjoint neutron source. Using adjoint neutron sources from each method, deterministic transport was carried out and weight windows and biased sources were calculated from the resulting adjoint neutron fluxes.

8.3.1 GT-CADIS

The GT-CADIS method was used to calculate the T in the top and bottom volumes using pulses of 10^7 cm^{-2} s^{-1}. These quantities are plotted in Figures 8.8 and 8.9, respectively. Figure 8.8 shows that in the top volume, single-energy-group irradiations using only the fastest neutron energy groups produce a weak photon emission density. In contrast, Figure 8.9 shows that single-energy-group irradiations result in much greater photon emission density in all neutron energy groups. The shapes of these T manifest themselves in the resulting adjoint neutron sources shown in Figure 8.10.

Using these adjoint neutron source spectra, SDRs were calculated via Equation 8.4. The SDR from the bottom volume is $9.22{\cdot}10^{-9}$ Sv/s: merely 1.003 times the expected value from Table 8.1; whereas the SDR from the top volume is $5.45{\cdot}10^{-14}$ Sv/s: $5.77{\cdot}10^{-6}$ times the expected value. These results are consistent with the η and η_I values given in Table 8.1. Since the adjoint neutron source for the top volume underestimates the SDR, the GT-CADIS method underestimates the importance of the top volume. The weight windows and biased sources resulting from these adjoint sources are shown in Figures 8.11 and 8.12, respectively. As expected, these figures show that neutrons are strongly biased toward the bottom volume and only weakly biased toward the top volume.

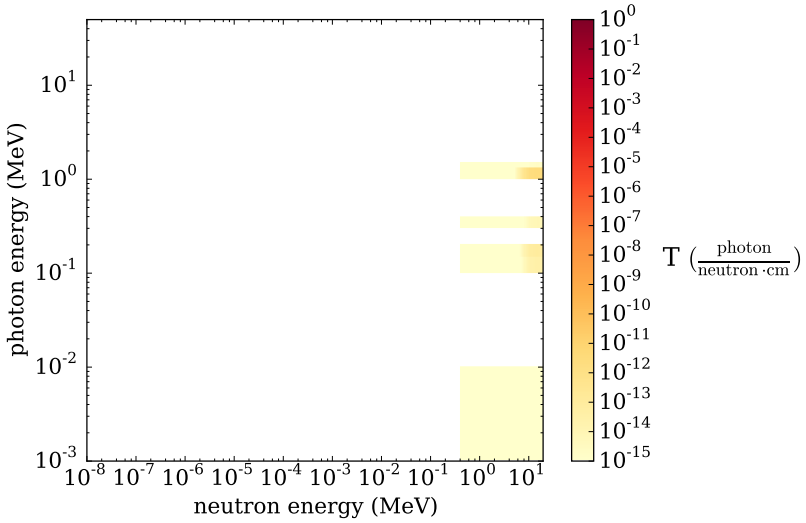

Figure 8.8: T for the top volume as calculated by the GT-CADIS method.

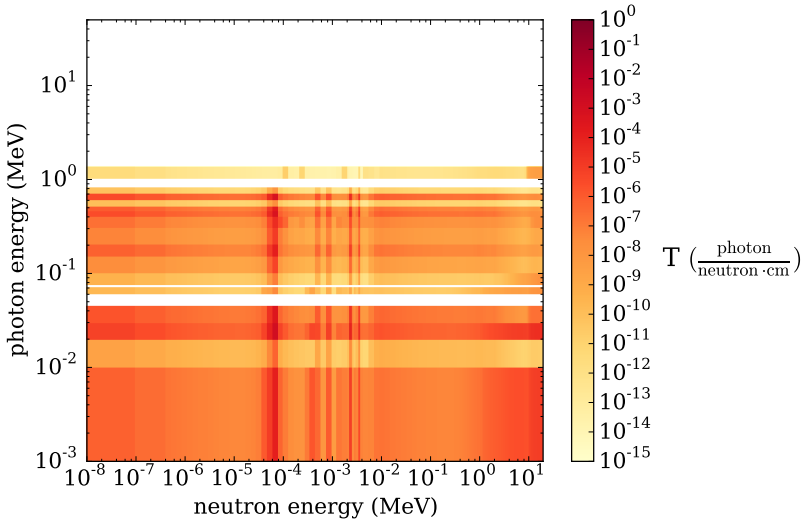

Figure 8.9: T for the bottom volume as calculated by the GT-CADIS method.

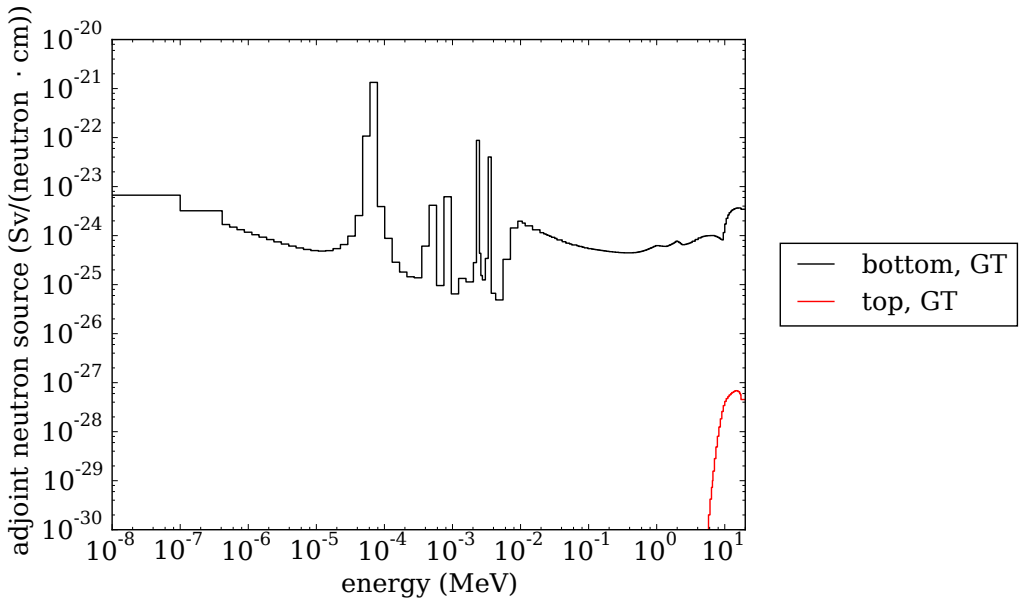

Figure 8.10: Adjoint neutron sources produced by the GT-CADIS method.

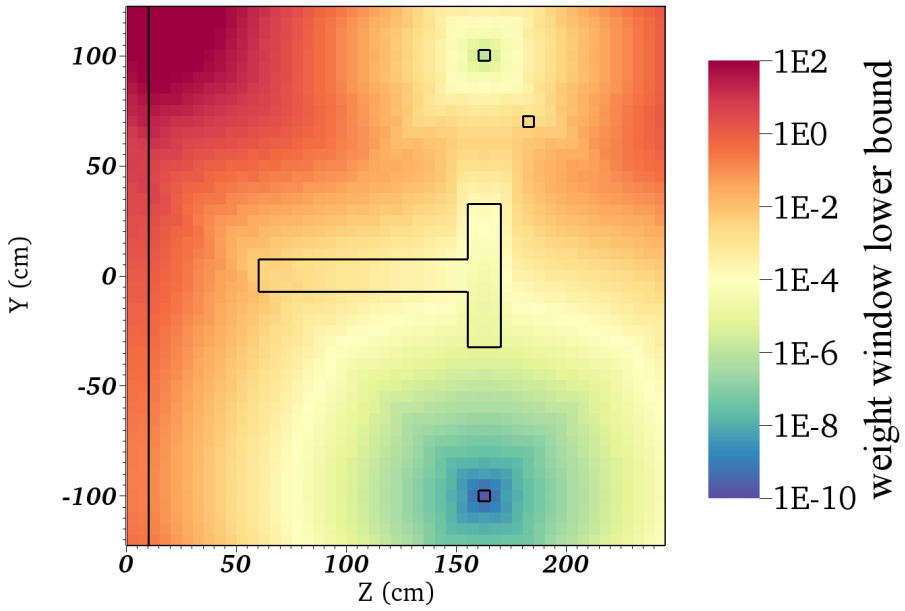

Figure 8.11: GT-CADIS weight window distribution for the 12.5 – 12.8 MeV energy group at $x = 0$.

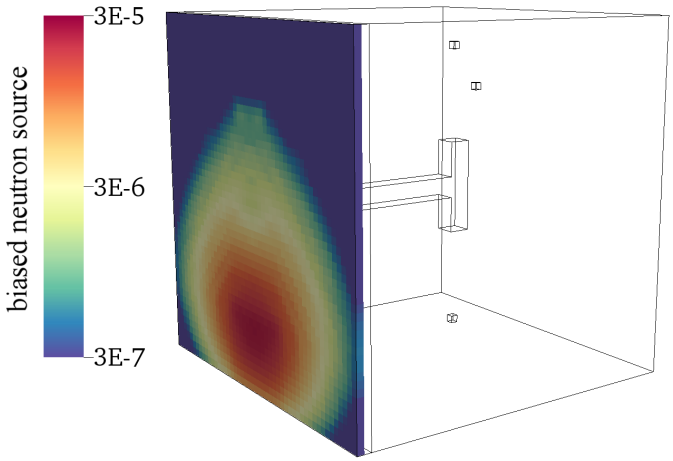

Figure 8.12: GT-CADIS biased source distribution for the 13.8 – 14.2 MeV energy group.

8.3.2 GTS-CADIS

The GTS-CADIS method as described in Section 4.2.1 uses a deterministic neutron transport calculation in order to obtain the neutron fluxes used to calculate T. For the purpose of this experiment, the neutron fluxes from MC neutron transport in Figure 8.3 were used. The T calculated via the GTS-CADIS method for the top volume is shown in Figure 8.13. This T is much larger in magnitude in the fast neutron region than T from GT-CADIS shown in Figure 8.8 as a result of the normalization process. The adjoint neutron source spectrum for the top volume using this T is shown in Figure 8.14. In this figure, an adjoint neutron source spectrum is also shown using an unnormalized T from GTS-CADIS — that is, T' from Equation 4.20. This figure also shows the GT-CADIS adjoint neutron source for the bottom volume for reference. Unlike the GT-CADIS adjoint neutron source for the top volume in Figure 8.10, the GTS-CADIS adjoint neutron sources go to zero for energies higher than the 13.8 – 14.2 MeV energy group because the forward neutron flux is zero for all energy groups above the source energy. With the unnormalized adjoint neutron source the SDR via Equation is 8.4 is a factor of $6.31 \cdot 10^{-6}$ of the expected value in Table 8.1. With normalization, this SDR is equivalent to the expected value.

The weight window distribution for the 12.5 – 12.8 MeV energy group is shown in Figure 8.15 and the biased source for the source energy group (13.8 – 14.2 MeV), is shown in Figure

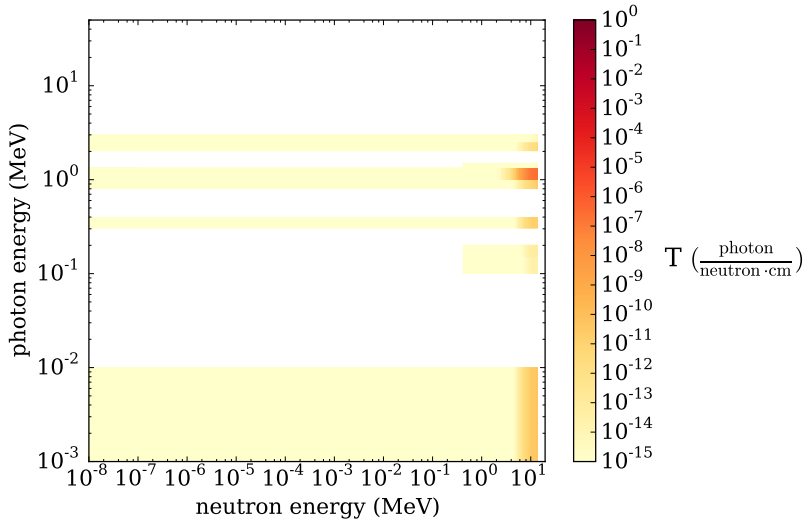

Figure 8.13: T for the top volume as calculated by the GTS-CADIS method with and without normalization.

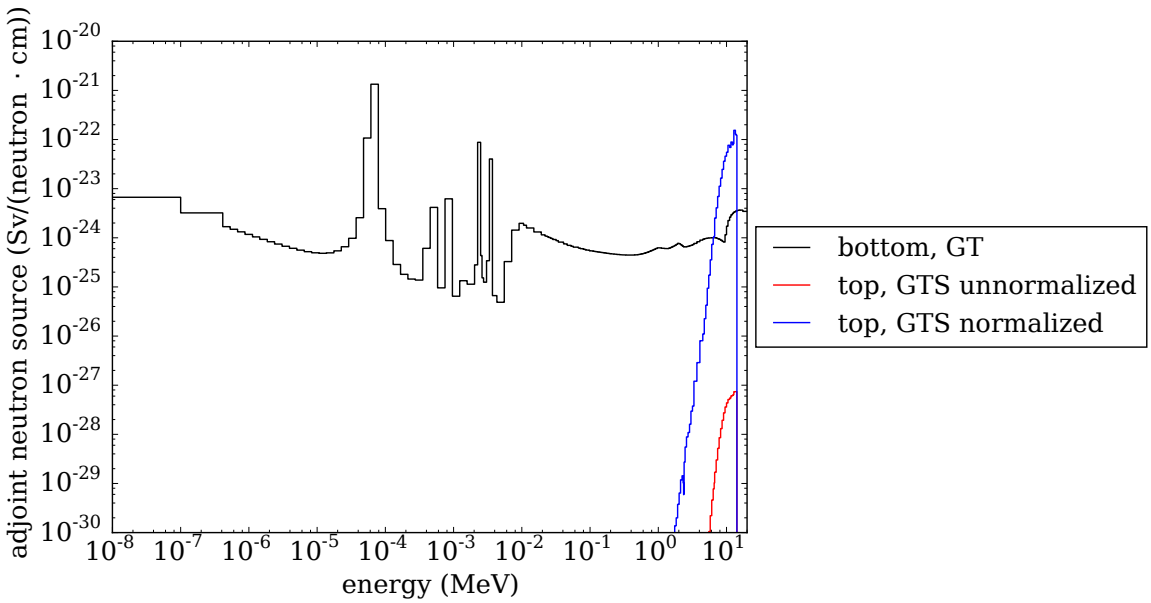

Figure 8.14: Adjoint neutron sources produced by the GTS-CADIS method.

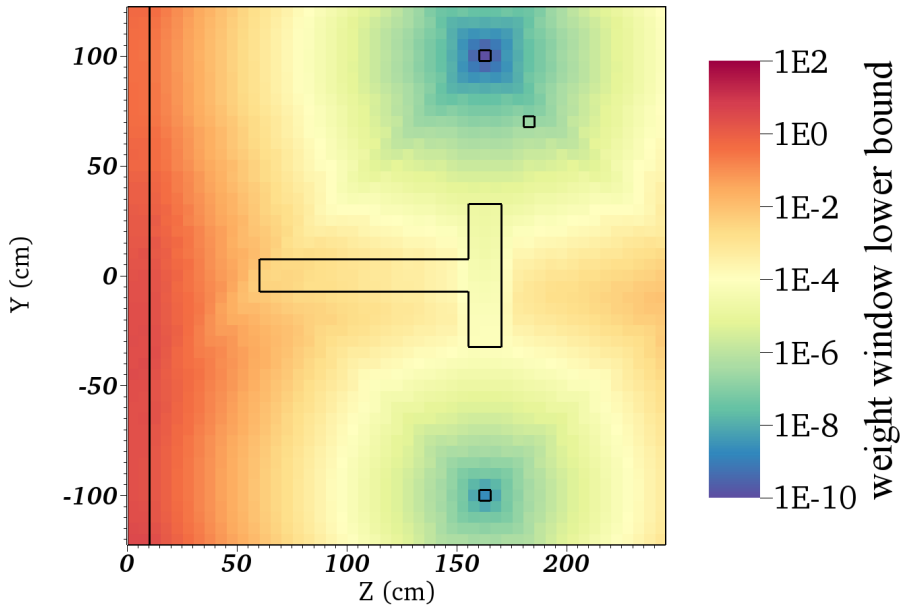

Figure 8.15: GTS-CADIS weight window distribution for the 12.5 – 12.8 MeV energy group at $\mathrm{x} = 0$.

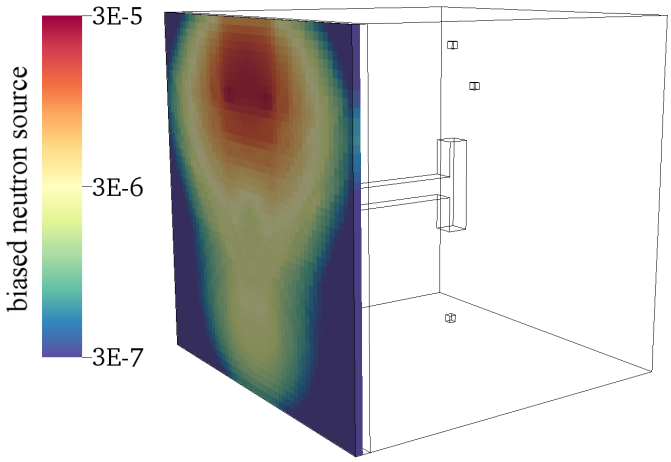

Figure 8.16: GTS-CADIS biased source distribution for the 13.8 – 14.2 MeV energy group.

8.16. For these high-energy groups, neutrons are biased more strongly toward the top volume. However, for low-energy groups it was observed that the weight window distribution strongly biases neutrons away from the top volume. This means that as neutrons downscatter near the top volume they are likely to be rouletted.

8.3.3 GTB-CADIS

GTB-CADIS was used to generate T for the top volume using perturbation parameters of $\mathsf{p} = 0.5$ and $\mathsf{p} = 1.5$. The T for $\mathsf{p} = 0.5$ is shown in Figure 8.17. In both cases, a uniform flux spectrum with a magnitude of 10^{10} cm^{-2} s^{-1} was used. This magnitude was chosen because is it similar to the magnitude of the neutron fluxes in the top volume shown in Figure 8.3. In practice, these neutron fluxes would not be known *a priori*, so this choice represents nearly the best case scenario. Unlike with the GT-CADIS and GTS-CADIS methods, this T has significant intensity for both fast and thermal neutrons. In other words, the multiple-neutron-interaction pathways are expected to be populated.

The adjoint neutron sources for $\mathsf{p} = 0.5$ and $\mathsf{p} = 1.5$ are shown in Figure 8.18. The shape of these adjoint neutron sources is similar to the shape of the cross sections in Figure 8.7 as expected. For energy groups with high adjoint neutron source intensity, the intensity is similar for $\mathsf{p} = 0.5$ and $\mathsf{p} = 1.5$. This was also observed for $\mathsf{p} = 0.1$ and $\mathsf{p} = 10$, indicating that T does not seem to be sensitive to p in this case. For energy groups in the epithermal region, with low adjoint neutron source intensity, differences are observed but these differences are unlikely to have an impact on the resulting VR parameters. Likewise, for both $\mathsf{p} = 0.5$ and $\mathsf{p} = 1.5$ the SDR calculated via Equation 8.4 was found to be $2.57{\cdot}10^{-9}$ Sv/s: 0.272 times the expected result. For this reason $\mathsf{p} = 0.5$ was arbitrarily chosen for VR parameter production. The resulting weight window and biased source distributions are shown in Figures 8.19 and 8.20, respectively. These VR parameters direct neutrons to both the top and bottom volumes fairly equally for the high-energy groups shown.

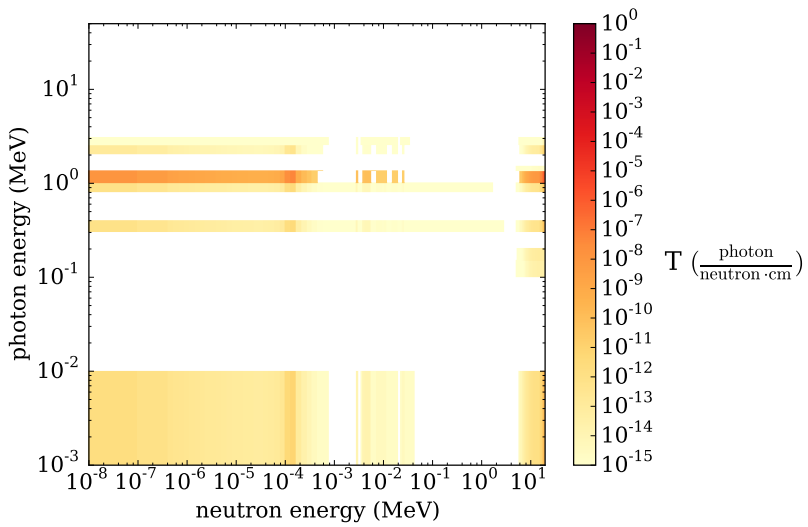

Figure 8.17: T for the top volume as calculated by the GTB-CADIS method with $\mathsf{p} = 0.5$.

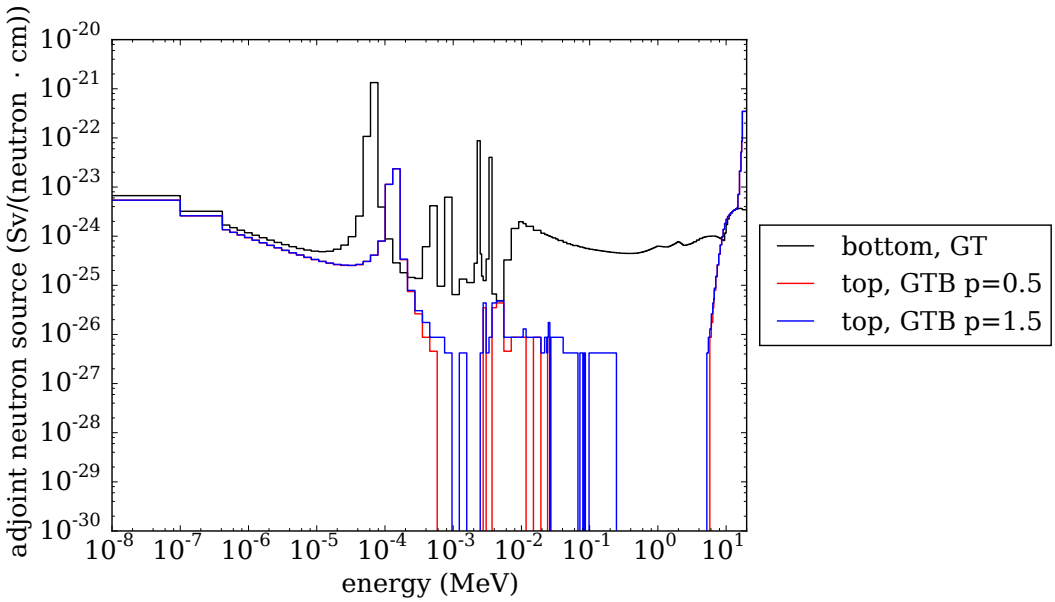

Figure 8.18: Adjoint neutron sources produced by the GTB-CADIS method.

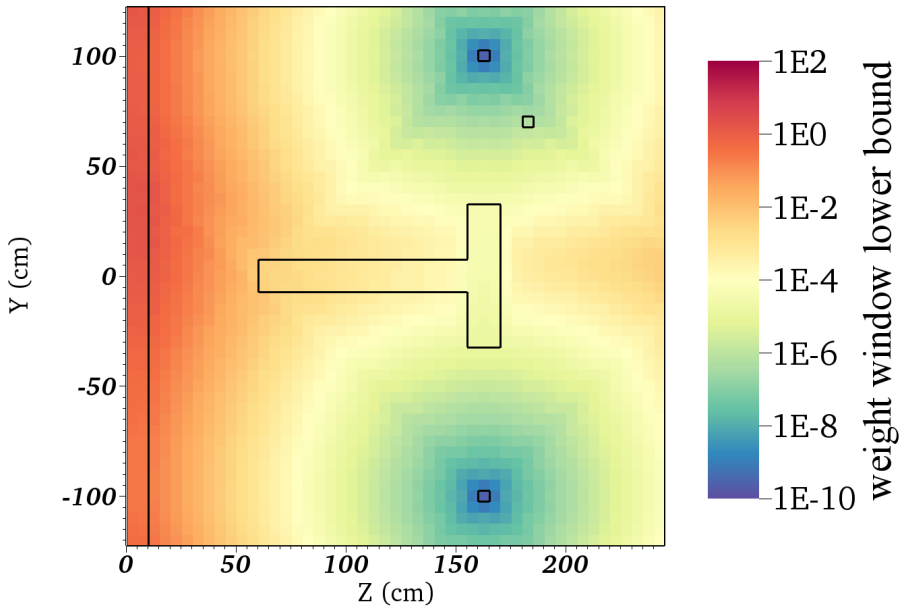

Figure 8.19: GTB-CADIS weight window distribution for the 12.5 – 12.8 MeV energy group at $x = 0$.

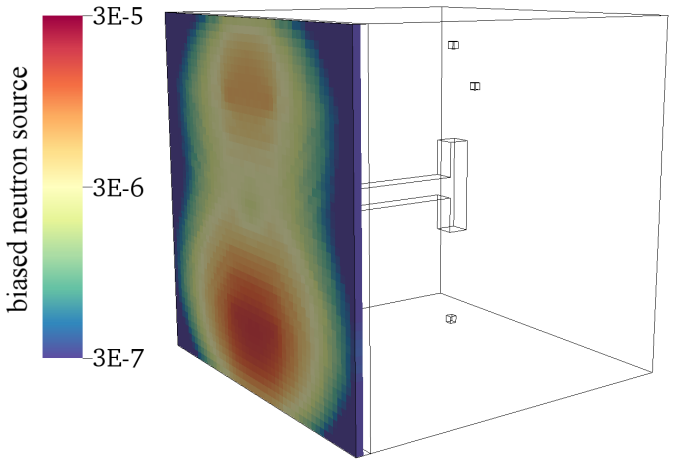

Figure 8.20: GTB-CADIS biased source distribution for the 13.8 – 14.2 MeV energy group.

8.3.4 GTSB-CADIS

The T produced via the GTSB-CADIS method is shown in Figure 8.21. A p of 0.5 was used, as was done with the GTB-CADIS method. This T is similar in shape to the GTB-CADIS T in Figure 8.17. The resulting adjoint neutron source is shown in Figure 8.22. This figure also shows the adjoint neutron source produced from the unnormalized T (e.g., T' in Equation 4.24). The magnitude of the adjoint neutron source is greater prior to normalization. Using the unnormalized adjoint neutron source the SDR is overpredicted by a factor of 2.00 via Equation 8.4. The weight windows and biased source distributions resulting from the normalized adjoint neutron source are shown in Figures 8.23 and 8.24 respectively. For the high-energy groups shown, GTSB-CADIS biases neutron more strongly toward the top volume.

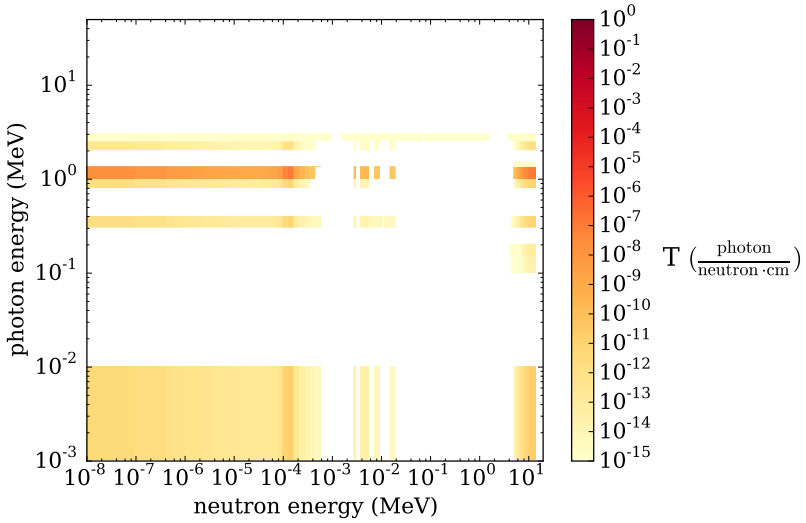

Figure 8.21: T for the top volume as calculated by the GTSB-CADIS method with $\mathsf{p} = 0.5$, with and without normalization.

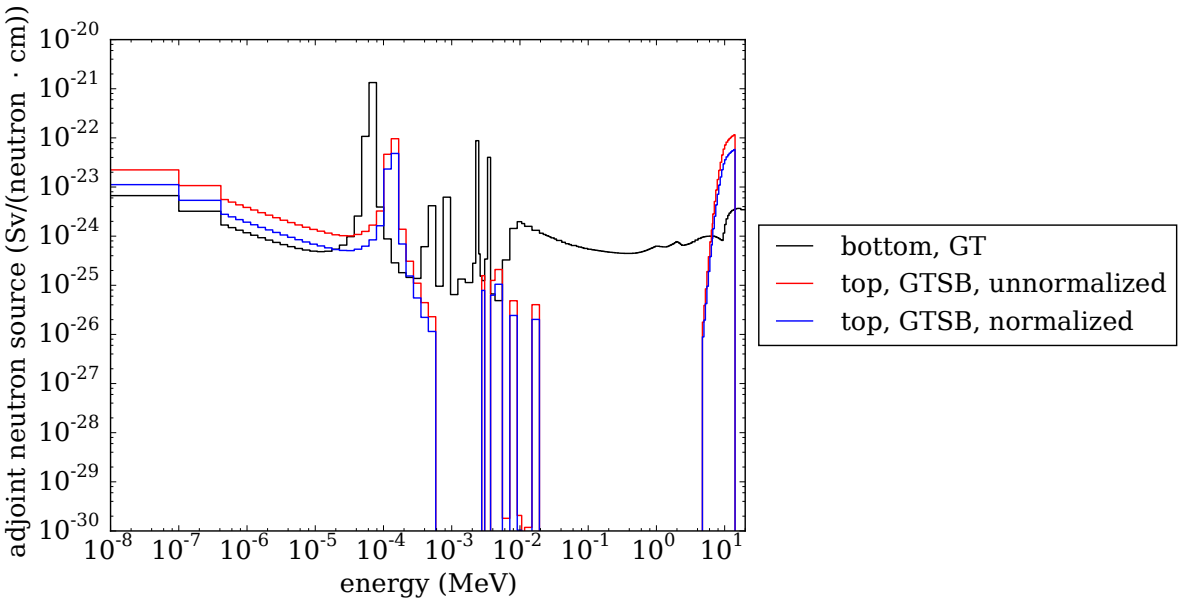

Figure 8.22: Adjoint neutron sources produced by the GTSB-CADIS method.

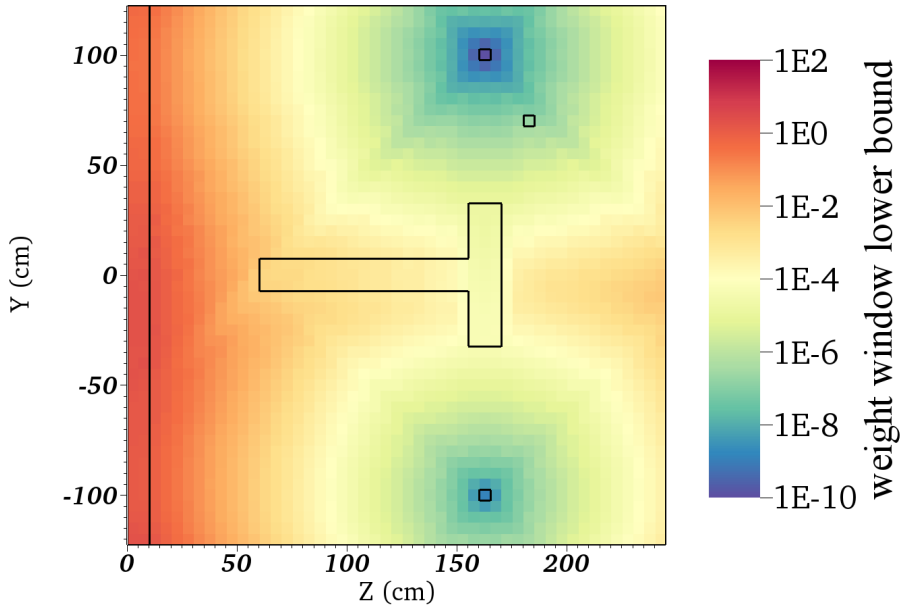

Figure 8.23: GTSB-CADIS weight window distribution for the 12.5 – 12.8 MeV energy group at $\mathrm{x} = 0$.

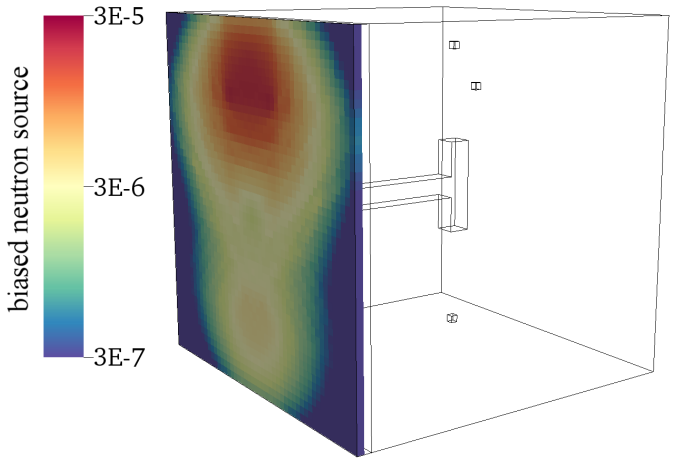

Figure 8.24: GTSB-CADIS biased source distribution for the 13.8 – 14.2 MeV energy group.

8.3.5 Summary of Methods Chosen for Experimentation

Adjoint neutron source spectra should have a shape that captures the cross sections of important reactions and a magnitude that captures the total importance (i.e., across all neutron energy groups) of a mesh volume element. The shapes of the adjoint neutron sources produced by each of the four methods are shown in Figure 8.25 and can be compared to the shapes of the cross sections in Figure 8.7. The magnitude of the adjoint neutron sources can be judged by comparing the SDR calculated by Equation 8.4 for each adjoint neutron source to the expected SDR. This information is summarized in Table 8.2.

The four methods capture each combination of correct shape and correct magnitude. With GT-CADIS, the shape of adjoint neutron source does not capture the importance of thermal neutrons, and does not have the correct magnitude. GTS-CADIS also has an

Table 8.2: SDRs calculated by Equation 8.4 for each adjoint neutron flux distribution. The fraction of the expected SDR is also shown using the expected SDRs from Table 8.1.

location	method	SDR (Sv/s)	fraction of expected SDR
bottom	GT	$9.22{\cdot}10^{-9}$	1.003
top	GT	$1.12{\cdot}10^{-13}$	$5.77 \cdot 10^{-6}$
top	GTS	$9.45{\cdot}10^{-9}$	1.000
top	GTB	$2.57{\cdot}10^{-9}$	0.272
top	GTSB	$9.45{\cdot}10^{-9}$	1.000

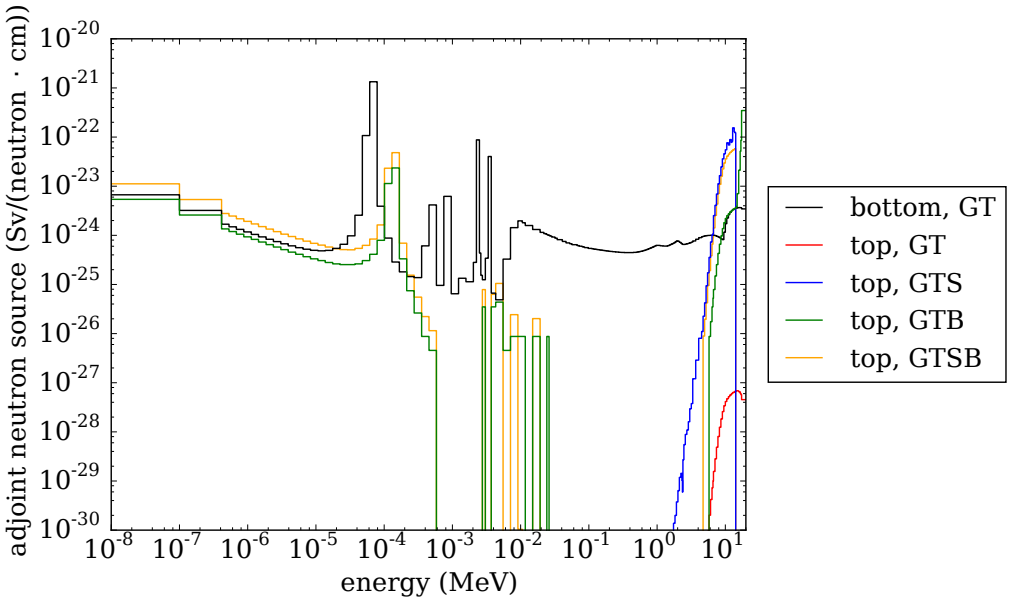

Figure 8.25: Adjoint neutron sources chosen for experimentation.

incorrect shape, but a correct magnitude. GTB-CADIS gives the correct shape, but with a incorrect magnitude (in this case approximately 4 times too low), and GTSB-CADIS gives both the correct shape and correct magnitude. The efficacy of these four methods will be compared, via the procedure explained in the next section.

8.4 Neutron Transport and R2S

The efficacy of the GT-, GTS-, GTB-, and GTSB-CADIS methods was assessed using a procedure similar to that used in Chapter 7. For each set of weight windows and biased sources, MC neutron transport was carried out for five neutron transport processor times, logarithmically spaced between 10^1–10^5 min. For each processor time, 10 trials were conducted. Each trial used a different random number seed and simulated a fixed number of particles. Trials were run on 4 computer cluster nodes with 20 cores per node and 80 MPI processes. Each node was an Intel® Xeon® E5-2670 v2 CPU with a clock speed of 2.50 GHz and 128 GB of RAM.

For the first 2 computer processor times, significant variation in computer processor times

was observed between trials, likely due to multiprocessing load balancing effects. For trials that resulted in computer processor times much shorter or longer than expected, the trials were rerun with different random number seeds. It should be emphasized that this was not done for the longest 3 computer processor times, for which the most useful information is garnered.

PyNE R2S was used to generate ALARA input for each trial. Activation was then done within the top and bottom volumes. Using the resulting photon emission densities, the SDR was calculated via Equation 2.8 (as was done in was done in Chapter 7), using the adjoint photon fluxes from Figure 8.6.

8.5 Results

The objective of this experiment was to compare the SDR convergence rates for each of the 4 sets of VR parameters. Total SDR results for each trial are shown in Figure 8.26, with the dashed line representing the sum of the converged SDRs from the top and bottom volumes from Table 8.1. The average and standard deviations of these SDRs are shown in Figure 8.27. In addition, similar plots are shown for the individual SDR contributions from the top and bottom volumes in Figures 8.28, 8.29, 8.30, and 8.31.

For the bottom volume results shown in Figures 8.30 and 8.31, all methods converge upon the expected result at a similar rate. However, for the top volume results in Figures 8.28 and 8.29 the SDR results from the GT- and GTS-CADIS methods are extremely low. With these methods important thermal neutrons are being rouletted in the vicinity of the top volume. In turn, most thermal neutron energy groups receive no MC scores, so the thermal flux is found to be zero. This undersampling causes a tremendous underestimation of the reaction rate for the $(\mathrm{n}, \boldsymbol{\gamma})$ reactions shown in Equation 8.3 resulting in an underestimation of the SDR. Since the GT- and GTS-CADIS methods still play a fair game the SDR in the top volume would converge for a sufficiently-long processor time. However due to the poor estimation of

the importance of thermal neutrons by these methods this processor time may eclipse that required for convergence via analog MC neutron transport.

For the GTB- and GTSB-CADIS methods, the performance for the top volume is similar. Both methods converge upon the expected result at similar rates to the convergence rate of the bottom volume. This is a promising result because the GTB-CADIS VR parameters were not created with the exact neutron spectrum, and were shown to have a magnitude about 4 times less than expected as shown in Table 8.2. This suggests that much of the benefit of these two methods comes from simply capturing the behavior of multiple neutron interactions.

Estimating the relative efficacy of these methods is complicated by the appearance of outliers, which are observed in results from both methods. The cause of one of these outliers was further investigated. For the GTSB-method, one trial resulted in a significantly higher SDR from the top volume at the 10^4 min processor time as seen in Figure 8.28. The neutron spectra in the top volume from this trial was obtained for the outlier trial and the other 9 points. Figure 8.32 shows a comparison between the outlier neutron spectrum and the average of the other 9 spectra. The ratio of the two is also shown. The outlier spectrum only differs from the average for the lowest 2 neutron energy groups, where it is approximately three times greater. These discrepancies may result from a single or small number of high-weight thermal neutrons streaming into the top volume. This explanation is consistent with the fact that outliers are only observed to have higher SDR results than expected. There is not enough data to determine whether this phenomenon is more likely to occur with VR parameters produced by either GTB- or GTSB-CADIS. Nonetheless, it is clear that both of these methods represent a significant improvement over the standard GT-CADIS method for this scenario.

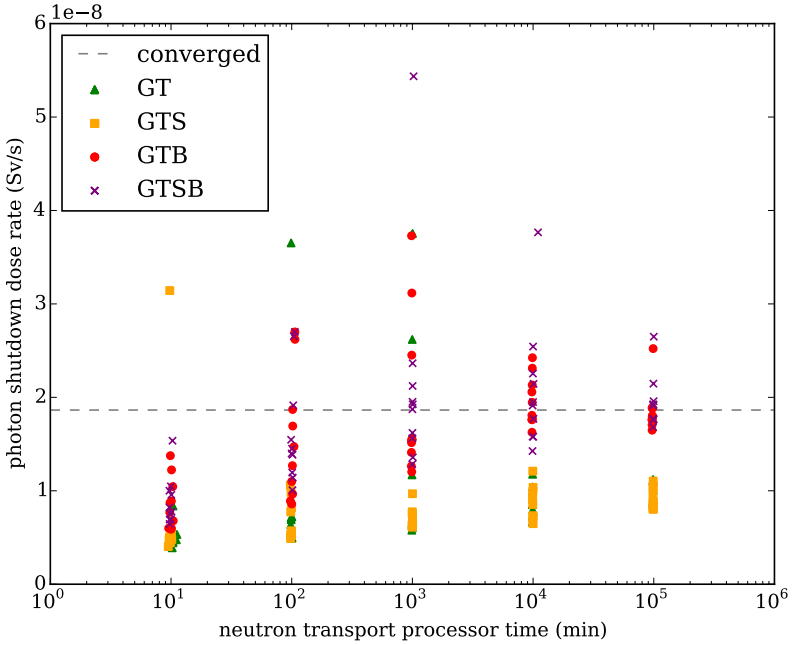

Figure 8.26: Total SDRs from the top and bottom volumes for each trial compared to the converged result from Table 8.1.

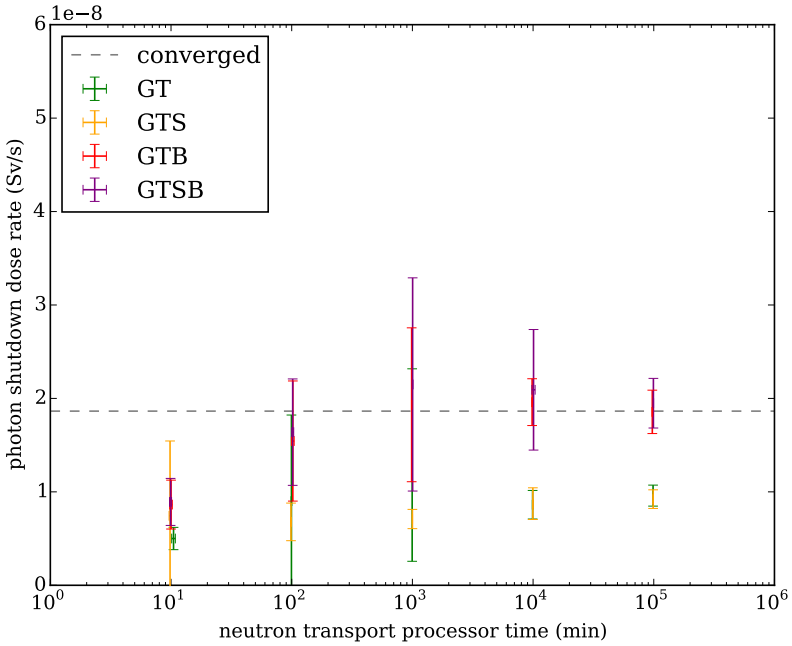

Figure 8.27: Average of total SDRs from the top and bottom volumes compared to the converged result from Table 8.1.

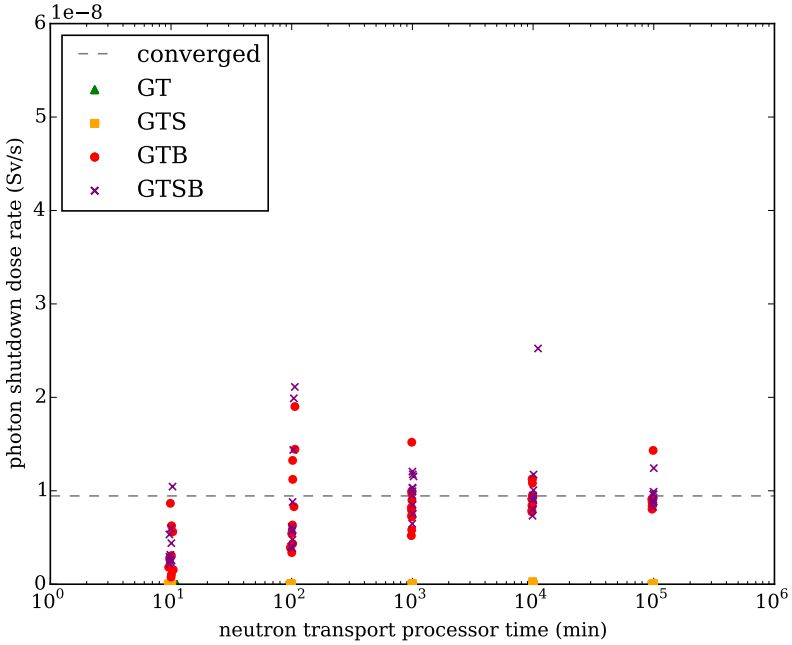

Figure 8.28: SDRs from the top volume for each trial compared to the converged result from Table 8.1.

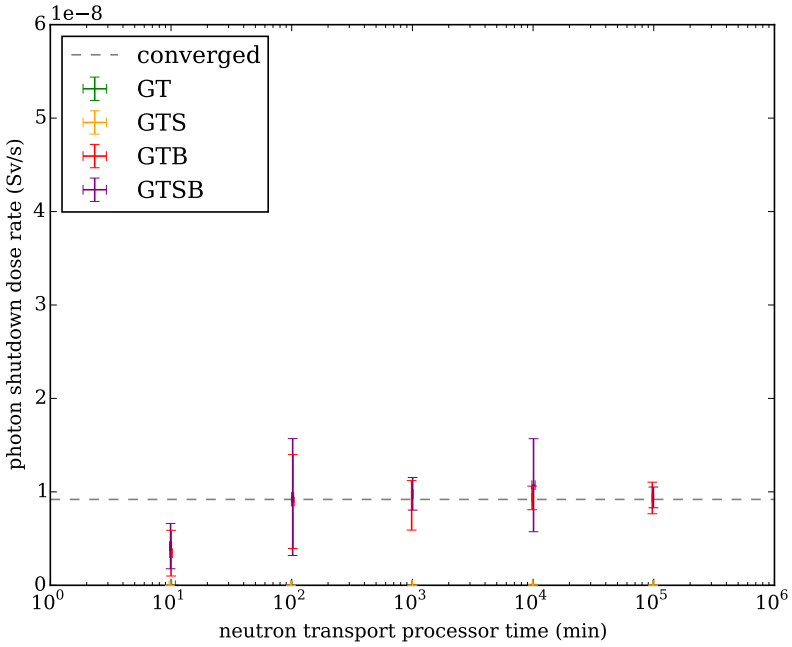

Figure 8.29: Average SDRs from the top volume compared to the converged result from Table 8.1.

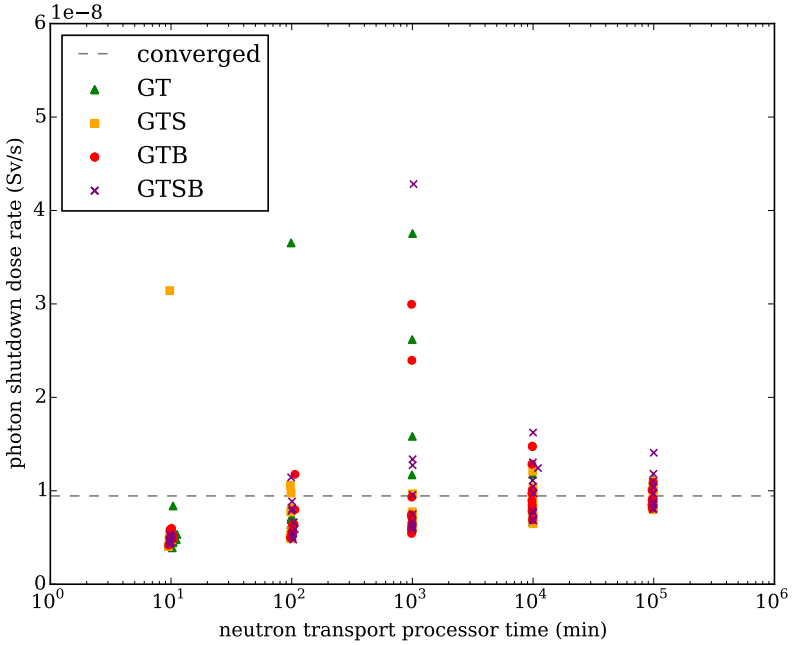

Figure 8.30: SDRs from the bottom volume for each trial compared to the converged result from Table 8.1.

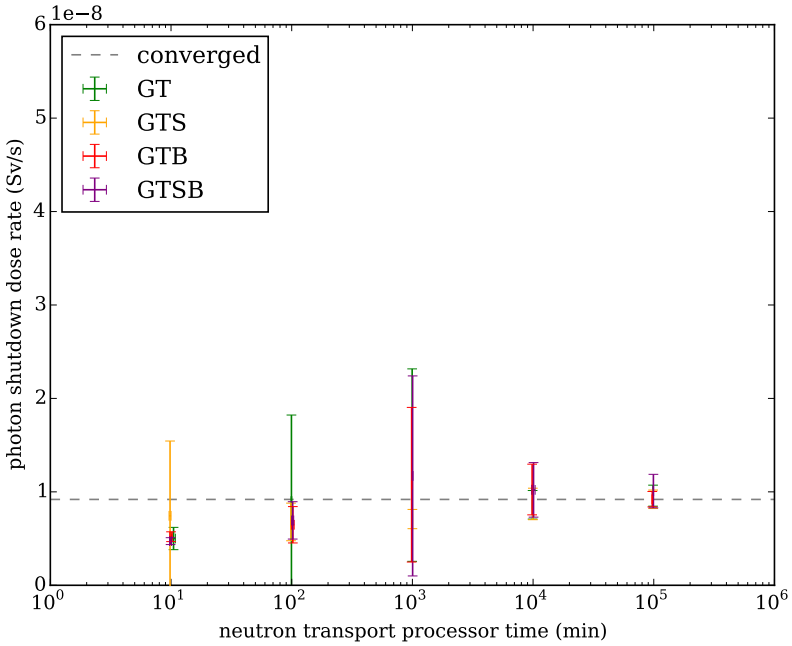

Figure 8.31: Average SDRs from the bottom volume compared to the converged result from Table 8.1.

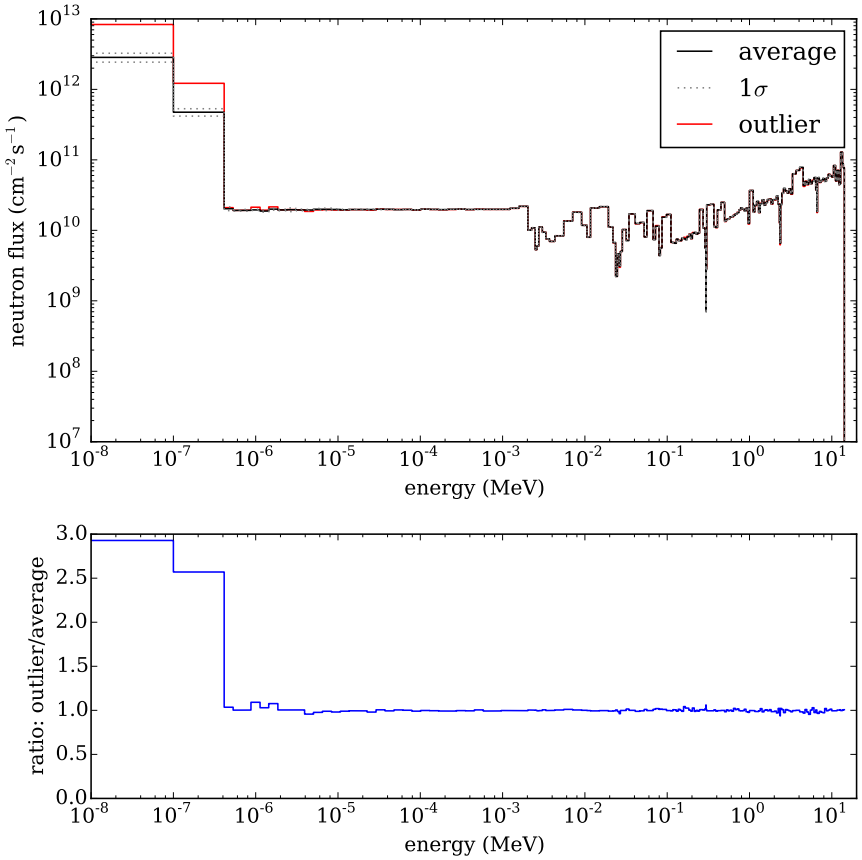

Figure 8.32: Neutron flux spectra in the top volume from the GTSB-CADIS outlier point for the 10^4 min processor time (as seen in Figure 8.26) compared to the average neutron spectrum of the other 9 points.

8.6 Conclusion

In Chapter 6 it was shown that the SNILB criteria are generally met for typical FES materials, spectra, and irradiation scenarios. However, some nuclides were found to significantly violate the SNILB criteria, most severely in cases where important radionuclides are produced by multiple neutron interactions. This chapter shows that in these special cases SNILB-violation methods can be used to obtain much better approximations for T than the GT-CADIS method.

In the problem described in this section a significant portion of the SDR results from a multiple-neutron-interaction pathway. Adjoint neutron sources produced via the GT- and GTS-CADIS methods were shown to neglect the importance of thermal neutrons. This

behavior was shown to be predictable through the calculation of η and η_I. With these methods, the thermal neutron flux is greatly undersampled in the top volume, resulting in an underestimation of the SDR. It does not appear that the GTS-CADIS method offers any additional benefit over the GT-CADIS method in this case.

The GTB- and GTSB-CADIS methods are shown to remedy this issue. Adjoint neutron sources produced via these methods are shown to capture the shape of the cross sections for both neutron interactions. With both methods, the SDR contributions from the top and bottom volumes converge at similar rates. Both methods had outlying trials for which the SDR was found to be significantly greater than average. Due to the presence of these outliers, more data would be needed to make definitive statements about the relative efficacy of these methods. The fact that the GTB-CADIS method seems to perform similarly the GTSB-CADIS method shows that detailed spectral information may not be required for the production of VR parameters. In other words, it appears that the shape of the adjoint neutron source is more important than the magnitude. This is a promising result because the GTSB-CADIS method requires the calculation of T in each volume element using deterministic forward neutron fluxes, whereas the GTB-CADIS can produce VR parameters by conducting irradiations for only pure materials without detailed knowledge of the neutron spectra.

Chapter 9

Production-Level Demonstration

In Chapters 7 and 8 the GT-CADIS and SNILB-violation methods were shown to be effective with simple demonstration problems. In this chapter, the GT-CADIS method is applied to a realistic problem. Unlike in previous chapters a complex geometry that does not conform to a Cartesian mesh is used, necessitating the mixing of T by volume fraction. A many-pulse irradiation scenario is used rather than a single irradiation and decay. In addition, photon dose rates are calculated with MC photon transport, as would be done for typical FES analysis, noting that in Chapters 7 and 8 deterministic adjoint photon flux distributions were used to calculate the SDR. For this demonstration, the 1 m version of the PPPL ST-FNSF was chosen. This small 27 MW (thermal) device has been proposed to further develop fusion blanket technology, namely tritium breeding and thermal power conversion [16].

9.1 Problem Description

Vertical and horizontal slices of the 1 m FNSF device are shown in Figure 9.1. A simplified CAD model of this device was obtained. This simplified model consists of only the inner-most portion of the geometry: everything inside the vacuum vessel. This model features homogenized breeding zones, blanket modules, center stack, and other components. Though the device is not exactly symmetrical vertically or radially, an octant of the geometry with reflective boundaries was chosen for this demonstration, allowing for a finer mesh resolution to be used. The chosen octant contains the Test Blanket Modules (TBM) labeled in Figure 9.1. The CAD model of the octant is shown in Figure 9.2 and annotated with material assignments. Homogenized material mixtures are defined in Table 9.1. Figure 9.2 also shows the location of the photon dose rate detector. This detector is sufficiently far from the

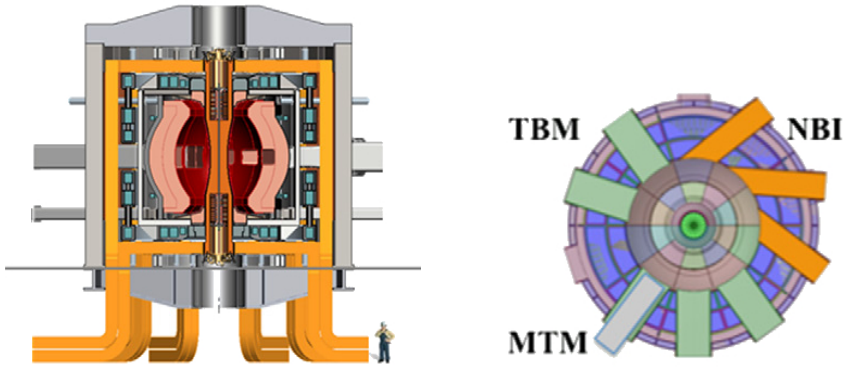

(a) vertical slice (b) midplane slice

Figure 9.1: Slices through the 1 m ST-FNSF device. The midplane slice shows the Tritium Breeding Modules (TBM), Neutral Beam Injectors (NBI), and Material Test Modules (MTM). Both slices are reproduced from Brown et al. [16].

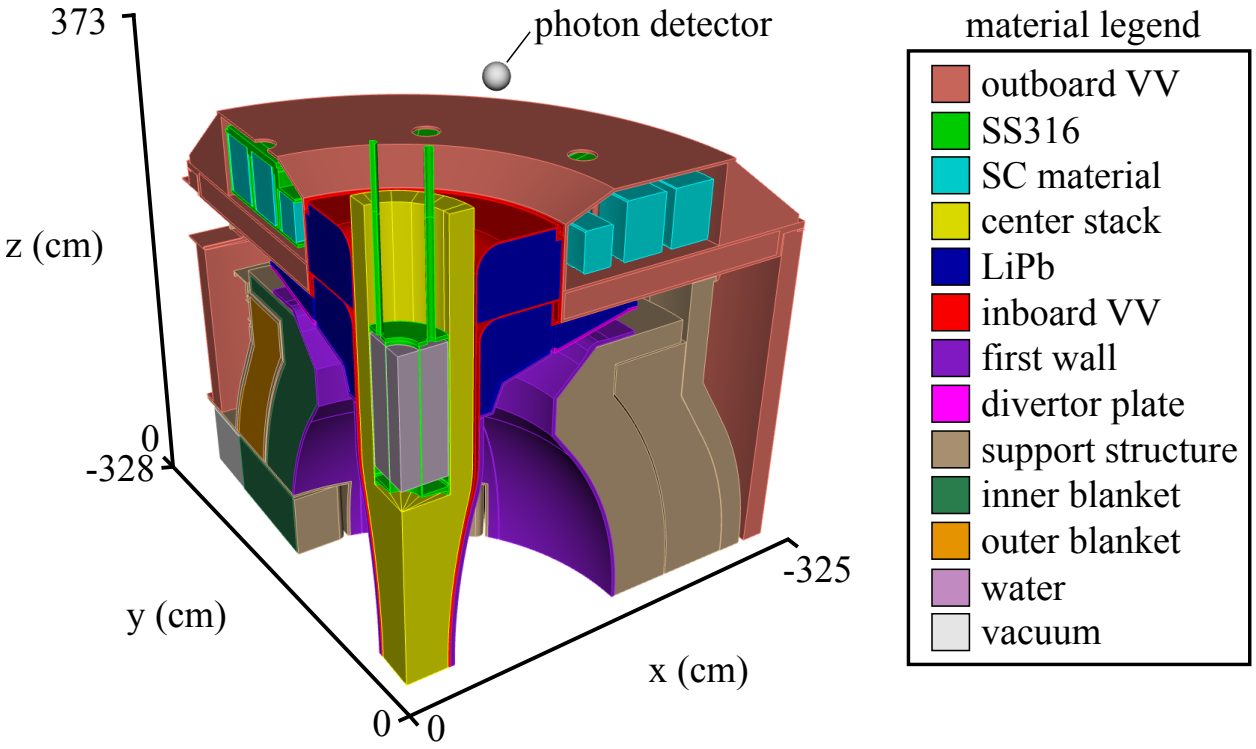

Figure 9.2: Octant of the 1 m ST-FNSF. Material mixture specifications appear in Table 9.1. Here "VV" denotes vacuum vessel and "SC" denotes superconducting.

reflecting boundaries that asymmetric effects are not expected to be significant.

The plasma neutron source was modeled using the DAGMC plasma source capabilities [45]. These capabilities allow for the random sampling of the initial positions and energies of neutrons born from plasma using several confinement modes [46] (noting that particle

Table 9.1: Volume fractions of materials within homogenized mixtures used in the FNSF geometry. For rows that do not add to 1, the remaining volume fraction is occupied by void.

mixture name	*MF82H*	*B-MF82H*	*ODS-MF82H*	*Magnet SS*	*GlidCop™*	*Cu*	*WTiC*	*LiPb, 90% enrich.*	*SiC*	*Nb_3Sn*	*water*	*He*	*R-GFF epoxy*
outboard VV	0.33	0.2									0.47		
SC material				0.7		0.15				0.02		0.1	0.03
center stack					0.78						0.22		
inboard VV	0.9											0.1	
first wall		0.27	0.08									0.65	
divertor plate							0.8					0.2	
support struct.	0.8											0.2	
outer blanket	0.045							0.840	0.038			0.033	
inner blanket	0.047							0.835	0.039			0.034	

Table 9.2: Parameters used for L-mode plasma neutron source generation.

parameter	value
minor radius (m)	0.5875
major radius (m)	1.05
pedestal radius (m)	0.4375
ion density, pedestal (m^{-3})	$1 \cdot 10^{20}$
ion density, separatrix (m^{-3})	$3 \cdot 10^{19}$
ion density, origin (m^{-3})	$1 \cdot 10^{20}$
ion temperature, pedestal (keV)	6.09
ion temperature, separatrix (keV)	0.1
ion temperature, origin (keV)	45.9
ion temperature peaking factor	8.06
ion density peaking factor	1.0
elongation	2.85
triangularity	0.53
Shafranov shift (m)	0.1

birth in plasma is isotropic). In order to employ biased neutron source sampling via the capabilities described in Section 5.4, a mesh-based representation of the forward neutron source is required. This was obtained by using the DAGMC plasma source capabilities to sample 10^8 particles. This was done using the low-confinement (L) mode with plasma parameters listed in Table 9.2. The positions and energies of these neutrons were then tallied on a mesh in the VITAMIN-J 175 energy group format. A nonuniform 62×62×69 mesh (265,236 mesh volume elements) was used for this purpose and for the rest of this problem. This mesh was created by hand to conform to important geometry boundaries. By dividing the number of tallies in each energy group in each mesh volume element by the volume of each mesh volume element the mesh-based PDF for the source density was obtained. This PDF was then normalized to 1. The resulting source density for the dominant energy group (13.8–14.2 MeV) is shown in Figure 9.3. This figure (and the remaining figures in this chapter) show a slice through the geometry at a 45° angle.

The total source intensity of the octant was chosen to be $1.197 \cdot 10^{18}$ n/s, which corresponds to 27 MW of fusion power within the full device. A complex irradiation and decay scenario was chosen, as shown in Figure 9.4. This scenario consists of approximately 9 years of pulsed

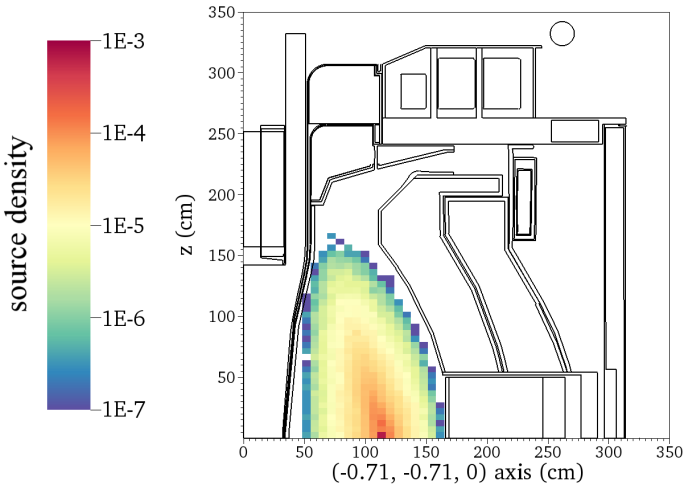

Figure 9.3: Neutron source density distribution for the 13.8 – 14.2 MeV energy group.

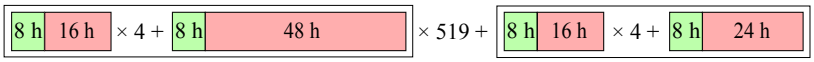

Figure 9.4: Scenario consisting of approximately 9 years of pulsed irradiation, followed by a 1 day shutdown period. Green represents irradiation intervals and red represents decay intervals.

irradiation, followed by a 1 day shutdown period, which are relevant time scales for FES operation and maintenance planning.

For this problem, DAG-MCNP5 with FENDL-2.1 nuclear data was used for all MC transport. All deterministic transport was carried out with PARTISN using P_5S_{16}, FENDL-2.1 nuclear data, and the VITAMIN-J group structure (175 neutron groups, 42 photon groups). Activation was done with ALARA with FENDL/A-3.0 nuclear data.

9.2 Generating Neutron Weight Windows and Biased Source

In order to generate weight windows and a biased source for this problem, the SNILB criteria were first evaluated for the materials in this problem in order to determine if the GT-CADIS method could be used or if an SNILB-violation method was required. This was done by evaluating η_I for each material using the irradiation scenario of interest and the characteristic

Table 9.3: Values of η_I for the FNSF materials, the spectra from Figure 6.3, and irradiation and decay scenario from Figure 9.4. ICRP-74 flux-to-dose-rate conversion factors were used for I_h.

	η_I		
Material	first wall	shield	vacuum vessel
outboard vv	1.02	1.00	1.00
SS316	1.04	1.00	1.00
SC material	1.03	1.01	1.00
center stack	1.00	1.00	1.00
LiPb	1.02	1.00	1.00
inboard vv	1.02	1.00	1.00
first wall	1.02	0.99	1.00
divertor plate	0.97	1.00	1.00
support structure	1.02	1.00	1.00
outer blanket	1.02	1.00	1.00
inner blanket	1.02	1.00	1.00
water	1.00	1.00	1.00

FES neutron spectra from Figure 6.3. Resulting η_I values are shown in Table 9.3. This table shows that for all spectra and materials, all η_I are within 4% of 1. This indicates that the SNILB criteria are valid in this case and the standard GT-CADIS method can be used to produce optimal VR parameters.

Proceeding with GT-CADIS, VR parameters were generated with a similar procedure as used in Chapters 7 and 8. A deterministic adjoint photon transport calculation was first done using the detector shown in Figure 9.2 as the adjoint source with ICRP-74 flux-to-dose-rate conversion factors defining the adjoint source spectrum. This was done with 4 computer cluster nodes with 16 MPI processes per node. Each node was an Intel® Xeon® E5-2670 v2 CPU with a clock speed of 2.50 GHz and 128 GB of RAM.

Unlike in previous chapters where each mesh volume element contained exactly one geometry cell and therefore one material, significant portions of the mesh used for this problem contained multiple geometry cells, resulting in a large number of unique mixtures. Due to computer memory limitations, this collection of mixtures was collapsed down into a small set of approximate mixtures. This was done using a 25% relative tolerance. In other

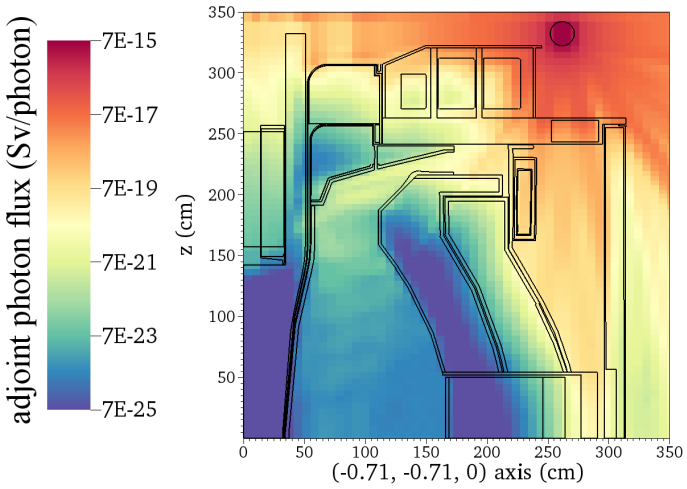

Figure 9.5: Adjoint photon flux distribution for the 0.8 – 1.0 MeV energy group.

words, if the volume fractions of the all the materials within two mixtures were within 25% of each other, these two mixtures were represented by a single mixture. The adjoint photon flux distribution is shown in Figure 9.5.

Next, T was calculated for all of the materials in the problem for the irradiation scenario of interest. These T were then mixed by volume fraction in order to obtain a T for each mesh volume element. This was done using the actual volume fractions within each mesh volume element — not the approximate volume fractions used for generating PARTISN input. Figure 9.6 shows the $\mathsf{T}_{\mathsf{g},\mathsf{h}}$ distribution for the 1.0–1.11 MeV neutron energy group (g) and the 0.8 – 1.0 MeV photon energy group (h). This figure shows that $\mathsf{T}_{\mathsf{g},\mathsf{h}}$ for the poloidal field (PF) coil material is approximately two orders of magnitude greater than any other material for this particular g and h. The striped patterns in the bottom of the plot are a result of the 45° slice through the geometry, which intersects the mesh volume elements diagonally.

The T for each mesh volume element and the adjoint photon flux were used to calculate the adjoint neutron source distribution shown in Figure 9.7. This figure shows that the most important spatial regions for neutrons are the areas of the PF coil and structural material in the immediate vicinity of the detector. For the purpose of comparison, an adjoint neutron source was also calculated via the FW-CADIS method, shown in Figure 9.8. As expected, the adjoint source intensity is inversely proportional to the forward flux. Since the detector

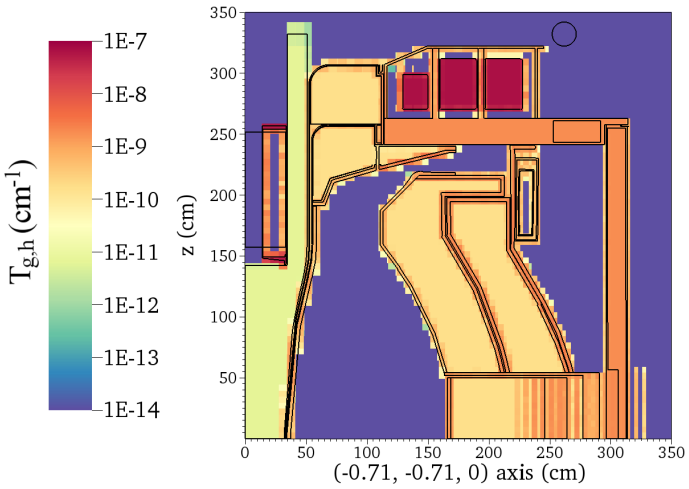

Figure 9.6: $\mathsf{T}_{\mathsf{g},\mathsf{h}}$ distribution for the 1.0–1.11 MeV neutron energy group (g) and the 0.8 – 1.0 MeV photon energy group (h).

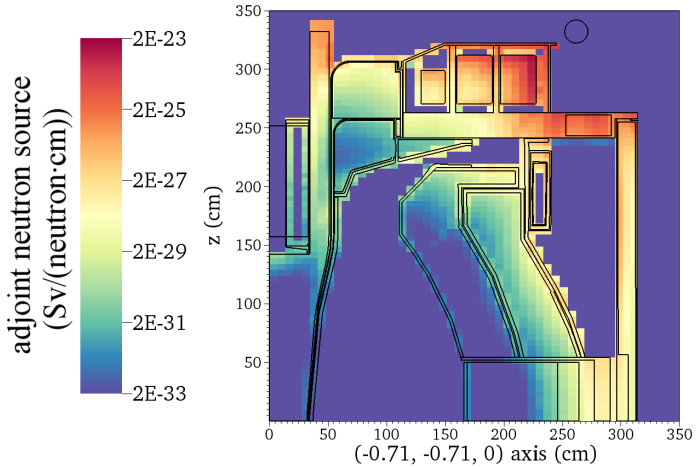

Figure 9.7: GT-CADIS adjoint neutron source distribution for the 1.0 – 1.11 MeV energy group.

happens to be in the region of lowest forward flux in this problem, the FW-CADIS method would likely provide significant speedup over analog. However, unlike the GT-CADIS method, FW-CADIS has high adjoint source intensity in the region behind the vacuum vessel, which will result in neutrons wastefully being directed toward this region.

Adjoint neutron transport was then carried out with the same run configuration and mixture collapsing criterion as adjoint photon transport. The adjoint neutron flux distribution is shown in Figure 9.9. Using this adjoint neutron flux, neutron weight windows and a biased source were generated, as shown in Figures 9.10 and 9.11. The adjoint neutron flux

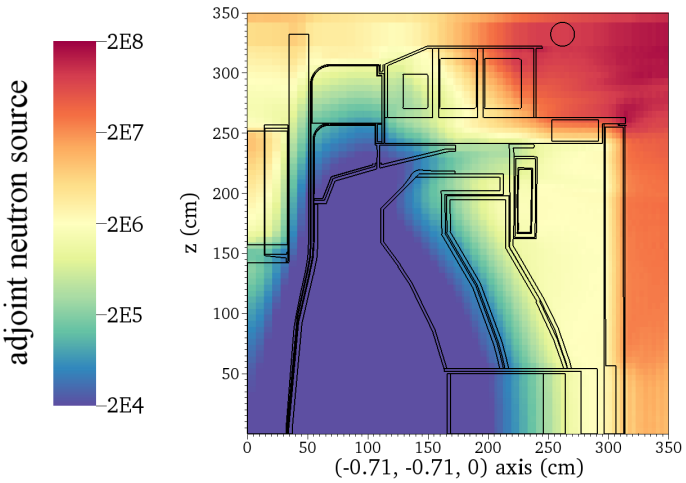

Figure 9.8: FW-CADIS adjoint neutron source distribution for the 1.0 – 1.11 MeV energy group.

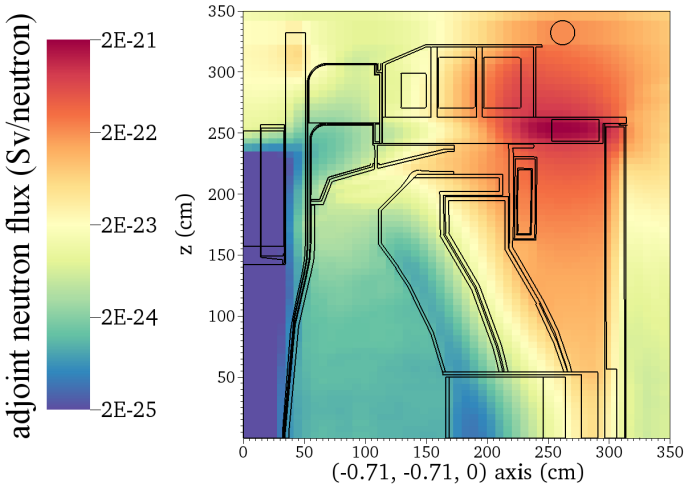

Figure 9.9: Adjoint neutron flux distribution for the 1.0 – 1.11 MeV energy group.

distribution and resulting weight window distribution show that the importance is nearly uniform throughout the plasma region. Likewise, the biased neutron source distribution is nearly identical to the unbiased source distribution shown in Figure 9.3. The weight window distribution suggests that streaming through the gap below the divertor plate is a more important pathway than diffusion through first wall and outboard blanket modules.

The contributon flux distribution resulting from the GT-CADIS adjoint neutron flux was also calculated using Equation 2.9 as seen in Figure 9.12. This plot confirms that neutrons primarily stream through the divertor region in order to reach import areas of the geometry.

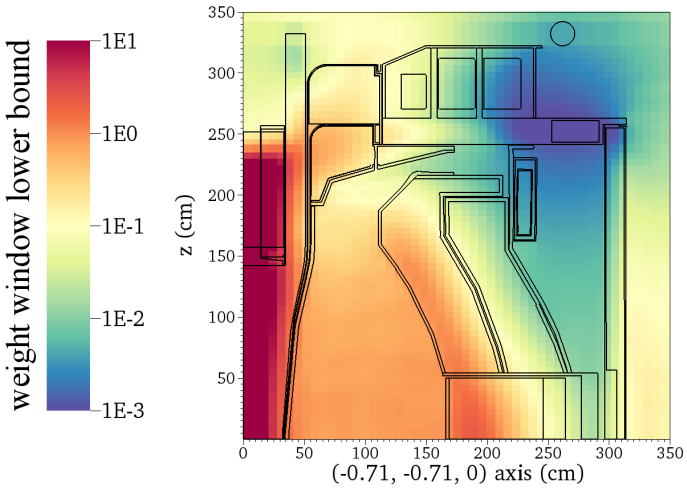

Figure 9.10: Neutron weight window distribution for the 1.0 – 1.11 MeV energy group.

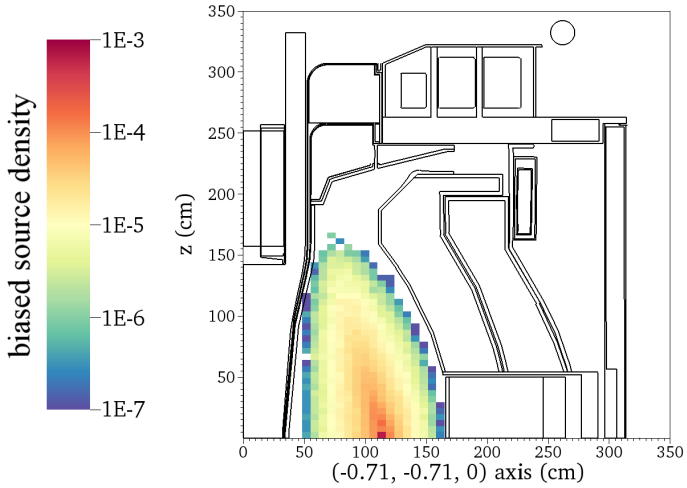

Figure 9.11: Biased neutron source density distribution for the 13.8 – 14.2 MeV energy group.

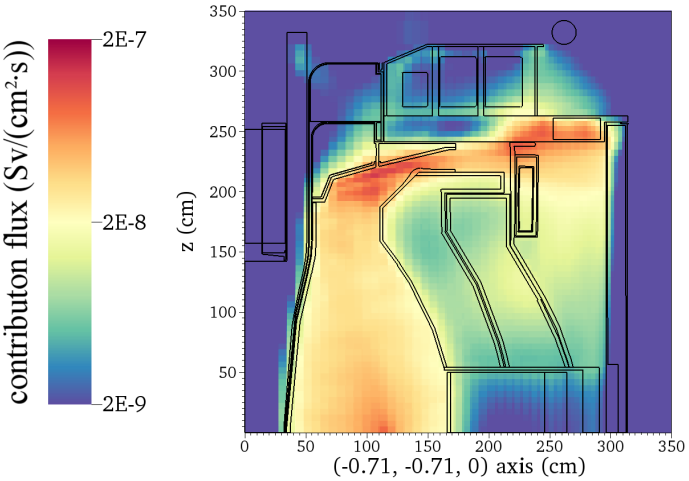

Figure 9.12: Total contributon flux distribution across all energy groups.

9.3 R2S

In to order calculate the SDR, neutron transport was first done using the GT-CADIS weight windows and biased source. This was done using the same hardware as deterministic transport but with 8 nodes and 20 MPI tasks per node. A total of $2{\cdot}10^9$ particles were simulated in 311 days of CPU time.[1]

The total neutron flux distribution is shown in Figure 9.13 with the relative error distribution shown in Figure 9.14. The neutron flux distribution shows the total neutron flux is attenuated by approximately 5 orders of magnitude between the source and detector. The relative error distribution shows that significantly less processor time is spent simulating particles in the center stack, outboard breeding zones and deep within the PF coils. A region of lower relative error is seen outwards of the outer PF coil. This is due to the fact that the PF coils block streaming high-weight particles that increase the variance in the surrounding vacuum regions. Relative errors are less than 1% for the most important regions (regions of high adjoint neutron flux in Figure 9.9).

Using PyNE R2S, ALARA input was generated and ALARA was run for each mesh

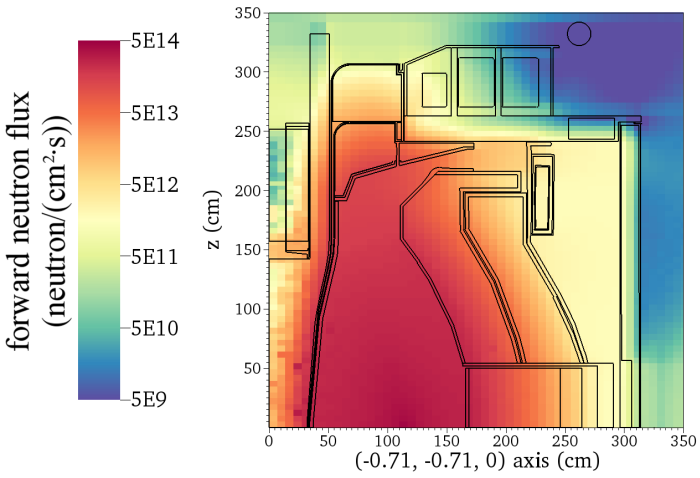

Figure 9.13: Total neutron flux distribution.

[1]During neutron transport an average of 1 in 5,600 particles were lost. Further analysis indicated that these lost particles were not confined to any single region, indicating significant issues with the CAD geometry. For FES analysis lost particles are common, and the loss rate must be weighed against the significance of the calculation. Since neutron flux and relative error distributions are consistent with expectations, this loss rate was deemed acceptable for the purpose of this demonstration.

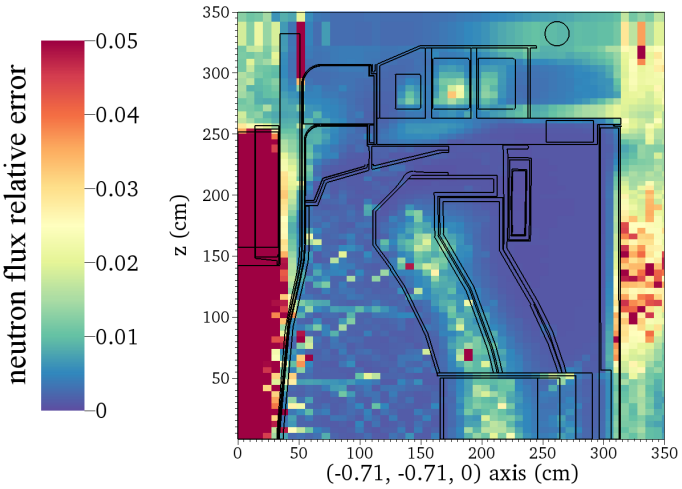

Figure 9.14: Total neutron flux relative error distribution.

volume element. The resulting photon emission density is shown in Figure 9.15. This figure shows that the first wall has 2–3 orders of magnitude greater photon emission density than the important regions of the problem (regions of high adjoint photon flux in Figure 9.5). For this reason, the standard CADIS method was used to generate weight windows and a biased source for the problem, shown in Figures 9.16 and 9.17 respectively. Since the adjoint photon flux was already required for GT-CADIS, no additional deterministic transport was required for this step.

Photon transport was done using these weight windows and a biased source with 10^{10} particles simulated on the same hardware and configuration as neutron transport. [2] Photon transport took 48.0 days of CPU time and resulted in a converged SDR of 4.02 $\cdot 10^{-5}$ Sv/s with a photon transport relative error of 0.0014. The calculated SDR for this problem is extremely high: these results indicate that after ~9 years of operation at full power, a much longer cooldown time should occur in order to perform any maintenance operations.

[2]Photon transport resulted in fewer lost particles than neutron transport: only 1 in 2.01 $\cdot 10^5$.

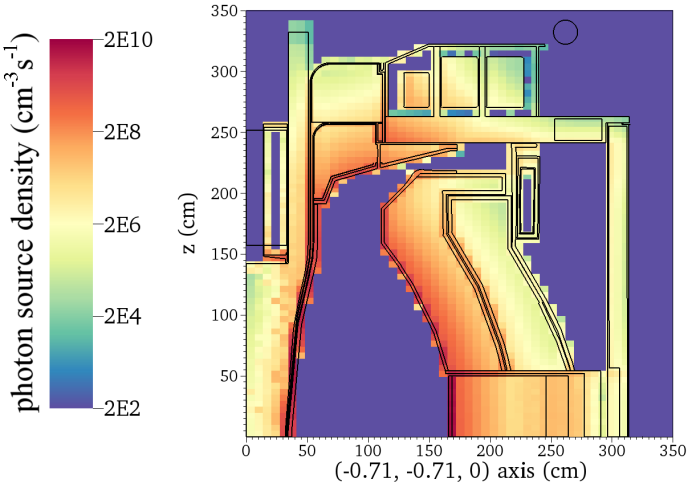

Figure 9.15: Photon emission density distribution for the 0.8–1.0 MeV energy group.

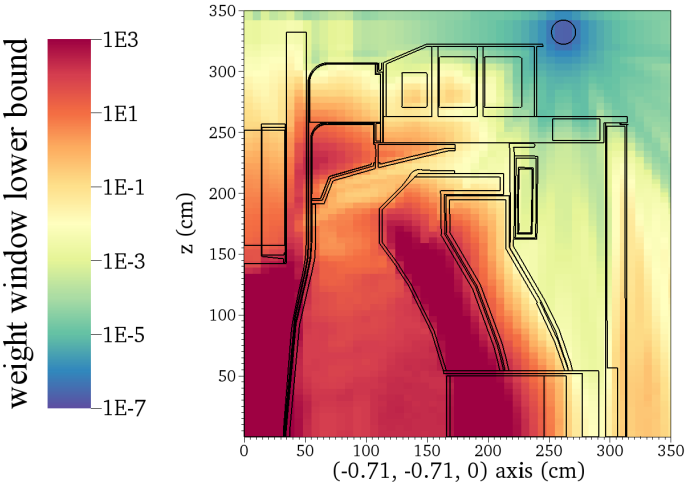

Figure 9.16: Photon weight window distribution for the 0.8 – 1.0 MeV energy group.

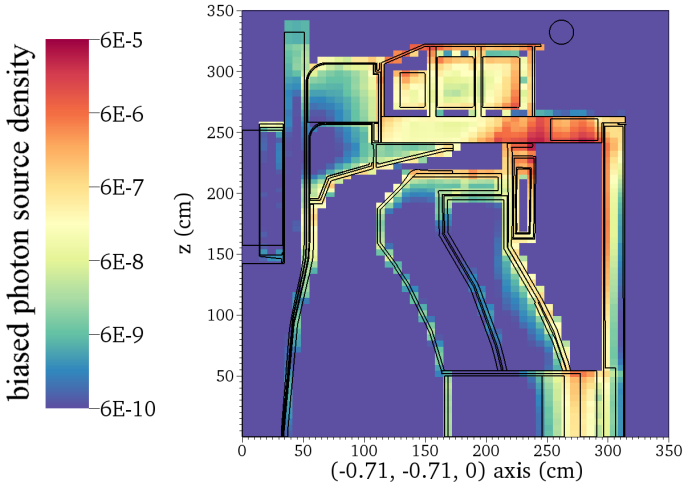

Figure 9.17: Biased photon emission density distribution for the 0.8 – 1.0 MeV energy group.

9.4 Conclusion

This chapter detailed the process of how the GT-CADIS method can be used in practice. A realistic geometry and irradiation scenario were chosen. The quantity η_I was first evaluated for each material in the problem using the irradiation scenario of interest and characteristic FES neutron spectra. This process provided *a priori* knowledge that the SNILB criteria are reasonably met for this problem and that the GT-CADIS method would be effective, without employing any of the SNILB-violation methods. Weight windows and a biased source were then generated using GT-CADIS. No significant challenges were encountered generating T using a complex irradiation scenario for each material and mixing T by volume fraction to obtain T in each mesh volume element. The resulting weight window distribution took on the expected shape — clearly biasing neutrons toward the important regions of the problem. The biased source shape indicated that source biasing may not be paramount for this class of problems. The use of the GT-CADIS method also allowed for the standard CADIS method to be employed for photon transport without any additional deterministic transport steps. It is clear that the GT-CADIS method can, and should, be applied to production-level problems, much like the standard CADIS and FW-CADIS methods which are in wide use today.

Chapter 10

Conclusion and Future Work

The MS-CADIS method describes a procedure for optimizing MC neutron transport for SDR analysis. The formulation of the MS-CADIS adjoint neutron source requires T, a quantity that relates neutron flux to photon emission density. In this work, an approximate solution for T is developed from first principles. The SNILB criteria delineate when this solution, the SNILB solution for T, is valid. Important radionuclides must be produced via single-neutron-interaction pathways that meet a low burnup criteria. The extent to which the SNILB criteria are met can be quantified through the calculation of η and η_{I}. The GT-CADIS method is an implementation of the MS-CADIS method that calculates T through a series of single-energy-group irradiations. When the SNILB criteria are met, the GT-CADIS T is equivalent to the SNILB solution. In special cases where the SNILB criteria are egregiously violated, the GT-CADIS method is not expected to be effective. A suite of SNILB-violation methods have been proposed for these scenarios. These methods modify the GT-CADIS method by using either detailed *a priori* knowledge of forward neutron flux spectra (GTS-CADIS), irradiations using a background neutron spectrum (GTB-CADIS), or both (GTSB-CADIS).

In Chapter 6 it was shown that the SNILB criteria are reasonably met for typical FES materials and neutron spectra, over a range of irradiation scenarios. The SNILB criteria are egregiously violated for some nuclides and these violations are more severe at high fluence and via multiple-neutron-interaction pathways. For this reason it is recommended that the SNILB criteria be evaluated for problems of interest prior to using the GT-CADIS method, to determine if SNILB-violation methods are necessary.

In Chapter 7 a simple problem where the SNILB criteria are met was generated. The GT-CADIS method was shown to result in speedups of 200 ± 100 relative to FW-CADIS

and $9 \pm 5 \cdot 10^4$ relative to analog. These speedups indicate that the computational resources required to obtain SDR results can be drastically reduced by using the GT-CADIS method.

The problem contrived in Chapter 8 violates the SNILB criteria via a dominant multiple-neutron-interaction pathway. The poor performance of the GT-CADIS method in this problem was predicted through the calculation of η and η_I. It was shown that in order to capture the behavior of multiple neutron interactions, irradiations with multiple energy groups simultaneously are required for the calculation of T. The GTS-CADIS method provided no additional benefit over GT-CADIS. The GTB- and GTSB-CADIS methods both offered significant performance improvements over GT-CADIS. The fact that the GTB-CADIS method performed similarly to GTSB-CADIS is an exciting result because it suggests that detailed neutron spectra information may not be paramount, even when the SNILB criteria are violated.

In Chapter 9, the GT-CADIS method was applied to a production-level problem. The 1 m ST-FNSF geometry and a ~9 year, many-pulse, irradiation scenario were used. In order to confirm that the GT-CADIS method would be effective for this problem, η_I was first calculated and found to be within 4% of 1 for all materials. The weight windows automatically produced by the GT-CADIS method clearly biased neutrons toward importance regions of the problem. It was also shown that the CADIS method can be used for MC photon transport without any additional deterministic transport.

This work has also opened up a number of interesting research questions. The GTB-CADIS method was shown to be effective without detailed knowledge of the neutron spectra and had similar performance to the GTSB-CADIS method. The relative performance of these methods could be further explored to see if this result holds for a variety of scenarios. Since the GTB-CADIS method produces the same T as GT-CADIS when the SNILB criteria are met, the GTB-CADIS method may be useful as a general purpose method, not only when the SNILB criteria are violated. Also, this work only considered target-based SDR problems. Though the application of the MS-CADIS method to global SDR problems has

been proposed, this has not yet been demonstrated in published work. The success of the GT-CADIS method motivates this further application. Finally, the fact that the SNILB criteria are generally met for FES scenarios motivates the use of T calculated via groupwise irradiations for the D1S method. Since the choice of T in the D1S method affects the final answer for the SDR, this application requires further research.

From this work it is clear that the MS-CADIS method and specifically the GT-CADIS implementation are broadly applicable to FES scenarios, will significantly reduce the computational resources necessary for calculating the SDR, and are ready for immediate use. This work has furthered the state-of-the-art and also opened up a variety of interesting research questions for future investigation.

References

[1] EUROFUSION, "JET: Europe's Largest Fusion Device — Funded and Used in Partnership," `https://www.euro-fusion.org/jet/` (2016), Online; accessed 2015-03-26.

[2] MAX-PLANCK-INSTITUT FÜR PLASMAPHYSIK, "Wendelstein 7-X," `http://www.ipp.mpg.de/16900/w7x` (2016), Online; accessed 2015-03-26.

[3] ITER ORGANIZATION, "ITER — The way to new energy," `http://iter.org` (2015), Online; accessed 2015-09-16.

[4] Y. CHEN and U. FISCHER, "Rigorous MCNP Based Shutdown Dose Rate Calculations: Computational Scheme, Verification Calculations and Application to ITER," *Fusion Engineering and Design*, **63–64**, 107–114 (2002).

[5] E. D. BIONDO, A. DAVIS, and P. P. H. WILSON, "Shutdown dose rate analysis with CAD geometry, Cartesian/tetrahedral mesh, and advanced variance reduction," *Fusion Engineering and Design*, **106**, 77–84 (2016).

[6] J. P. CATALÁN, P. SAUVAN, and J. SANZ, "Shutdown dose rate assessment for a DCLL blanket-based reactor: Application of the R2S-UNED approach," *Fusion Engineering and Design*, **88**, *9–10*, 2088–2091 (2013), Proceedings of the 27th Symposium On Fusion Technology (SOFT-27); Liège, Belgium, September 24–28, 2012.

[7] A. DAVIS and R. PAMPIN, "Benchmarking the MCR2S system for high-resolution activation dose analysis in ITER," *Fusion Engineering and Design*, **85**, *1*, 87–92 (2010).

[8] M. MAJERLE, D. LEICHTLE, U. FISCHER, and A. SERIKOV, "Verification and validation of the R2Smesh approach for the calculation of high resolution shutdown dose rate distributions," *Fusion Engineering and Design*, **87**, *5-6*, 443–447 (2012).

[9] P. PERESLAVTSEV, U. FISCHER, D. LEICHTLE, and R. VILLARI, "Novel approach for efficient mesh based Monte Carlo shutdown dose rate calculations," *Fusion Engineering and Design*, **88**, *9–10*, 2719–2722 (2013), Proceedings of the 27th Symposium On Fusion Technology (SOFT-27); Liège, Belgium, September 24–28, 2012.

[10] A. HAGHIGHAT and J. C. WAGNER, "Monte Carlo Variance Reduction with Deterministic Importance Functions," *Progress in Nuclear Energy*, **42**, *1*, 25–53 (2003).

[11] J. C. WAGNER, D. E. PEPLOW, and S. W. MOSHER, "FW-CADIS Method for Global and Regional Variance Reduction of Monte Carlo Radiation Transport Calculations," *Nuclear Science and Engineering*, **176**, *1*, 37–57 (2014).

[12] A. M. IBRAHIM, P. P. WILSON, M. E. SAWAN, ET AL., "Assessment of fusion facility dose rate map using mesh adaptivity enhancements of hybrid Monte Carlo/deterministic techniques," *Fusion Engineering and Design*, **89**, *9–10*, 1875–1879 (2014), Proceedings of the 11th International Symposium on Fusion Nuclear Technology-11 (ISFNT-11) Barcelona, Spain, 15-20 September, 2013.

[13] A. TURNER, R. PAMPIN, M. LOUGHLIN, ET AL., "Nuclear analysis and shielding optimisation in support of the ITER In-Vessel Viewing System design," *Fusion Engineering and Design*, **89**, *9–10*, 1949–1953 (2014).

[14] A. M. IBRAHIM, D. E. PEPLOW, R. E. GROVE, J. L. PETERSON, and S. R. JOHNSON, "The Multi-Step CADIS Method for Shutdown Dose Rate Calculations and Uncertainty Propagation," *Nuclear Technology*, **192**, *3*, 286–298 (2015).

[15] A. M. IBRAHIM, D. E. PEPLOW, J. L. PETERSON, and R. E. GROVE, "Novel hybrid Monte Carlo/deterministic technique for shutdown dose rate analyses of fusion energy systems," *Fusion Engineering and Design*, **89**, *9–10*, 1933–1938 (2014), Proceedings of the 11th International Symposium on Fusion Nuclear Technology-11 (ISFNT-11) Barcelona, Spain, 15–20 September, 2013.

[16] T. BROWN, J. MENARD, L. E. GUEBLAY, and A. DAVIS, "PPPL ST-FNSF Engineering Design Details," *Fusion Science and Technology*, **68** (2015).

[17] E. LEWIS and W. MILLER JR., *Computational Methods of Neutron Transport*, American Nuclear Society, Inc. (1993).

[18] G. GOERTZEL and M. H. KALOS, "Monte Carlo Methods in Transport Problems," *Progress in Nuclear Energy. Series 1, Physics and Mathematics*, **2**, 315–369 (1958).

[19] M. L. WILLIAMS, "Generalized Contributon Response Theory," *Nuclear Science and Engineering*, , *108*, 355–383 (1991).

[20] T. M. EVANS, A. S. STAFFORD, R. N. SLAYBAUGH, and K. T. CLARNO, "Denovo: A New Three-Dimensional Parallel Discrete Ordinates Code in SCALE," *Nuclear Technology*, **171**, 171–200 (2010).

[21] R. ALCOUFFE, R. BAKER, J. DAHL, S. TURNER, and R. WARD, "PARTISN: A Time-Dependent, Parallel Neutral Particle Transport Code System," Tech. Rep. LA-UR-05-3925 (May 2005).

[22] X-5 MONTE CARLO TEAM, "MCNP - A General Monte Carlo N-Particle Transport Code, Version 5," (2004).

[23] T. J. TAUTGES, P. P. H. WILSON, J. KRAFTCHECK, B. F. SMITH, and D. L. HENDERSON, "Acceleration Techniques for Direct Use of CAD-Based Geometries in Monte Carlo Radiation Transport," in "International Conference on Mathematics, Computational Methods & Reactor Physics (M&C 2009)," American Nuclear Society, Saratoga Springs, NY (2009).

[24] T. J. TAUTGES, R. MEYERS, K. MERKLEY, C. STIMPSON, and C. ERNST, "MOAB: A Mesh-Oriented Database," Tech. Rep. SAND2004-1592, Sandia National Laboratories (2004).

[25] G. D. SJAARDEMA, T. J. TAUTGES, T. J. WILSON, ET AL., *CUBIT mesh generation environment Volume 1: Users manual*, Sandia National Laboratories (1994).

[26] M. E. SAWAN ET AL., "Application of CAD-Neutronics Coupling to Geometrically Complex Fusion Systems," in "Proc. 23rd Symp. Fusion Engineering (SOFE)," San Diego, California (2009).

[27] P. P. H. WILSON, *ALARA: Analytic and Laplacian Adaptive Radioactivity Analysis*, PhD thesis, Fusion Technology Institute, UW-Madison, Madison, WI, United States (Apr. 1999).

[28] P. P. H. WILSON, H. TSIGE-TAMIRAT, H. Y. KHATER, and D. L. HENDERSON, "Validation of the ALARA activation code," *Fusion Technology*, **34**, *3*, 784–788 (1998).

[29] H. BATEMAN, "Solution of a System of Differential Equations Occurring in the Theory of Radio-active Transformations," *Proceeding of the Cambridge Philosophical Society*, **15**, *423* (1910).

[30] "Conversion Coefficients for use in Radiological Protection against External Radiation," *ICRP Publication 74*, **26**, *3/4* (1996).

[31] M. J. LOUGHLIN, "Recommendations on Computation of Dose from Flux Estimates," Tech. Rep. IDM Number ITER_D_29PJCT, ITER (2008).

[32] D. VALENZA, H. IIDA, R. PLENTEDA, and R. T. SANTORO, "Proposal of shutdown dose estimation method by Monte Carlo code," *Fusion Engineering and Design*, **55**, *4*, 411–418 (2001).

[33] R. VILLARI, U. FISCHER, F. MORO, ET AL., "Shutdown dose rate assessment with the Advanced D1S method: Development, applications and validation," *Fusion Engineering and Design*, **89**, *9–10*, 2083–2087 (2014), Proceedings of the 11th International Symposium on Fusion Nuclear Technology-11 (ISFNT-11) Barcelona, Spain, 15–20 September, 2013.

[34] A. DAVIS and A. TURNER, "Comparison of global variance reduction techniques for Monte Carlo radiation transport simulations of ITER," *Fusion Engineering and Design*, **86**, 2698–2700 (2011).

[35] C. BATES, E. BIONDO, K. HUFF, K. KIESLING, and A. SCOPATZ, "PyNE Progress Report," *Transactions of the American Nuclear Society*, **111** (2014).

[36] P. BATISTONI, M. ANGELONE, L. PETRIZZI, ET AL., "Experimental Validation of Shut-Down Dose Rates," Final Report ITER TASK T-426 (2001).

[37] D. MOULE and P. WILSON, "Mesh Generation Methods for Deterministic Radiation Transport Codes," in "Annual Meeting," American Nuclear Society, Hollywood, FL, United States (2011).

[38] J. KOPECKY, "VALIDATION OF FENDL-3/A LIBRARY USING INTEGRAL MEASUREMENTS," Tech. Rep. INDC(NED)-011, IAEA INDC International Nuclear Data Committee, Vienna, Austria (2012).

[39] M. E. SAWAN, "Nuclear Analysis in Support of the Design of ITER Blanket Modules," (June 2011), IEEE Cat. No. CFP11SPF-CDR.

[40] D. L. ALDAMA and A. TRKOV, "FENDL-2.1: Update of an evaluated nuclear data library for fusion applications," Tech. Rep. INDC(NDS)-467 (2004).

[41] E. SARTORI and G. PANINI, "ZZ GROUPSTRUCTURES, VITAMIN-J, XMAS, ECCO-33, ECCO2000 Standard Group Structures," Tech. Rep. 40-03, Nuclear Energy Agency of the OECD (NEA) (1991).

[42] E. POLUNOVSKIY, Private communication (email) (2015), Nuclear analyst, ITER organization.

[43] V. BARABASH, "Chemical compositions of materials representing the components included into basic model for nuclear analysis of ITER," Tech. Rep. IDM UID HTN8X3, ITER (2015).

[44] M. CHADWICK, P. OBLOŽINSKÝ, M. HERMAN, ET AL., "ENDF/B-VII.0: Next Generation Evaluated Nuclear Data Library for Nuclear Science and Technology," *Nuclear Data Sheets*, **107**, *12*, 2931–3060 (2006).

[45] A. DAVIS, "DAGMC plasma sources," `https://github.com/makeclean/DAGMC/tree/plasma_sources/sources` (2016).

[46] C. FAUSSER, A. L. PUMA, F. GABRIEL, and R. VILLARI, "Tokamak D-T neutron source models for different plasma physics confinement modes," *Fusion Engineering and Design*, **87**, *5–6*, 787–792 (2012), Tenth International Symposium on Fusion Nuclear Technology (ISFNT-10).

Appendix A

Bateman Taylor Expansions

In this appendix, it is shown that Equation 3.17, duplicated here:

$$N_i(t) = N_1(0) \sum_{k=1}^{i-1} \left[\frac{P_{k+1} \left(\sum_{z=0}^{Z} \frac{(-t)^z}{z!} (d_k^z - d_i^z) \right)}{d_i - d_k} \prod_{\substack{l=1, \\ l \neq k}}^{i-1} \frac{P_{l+1}}{d_l - d_k} \right], \quad i > 1 \tag{A.1}$$

can be reduced to much simpler expressions by truncating the Taylor expansion. When the Taylor expansion is truncated with $Z = i - 1$, the result is Equation 3.20, duplicated here:

$$N_i(t) = N_1(0) \frac{t^{i-1}}{(i-1)!} \prod_{j=2}^{i} P_j, \quad i > 1. \tag{A.2}$$

When $Z = i$ the result is Equation 3.24, duplicated here:

$$N_i(t) = N_1(0) \frac{t^{i-1}}{i!} \left(i - t \sum_{j=1}^{i} d_i \right) \prod_{k=2}^{i} P_k, \quad i > 1. \tag{A.3}$$

To confirm this, a Mathematica® function was first written in order to evaluate Equation A.1 as a function of i and Z. This function is shown here:

```
BatemanSimp[i_,Z_]:=FullSimplify[Subscript[N,1]*Sum[Subscript[P,k
    ↪ +1]*Sum[(-t)^z/z!*(Subscript[d,k]^z - Subscript[d,i]^z),{z
    ↪ ,0,Z}]/(Subscript[d,i]-Subscript[d,k])*Product[If[l!=k,
    ↪ Subscript[P,l+1]/(Subscript[d,l] - Subscript[d,k]),1],{l,1,i
    ↪ -1}],{k,1,i-1}]]
```

This function was first evaluated for $i = [2, 5]$ with $Z = i - 1$:

```
In[112]:= BatemanSimp[2, 1]
Out[112]= t N1 P2

In[113]:= BatemanSimp[3, 2]
Out[113]= 1/2 t^2 N1 P2 P3

In[114]:= BatemanSimp[4, 3]
Out[114]= 1/6 t^3 N1 P2 P3 P4

In[115]:= BatemanSimp[5, 4]
Out[115]= 1/24 t^4 N1 P2 P3 P4 P5
```

These results are consistent with Equation A.2. The function was then evaluated for $\mathfrak{i} = [2, 5]$ with $Z = \mathfrak{i}$:

```
In[116]:= BatemanSimp[2, 2]
Out[116]= -1/2 t (-2 + t (d1 + d2)) N1 P2

In[117]:= BatemanSimp[3, 3]
Out[117]= -1/6 t^2 (-3 + t (d1 + d2 + d3)) N1 P2 P3

In[118]:= BatemanSimp[4, 4]
Out[118]= -1/24 t^3 (-4 + t (d1 + d2 + d3 + d4)) N1 P2 P3 P4

In[119]:= BatemanSimp[5, 5]
Out[119]= -1/120 t^4 (-5 + t (d1 + d2 + d3 + d4 + d5)) N1 P2 P3 P4 P5
```

These results are consistent with Equation A.3.